Magnetic Adsorbates on Metal Substrates: Magnetic Anisotropy and Switching of the Kondo State

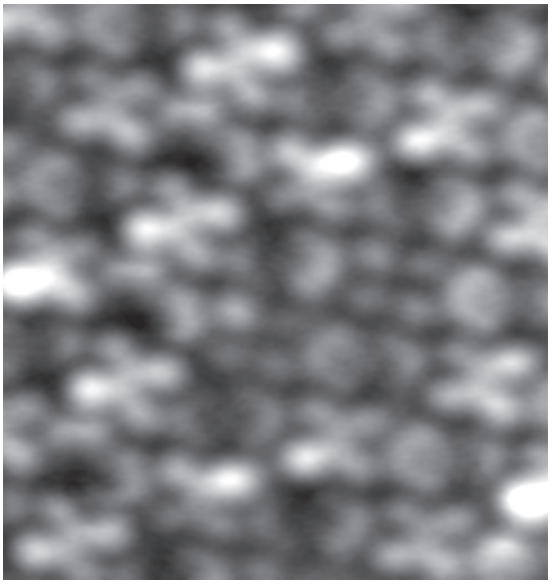

Magnetic Adsorbates on Metal Substrates: Magnetic Anisotropy and Switching of the Kondo State

Dissertation

zur Erlangung des Grades eines
Doktor rer. nat.

am Fachbereich Physik
der Freien Universität Berlin

vorgelegt von
Paul Stoll

Berlin, 2020

Erstgutachterin: Prof. Dr. Katharina J. Franke
Zweitgutachter: Prof. Dr. Wolfgang Kuch

Tag der Disputation: 26.03.2021

Kurzfassung

In der vorliegenden Arbeit werden zwei unterschiedliche Molekülsysteme auf metallischer Oberfläche, die ein Doppelmuldenpotential aufweisen, mit Hilfe von Rastertunnelmikroskopie (STM), Rasterkraftmikroskopie (AFM) und Röntgenabsorption untersucht. Die Motivation für diese Untersuchungen liegt darin, dass Doppelmuldenpotentiale essentiell für die Realisierung von Bits in digitaler Technologie sind. In beiden Molekülsystemen wird außerdem die Frage nach der Ansteuerung durch elektrischen Strom untersucht.

Das erste Molekülsystem ist der Ladungstransferkomplex Tetrathiafulvalen(TTF)/Tetracyanoethylen(TCNE) auf der Gold (111)-Oberfläche. Mittels atomar auflösendem AFM konnten zwei Konformationszustände des TCNE identifiziert werden. Während eine Konformation einen ausgeprägten Kondo-Effekt aufweist, ist dieser in der anderen Konformation nicht vorhanden. Dies wird mit einer Änderung der Parameter des Anderson-Modells durch eine Änderung der Hybridisierung mit der Oberfläche erklärt.

Die Konformationszustände des TCNE im Ladungstransferkomplex liegen auf entgegensetzten Mulden eines asymmetrischen Doppelmuldenpotentials, das mit Hilfe von Schaltratenmessungen per STM untersucht wurde. Beim Schalten in den thermisch stabilen Zustand ist ein wahrscheinlich thermischer Relaxationsschritt vorhanden, der in der anderen Schaltrichtung fehlt. Die unterschiedliche Schaltdynamik ermöglicht ein kontrolliertes Schalten in den gewünschten Zustand.

Das zweite untersuchte Molekülsystem ist der metallorganische Komplex Dysprosium-tris(1,1,1-trifluoro-4-(2-thienyl)-2,4-butanedionat) (Dy(tta)3). Die Monolagen-weise und intakte Adsorption wurde mittels STM überprüft. Durch STM und Röntgenabsorption ist eine Koordinationsgeometrie mit zwei tta-Liganden flach auf der Oberfläche und einem hoch stehenden tta-Liganden evident. Eine uniaxiale magnetische Anisotropie, die gesuchte Energiebarriere, wurde mit Hilfe von Röntgen-Magnetischem Zirkulardichroismus nachgewiesen. Diese Anisotropie wird von den negativen Ladungen der zwei flach liegenden Liganden induziert. Eine Wechselwirkung des magnetischen Moments mit den Tunnelelektronen wird ausgeschlossen.

Abstract

In the following dissertation two different molecular systems on a metallic surface that show a double-well potential are investigated by methods of scanning tunneling microscopy (STM), atomic force microscopy (AFM) and X-ray absorption (XA). The investigation is motivated by the fact that double-well potentials are essential for the realization of digital bits in computational technology. In both molecular systems the question of control or addressing the state by electric current is explored.

The first investigated molecular system is the charge transfer complex tetrathiafulvalene(TTF)/tetracyanoethylene(TCNE) on the (111)-surface of gold. By means of atomically resolved AFM two distinct conformational states of the TCNE were identified. While one state shows a pronounced Kondo effect, the effect is not present in the second state. This is explained by a change of parameters of the Anderson impurity model due to a change of the hybridization with the surface.

The conformational states of the TCNE in the charge transfer complex lie in the two minima of an asymmetric double-well potential that is investigated by measuring of switching rates with STM. When switching into the thermally stable state, a probably thermal relaxation process is present that is absent in the other switching direction. The difference in the switching dynamics allows a controlled switching in the desired state.

The second investigated molecular system is dysprosium-tris(1,1,1-trifluoro-4-(2-thienyl)-2,4-butanedionate) (Dy(tta)3). The intact and monolayer-wise adsorption of the complex on the surface are verified by STM. Combined XA and STM studies prove a coordination geometry with two tta-ligands adsorbed flat on the surface and one tta-ligand standing upright. A uniaxial magnetic anisotropy, the potential barrier, in the central dysprosium ion is detected by X-ray Magnetic Circular Dichroism. The anisotropy is induced by the negative charges of two flat-lying ligands. An interaction of the magnetic moment with tunneling electrons is ruled out.

Contents

1 Introduction and Outline **1**

2 Experimental and theoretical details **5**

2.1 Scanning Tunneling Microscopy 5

2.1.1 The tunneling current 6

2.1.2 Spectroscopy 8

2.1.3 Lock-In detection 10

2.2 Non-contact atomic force microscopy 14

2.2.1 Operational principle: the damped harmonic oscillator 14

2.2.2 Forces at the nano-scale 16

2.2.3 Local Contact Potential Difference 18

2.2.4 The experimental setup 19

2.3 Molecules on metal surfaces 21

2.3.1 Chemisorption 21

2.3.2 Orbital derived states in physisorption 22

2.3.3 The Kondo effect 23

2.4 Magnetism of Lanthanides 26

2.4.1 Paramagnetism of 4f-shell electrons 26

2.4.2 Ligand-field induced anisotropy of single ions 29

2.5 X-ray absorption techniques 32

2.5.1 Angle dependency of the K-edge 35

2.5.2 X-ray Natural Linear Dichroism 36

2.5.3 X-ray Magnetic Circular Dichroism 38

2.6 Literature review on Tetrathiafulvalene and Tetracyanoethylene 41

2.6.1 TTF on Au(111) 41

2.6.2 TCNE on Au(111) 43

2.6.3 TCNE on Cu(111) 44

3 Charge transfer complex TTF/TCNE on the Au(111) surface **47**

3.1 Deposition of the compound onto the surface 48

3.2 Adsorption geometry . . . 48
3.3 Molecular configuration of the high and low states . . . 52
3.3.1 Determination of topography from frequency shift contrast . . . 53
3.3.2 Origin of energy barrier between states . . . 56
3.4 Charge state of conformational states . . . 59
3.4.1 Measurement of electric potential . . . 59
3.4.2 Comparison to simulated potential . . . 62
3.5 Absence of the Kondo effect in the bent conformational state . . . 64
3.6 Summary . . . 65

4 Switching of Tetracyanoethylene in TCNE/TTF on Au(111) 67
4.1 Acquisition of time resolved data . . . 67
4.2 The ladderclimbing model . . . 71
4.3 Order of reaction - estimation of potential barrier height . . . 74
4.3.1 Two phases with similar adsorption . . . 75
4.3.2 Estimation of the energy barrier height in the row phase . . . 77
4.4 Saturation effects of current driven excitation in the checkerboard phase . 82
4.5 Effects of environment on switching . . . 87
4.6 Stability of conformational states and rates at higher temperature. . . . 88
4.7 Controlled switching . . . 90
4.8 Summary . . . 91

5 Magnetic anisotropy in a single-ion lanthanide complex on the surface 93
5.1 Experimental details . . . 96
5.2 Molecular configuration on the Au(111) surface . . . 97
5.3 Magnetic anisotropy of $Dy(tta)_3$ . . . 100
5.3.1 Orientation of $Dy(tta)_3$ 4f orbitals . . . 100
5.3.2 The ground state as confirmation of the uniaxial model . . . 105
5.4 Inelastic tunneling spectra and the first excited state energy . . . 107
5.5 Adsorption structure of $Gd(tta)_3$ on Au(111) . . . 108
5.5.1 XA spectroscopy on $Gd(tta)_3$ on Au(111) . . . 109
5.5.2 Non-magnetic origin of inelastic excitations in $Gd(tta)_3$ . . . 111
5.6 Summary . . . 112

6 Summary 115

1 Introduction and Outline

During the last century physical research played a decisive part in digital technology's advance to smaller length scales. In magnetic hard drives the storage density has been increased by orders of magnitude with the implementation of readout mechanisms using magnetic tunnel resistance [1] and giant magnetoresistance [2, 3]. Half a century before that the invention of the transistor started the development what we now know as the modern digital computing technology [4, 5, 6]

To increase the computational speed and the storage density the devices are made smaller to put more on a smaller surface [7]. As the miniaturization enters atomic scales, material properties change fundamentally. Collective phenomena like magnetic domains or semiconducting band bending loose their meaning when talking about a small number of atoms.

In order to develop digital memory devices with molecular-sized bits, two-state devices composed of single molecules need to be found within basic research. In these molecules the two states need to have different properties, e.g. electric or magnetic, to enable a readout of the state. The potential landscape of the molecular system needs a sufficiently large energy barrier that ensures that the system stays on one side of the potential when not excited by external stimuli. In the case of magnetic memory in magnetic hard drives the barrier of the double well potential is facilitated by magnetic anisotropy.

For single magnetic atoms one might ask, what can create a suitable magnetic anisotropy in a single magnetic metal center, when the magnetic moment is not stabilized by the exchange coupling of other metal atoms. In general, one might look for alternative realizations of two-state devices or energy landscapes with a double-well potential.

The surface science of adsorbed molecules is suited for the research of alternative digital systems. Organic molecules are very versatile and can be synthesized with a wide range of properties. Molecules adsorbed on a metal surface are automatically contacted by an electric lead, which would be important for reading and writing a memory device.

The field of surface science made a breathtaking progress during the last decades. Building on the well established Scanning Tunneling Microscopy technique [8] that revolutionized

the field of surface science, allowing the imaging of surfaces with atomic resolution, the non-contact Atomic Forces Microscopy has been developed [9, 10]. The technique allowed for the first time atomically resolved imaging of single molecules that are adsorbed flat on the surface [11]. Not only did the images look like the familiar Lewis formulas of the molecules, but they opened up new methods of research. The measurement of the Local Contact Potential Difference (LCPD), for instance, allowed the determination of atomic and molecular charges and even partial charges within molecules [12].

In the present work two molecular systems on a metal surface are evaluated as candidates for two-state devices according to two criteria. First, the realization of an energy landscape of two-state devices, a double-well potential. Second, the accessibility by electric tunneling current of the object in the double-well potential, either the center of mass of a molecule or the magnetic moment in a central ion of a metal-organic complex.

The thesis has the following structure. In chapter 2 the basic experimental methods are presented as well as some basic concepts about the investigated physical systems. Scanning Tunneling Microsopy and Atomic Force Microscopy as well as the corresponding spectrosopies are briefly sketched. Here, the interpretation of STM data as a measurement of local density of states is discussed. How to obtain a measure of local electric potential on the sub-molecular level is laid out. Basics concepts and phenomena that occur when molecules are adsorbed on metal surfaces are presented. Briefly, the basic definitions and notations are introduced that are necessary to discuss the magnetism of localized electrons on the atom. Certain X-ray absorption spectroscopy methods are presented. Finally, in section 2.6 a review of the literature on the donor molecule Tetrathiafulvalene (TTF) and the acceptor molecule Tetracyanoethylene (TCNE) adsorbed on different noble metal surface is presented. Some predictions for the charge transfer complex TTF/TCNE on the gold Au(111) surface can be made from the known literature that will be confirmed in this thesis.

Chapter 3 deals with the two-state system TTF/TCNE on the Au(111) surface. Two conformational states that are an implementation of the sought-after two-state device are identified by AFM. The presence of the many-body Kondo state in one of the states and the absence in the other state hints at different charges of the states. This is disproved by LCPD measurements.

Chapter 4 continues the investigation of the molecular system TTF/TCNE but focuses

on the switching dynamics and its relation to the tunneling current. After finding a difference in the switching process for the two directions, a way to controllably switch the TCNE molecule into the desired state is presented.

In chapter 5 the ligand-field-induced uniaxial anisotropy is utilized as a potential barrier for the magnetic moment of a metal center in the metal-organic complex dysprosium-tris(1,1,1-trifluoro-4-(2-thienyl)-2,4-butanedionate) (Dy(tta)3). It is shown that the ligand-field induced anisotropy is uniaxial due to the adsorption on the surface. An addressing of the magnetic moment by the tunneling current will be discussed.

Chapter 6 gives an overview of the results presented in previous chapters.

2 Experimental and theoretical details

The investigation of chemical adsorbates on metal surfaces can be done either by detecting a strong signal from an ensemble of molecules, e.g. using an optical technique, or by observing the individual molecules with a scanning probe setup. This thesis focuses on the latter approach in particular in Chapter 3, while also using the former approach in a combined investigation presented in Chapter 5. In the following chapter the working principles of the used methods, namely the Scanning Tunneling Microscopy (STM) and Spectroscopy as well as the Atomic Force Microscopy (AFM), will be explained in detail. In addition, the near edge X-ray absorption fine structure (NEXAFS) and the X-ray magnetic circular dichroism (XMCD) will be introduced.

2.1 Scanning Tunneling Microscopy

The measurement of conductivity (more precisely the differential conduction) of single atoms and small molecules gives access to a plethora of quantum-mechanical properties such as electronic and vibrational energy levels. To perform the measurement the molecules have to be contacted by electrodes which is achieved in this thesis with STM. A conducting tip is moved over the flat surface of a single crystal with molecules of interest on it and the tunneling current is measured. The surface is scanned line by line keeping either the distance to the surface in the constant height mode of operation or keeping the electric current constant in the constant current mode via an electric feedback. The resulting image of either the current in the constant height mode or the constant current topography is used to identify the individual molecules on the surface and to note their position for further experiments.

2.1.1 The tunneling current

The principal part of a tunneling microscope is the tunneling junction between the probe tip and the metal sample surface. As we will see in the following the size of the electrical tunneling current depends exponentially on the tip-surface distance and on the local density of states on the surface under the tip. This allows precise imaging with sub-molecular resolution.

The tunneling of a particle with mass m and energy E over a barrier of width d in z-direction with energetic height U can be described by the transmission coefficient formula within the quasiclassical approximation (also known as the Wentzel–Kramers–Brillouin or the Liouville–Green method) [13]. Under the assumption that the barrier width d is bigger than the wave length of the particle wave function, the interaction between the two sides of the barrier can be regarded as very low and the states on each side of the barrier are approximated by their eigenstates as if they were isolated. For a free particle tunneling through a one-dimensional barrier the transmission probability takes the well-known exponential form

$$T \propto \exp(-\frac{2}{\hbar}\int_0^d dz\sqrt{2m(U(z)-E)}). \tag{2.1}$$

Using the approximation of a trapezoidal barrier with an average height $\Phi = (U(0) + U(d))/2$ this reduces to

$$T \propto \exp(-\frac{2}{\hbar}d\sqrt{2m(\Phi-E)}). \tag{2.2}$$

In the case of conduction electrons in two metallic leads that are separated by a non-conducting barrier, Φ is the energy difference between the Fermi level and the vacuum level, which is roughly the work function of the two leads. Assuming a typical metal work function value of 4 eV gives an increase of tunneling probability by an order of magnitude for a decrease of the barrier by 1 Å. In the setup of a vacuum barrier between a flat surface and a rough-textured tip the tunneling current is therefore dominated by the tunneling from the tip atoms closest to the surface. Tips with the effective sharpness

of one atom are therefore likely, resulting in lateral resolution of scanning imaging of the length scale of a single atom.

To obtain the electric current between tip and sample with the voltage V applied across the barrier, all matrix elements $M_{\mu\nu}$ for the transition between all tip states ψ_μ and all surface states ψ_ν multiplied by the occupation of the respective state (as described by the Fermi-function) have to be summed up. This results in the current being

$$I = \frac{2\pi e}{\hbar} \sum_{\mu,\nu} f(E_\mu)[1 - f(E_\nu + eV)]|M_{\mu\nu}|^2 \delta(E_\mu - E_\nu). \tag{2.3}$$

As the experiments are mostly done at room temperature or below, the Fermi function can be approximated by a step function. In order to further simplify the equation and to obtain a formula that is easy to discuss, the case of very low voltages can be considered, in which only the states close to the Fermi level contribute to the tunneling conduction. The expression for the current then simplifies to the Ohmic product of the applied voltage, a physical constant and the sum of all transition matrix elements at the Fermi level.

$$I = \frac{2\pi}{\hbar} e^2 V \cdot \sum_{\mu,\nu} |M_{\mu\nu}|^2 \delta(E_\mu - E_F)\delta(E_\nu - E_F). \tag{2.4}$$

It has been shown by Bardeen that the matrix element for transition $M_{\mu\nu}$ can be obtained by integrating the quantum mechanical current over any surface $\vec{S}$ that lies entirely in the tunneling barrier and is perpendicular to the current [14].

$$M_{\mu\nu} = \frac{\hbar}{2m_e} \int d\vec{S}(\psi_\mu^* \vec{\nabla}\psi_\nu - \psi_\nu \vec{\nabla}\psi_\mu^*) \tag{2.5}$$

This has been used by Tersoff and Hamann [15] to develop an expression of the current that separates the states of the tip and the surface. Since the integral in equation 2.5 is performed only over some surface in the barrier region, the assumptions for the particular wave functions need only be accurate at this surface. An exponential decay towards the direction of the gap is plausible for both wave functions. The state wave functions of

the sample surface material ψ_ν can be expanded as general surface Bloch waves that exponentially decay into the gap region and the tip states ψ_μ as asymptotically spherical and also exponentially decaying. Then the current is obtained to be proportional to the following expression.

$$\begin{aligned} I &\propto D_t(E_F)V \cdot \sum_\nu |\psi_\nu(r_0)|^2 \delta(E_\nu - E_F) \\ &\propto D_t(E_F)V\rho_S(r_0). \end{aligned} \tag{2.6}$$

Here, the density of states of the tip at the Fermi level is represented by $D_t(E_F)$, while the density of states of the sample $\rho_S(r_0)$ is evaluated at the center of the tip sphere r_0. With Φ as the work function of the two metals and d the tunneling barrier width, the exponential dependence of the current on d enters via the exponential decay of the sample density of states $\rho_S(r_0) \propto \mathrm{e}^{-2d\frac{\sqrt{2m\Phi}}{\hbar}}$. ρ_S and d are the two quantities of interest that are simultaneously probed by the tip via the tunneling current.

An STM image of an adsorbed molecule on the surface contains contributions from both quantities d and ρ_S. Typically, the frontier orbitals of the molecule hybridize with the Fermi level of the metal surface, effectively extending the surface to the molecule. As a consequence, the current image in a constant height scan of a molecule at low bias voltages for a non-varying $\rho_S(E)$ will resemble the frontier orbital closest to the Fermi level. Typically, the symmetry and the nodal planes of the orbital are clearly distinguishable. The topography signal in a constant current scan (d at constant $I(d)$) is essentially the logarithm of the constant height image.

For the characterization of surfaces and adsorbates the constant current imaging is the most popular scanning regime. Its main drawback is the limited scanning speed due to the bandwidth of the constant current feedback. The practical advantage is that there is no need to determine the plane of the surface, which would require an additional measurement procedure.

2.1.2 Spectroscopy

Beside STM imaging, an extremely valuable tool for studying surfaces and adsorbates originates in the dependence of the tunneling current on the density of states localized

under the tip at a particular point on the surface. It is possible to obtain the information on the energetic position of the adsorbate states with respect to the Fermi-level of the surface by measuring the current and differential conductance while varying the bias voltage. The tunneling probability is proportional to the surface density of states, as seen in equation 2.6. However, the equation was derived under the condition of small voltages and constant ρ_S. It can be extended to higher voltages for a variable ρ_S [16, 17].

$$I \propto \int_{E_F}^{E_F+V} dE\ \rho_S(E)\ D_t(E-eV)\ T(E_F+eV,d), \tag{2.7}$$

$$\text{with} \quad T(E_F+eV,d) = \mathrm{e}^{-2d\frac{\sqrt{m}}{\hbar}\sqrt{2(\Phi+E_F-E)+eV}}, \tag{2.8}$$

where $T(E_F+eV,d)$ is the transmission coefficient that mostly depends on the geometry of the junction. Using the lock-in technique that will be explained in detail in the next section, the differential conductance $\frac{dI}{dV}$ can be conveniently obtained. That in turn, again assuming a constant density of states on the tip, is proportional to the density of states on the surface at the applied voltage, modified by the slowly varying transmission term

$$\frac{dI}{dV}(V,d) \propto\ \rho_S(E_F+eV)T(E_F+eV,d). \tag{2.9}$$

Typically, the density of states observed in spectroscopy originates from surface states of the metal leads or states of the adsorbate such as the highest occupied molecular orbital or the lowest unoccupied molecular orbital. Aside from this elastic tunneling process an inelastic tunneling process can also take place. Such a process is sketched in Figure 2.1 a). An electron from an occupied level in the negatively biased lead can loose the energy $\hbar\omega_0$ to the excitation of a vibration ω_0 while tunneling into the unoccupied level with the energy $\mathrm{E}_2 = \mathrm{E}_1 - \hbar\omega_0$ in the other lead. The possibility of the excitation opens an additional tunneling path increasing the tunneling current. Since the required occupation of levels occurs for bias voltages V that correspond to higher electron energies than the vibration energy, the effect is visible as a kink in the tunneling current diagram that is plotted against the bias voltage at $eV = \hbar\omega_0$, which is shown in 2.1 b). Also shown is the second derivative of the current with respect to the voltage, which has a peak shape with the width that is in most cases dependent mostly on the temperature.

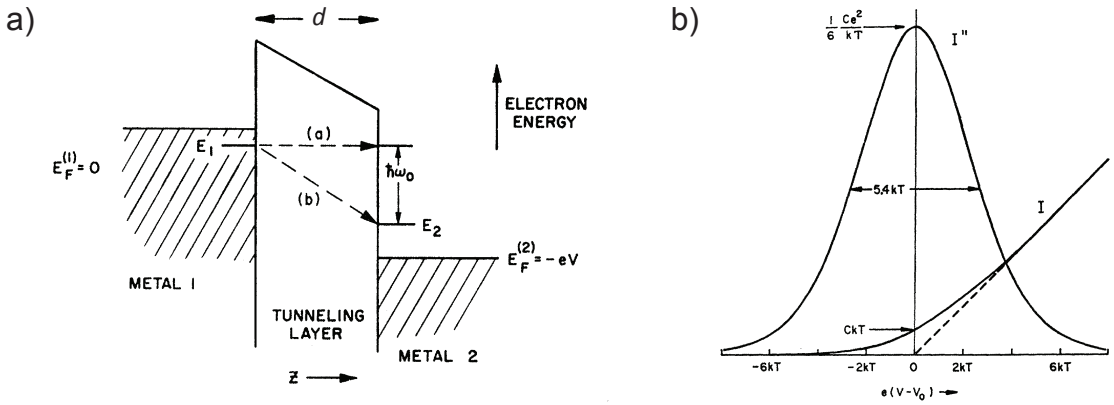

Figure 2.1: Taken from [18]: a) electron tunnels from energy E_1 to $E_1 - \hbar\omega_0 = E_2$ across a barrier with thickness d with potential difference $-eV$; b) resulting kink in the current I and the corresponding peak in its second derivative $I"$

As is the case for imaging, spectroscopy is recorded while maintaining either a constant tip height or a constant current. Constant current spectroscopy has the advantage of compensating the exponentially increasing transmission coefficient of the junction. It is therefore used in the voltage range between some 200 meV and the work-function energy. Constant height spectroscopy, in turn, is useful around the Fermi-energy at voltage magnitudes smaller than 1 V.

2.1.3 Lock-In detection

The exponential dependence of the current on the distance and the billion-fold amplification of the current by the measurement electronics does not only provide detailed images on the atomic scale but also makes the measurement setup highly susceptible to mechanical and electronic noise. While the STM feedback loop keeps the tunneling junction intact thereby making the imaging possible. In the case of open feedback spectroscopy an additional method to compensate noise is used, namely the lock-in technique.

The operational principle of the lock-in detector relies on the orthogonality of trigonometric functions of different periodicity. Multiplying the measured signal by a reference sinus wave and integrating over an integer multiple of the reference sine periods leaves only a part of the signal in a narrow bandwidth around the frequency of the reference wave. All contributions to the signal from frequencies outside the narrowed bandwidth interval

including the noise vanish. Therefore, if the signal of interest has the same periodicity as the reference, it is amplified with respect to its noise level.

Let us consider a resistor that is measured for a time $n \cdot T$ while it is traversed by current I_0 at an applied voltage V_0 to which a modulation voltage $V_M \sin(2\pi f t)$ is added, with $f = \frac{1}{T}$ being the frequency and inverse period of the modulation as well as the reference wave. Along with the signal of interest $I(V)$ also some noise I_{Noise} is measured. Since $I(V)$ is for all practical purposes a real analytic curve, it can be expanded in a Taylor series. The lock-in operation then becomes

$$\begin{aligned}
&\int_0^{n\cdot T} I(V_0 + V_M \cdot \sin(2\pi f t) + I_{\text{Noise}}(t)) \times \frac{1}{\pi}\sin(2\pi f t)\ \mathrm{dt} \\
=&\int_0^{n\cdot T} (I_0 + \frac{\mathrm{d}I}{\mathrm{d}V}|_{V_0} V_M \cdot \sin(2\pi f t) + \frac{1}{2}\frac{\mathrm{d}^2 I}{\mathrm{d}V^2}|_{V_0}(V_M \cdot \sin(2\pi f t))^2 + ...) \times \frac{1}{\pi}\sin(2\pi f t)\ \mathrm{dt} \\
&+ \int_0^{n\cdot T} I_{\text{Noise}}(t)\frac{1}{\pi}\sin(2\pi f t)\ \mathrm{dt} \\
=&\frac{\mathrm{d}I}{\mathrm{d}V}|_{V=V_0} \cdot V_M + \frac{1}{\pi}\tilde{I}_{n\text{Noise}}(f)|_{f=\frac{1}{T}} + O(V_M^3).
\end{aligned} \tag{2.10}$$

As all odd powers of the sine function vanish after integration over one period, all terms with even powers of V_M vanish leaving only odd numbered derivatives. Assuming that the first derivative is bigger than the third and higher derivatives (which they are if V_M is small compared to the energy resolution of the setup) the lock-in signal gives essentially the first derivative with respect to the applied voltage multiplied by the modulation voltage represented by the first term of the last line in the above equation. The in-going noise is transformed to the nth sine Fourier coefficient at the frequency $f = \frac{1}{T}$ and is not multiplied by the modulation voltage. Since the first derivative is the interesting part of the signal, the signal to noise ratio (SNR) of the lock-in signal is the ratio of these first two terms

$$\text{SNR} = \frac{\frac{\mathrm{d}I}{\mathrm{d}V}|_{V=V_0} \cdot V_M}{\frac{1}{\pi}\tilde{I}_{n\text{Noise}}(f)|_{f=\frac{1}{T}}}. \tag{2.11}$$

For modulation widths that are small compared to the energy resolution of the experiment the signal to noise ratio can be increased by increasing V_M, for higher modulations however,

the higher orders of the expansion in equation 2.10 become significant and contribute to the systematic (non-stochastic) part of the measurement error. Therefore V_M is typically set to some low integer fraction of the resolution.

The main reason to use the lock-in detection principle in the first place lies in the denominator of equation 2.11. Noise outside the narrow bandwidth window of $\frac{1}{n \cdot T}$ (here as always $f = \frac{1}{T}$) around the modulation frequency is filtered away by the lock-in technique. Integrating over a higher number of periods n decreases the width of the frequency interval and therefore the measured noise. To increase n while the overall measurement time is kept the same, the modulation frequency can be increased up to the bandwidth limit of the instruments, making a higher bandwidth useful. This contrasts the alternative method of simple averaging for a longer time, where the bandwidth has to be reduced to increase the SNR. The frequency can be chosen to lie far away from frequencies of known external noise sources, such as streetcars.

Electrical conductance measurements in particular have an additional advantage for measuring at a higher modulation frequency. The current over a resistor exhibits a pink noise, a noise that has a lower magnitude at a higher frequency, typically modeled as $\frac{1}{f^\alpha}$ with roughly $0.8 < \alpha < 1.5$. While its physical origins can vary and are not fully understood, pink noise occurs in many different types of conductors [19, 20] including tunneling junctions. As a convenient consequence for lock-in detection a measured bandwidth window at higher frequency contains significantly less noise.

To illustrate the advantage of the lock-in technique over simple averaging of a longer signal trace, the results of a simulation are presented in Figure 2.2. The simulated current in this example is obtained by summing the integral of the two arc tangent steps that are seen as kinks in Figure 2.2 a) and a simulated noise with a $\frac{1}{f^{0.8}}$ power spectral density (Figure 2.2 d)). To obtain the derivative of the current with respect to the bias voltage with a high signal to noise ratio either the lock-in technique can be applied or the current can be averaged for some period of time which would lead to a decrease in noise for longer measurement times. In the first case the lock-in modulation would appear in the current as seen in Figure 2.2 b) while in the second case a step-wise bias voltage ramp might be used and the dI/dV obtained from the mean value of one current step that is shown in Figure 2.2 c). The resulting derivatives strongly differ in noise performance as seen in Figure 2.2 e), with the lock-in signal exhibiting a much cleaner signal. Admittedly, the presented example shows the noise in the case of the arbitrarily chosen modulation

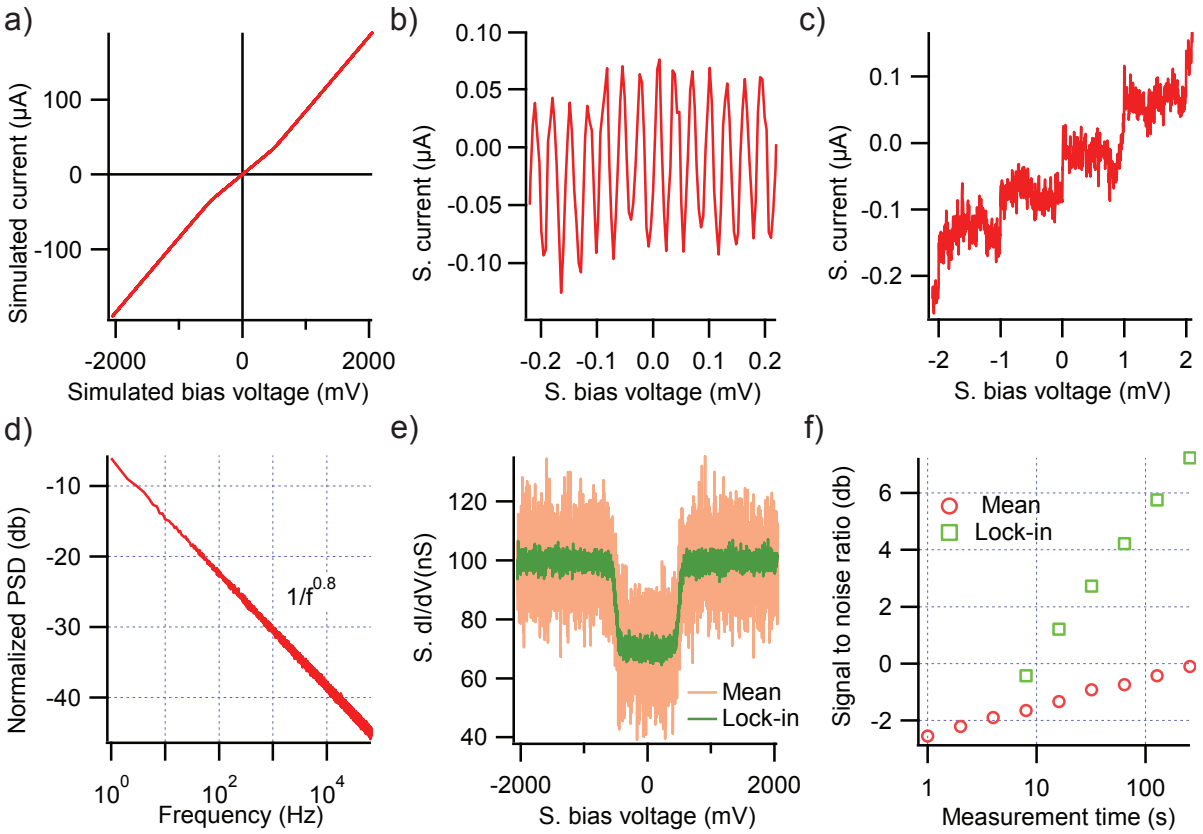

Figure 2.2: a) Simulated current vs. voltage behavior of a hypothetical resistor; dI/dV can be obtained either using lock-in modulation b) or step-wise ramping and differentiating after averaging c); d) power spectral density of a modeled $1/f^{0.8}$ noise added to the simulated current (averaged over 128 trace samples); e) dI/dV obtained from step-wise ramping (pink) and from the lock-in technique (green); f) signal to noise ratio performance vs. invested time for lock-in (green squares) and averaging (red circles) .

amplitude of 1 mV at 1 kHz modulation frequency. Nevertheless, one can obtain the evolution of the signal-to-noise ratios upon increasing the measurement duration. As can be seen in Figure 2.2 f), where the ratio of the feature size of the test signal and the root mean square of the noise are plotted as a function of increased measurement time, the lock-in technique gains a better noise performance much faster than simple averaging. The higher power law dependence is even stronger for higher pink noise power exponents.

2.2 Non-contact atomic force microscopy

For the investigation of charge transfer complexes within this work, the non-contact frequency-shift atomic force microscopy (AFM) is utilized. The operation principle of the imaging technique as well as the measurement of the local potential difference (LCPD) will be explained in detail. These two experimental techniques are used in this work.

The presentation of the AFM technique will follow the review article of Giessibl [21]. The principles of LCPD will be presented following the description in the thesis of Christian Lotze [22].

As described previously the STM signal is dominated by the states at the Fermi level of the substrate and the frontier orbitals of the adsorbates. While insights into the local density of states are of great interest, the interpretation of the conductance signal is often ambiguous. In contrast to this, the AFM signal stems from all attractive and repulsive forces of all electrons between the tip and the surface. Hence, it offers information that is complementary to that of STM.

2.2.1 Operational principle: the damped harmonic oscillator

In non-contact mode AFM the probe tip is placed on an oscillating cantilever. When the probe interacts with the sample of interest the oscillation is perturbed and this change in oscillation is then measurable. The cantilever can be regarded as a very good harmonic oscillator and the force between tip and sample F_{TS} as an addition to the restoring force

$$F = -\left(k + \frac{\partial F_{TS}}{\partial x}\right) x. \tag{2.12}$$

The well-known equation for a driven damped harmonic oscillator describes the movement along the oscillation coordinate x of an oscillator that is driven by the sinusoidal force of amplitude F_D and frequency ω. With the effective mass m, the spring constant k, the resulting eigenfrequency $\omega_0 = 2\pi f_0 = \sqrt{\frac{k}{m}}$ and the quality factor Q the equation is

$$\ddot{x} + \frac{\omega_0}{Q}\dot{x} + \omega_0^2 x = \frac{F_D}{m}\sin\omega t. \tag{2.13}$$

The time dependent solution to the above equation evolves into the steady state solution. Using the ansatz $A\sin(\omega t+\varphi)$ in equation 2.13 one obtains for the amplitude A and phase shift φ between driving force and resulting oscillation

$$A=\frac{\frac{F_D}{m}}{\sqrt{(\frac{\omega_0\omega}{Q})^2+(\omega_0^2-\omega)^2}},\qquad\text{and}\qquad\varphi=\arctan\frac{Q(\omega^2-\omega_0^2)}{\omega_0\omega}-\frac{\pi}{2}. \tag{2.14}$$

In resonance the oscillation amplitude has the maximal value $\frac{F_DQ}{m\omega_0^2}$. In the frequency region $\frac{\omega_0}{Q}$, called the resonance width or full width at half maximum, the amplitude is at least a factor $\frac{1}{\sqrt{2}}$ of that value. In this region the phase can be linearly approximated as roughly $\frac{2Q}{f_0}(f-f_0)$.

The driving force is applied as an electrical signal to the actuator, typically a piezo-crystal near or in the oscillator. The deflection signal, another piezo voltage, is the input of the feedback loop that keeps the oscillator at constant amplitude and at its eigenfrequency. In the amplitude branch of the feedback loop the amplitude of the deflection signal is used to control the amplitude of the driving oscillation. An increase in driving amplitude at resonance frequency would mean a dissipation of the oscillator energy into the sample. In the present thesis the driving amplitude was monitored to stay constant to ensure that no inelastic changes occur in the sample.

In the frequency branch of the feedback circuit a phase locked loop (PLL) adjusts the frequency of the driving oscillator so that the deflection signal oscillation and driving oscillation maintain the exact $\frac{\pi}{2}$ phase difference and thereby the same frequency. The difference in eigenfrequency f_0 between the probe interacting with the sample and when it is sufficiently far away, is called the frequency shift Δf.

With the tip being at some distance to the sample the forces and force gradients are small compared to the restoring force and stiffness of the oscillating cantilever. Taylor-expanding the square root in the expression for the frequency, the frequency shift becomes proportional to the force gradient of the tip sample interaction.

$$\Delta f=\frac{1}{2\pi}\sqrt{\frac{1}{m}\left(k+\frac{\partial F_{TS}}{\partial x}\right)}-\frac{1}{2\pi}\sqrt{\frac{k}{m}}\approx\frac{f_0}{2k}\frac{\partial F_{TS}}{\partial x} \tag{2.15}$$

The obtained frequency shift can be used in mapping with Å resolution by plotting it against the piezo voltage of a scanning microscope in the same manner as imaging with STM. In order to understand what the Δf signal means, we will look at typical forces that occur between the probe and the sample.

2.2.2 Forces at the nano-scale

A sharp probe tip above a surface has two main length scales at which forces act. When the distance of the tip apex to the surface is only few Å the very short ranged Pauli-repulsion and the van der Waals attraction between apex atom and closest surface atom play a major role. For distances in the nanometer range the electrostatic and van der Waals attraction between the several nanometers large portion of the tip and an equally large portion of the surface dominate.

It is common to model the closed ranged interaction with the Lennard-Jones-potential that contains a fast decaying repulsive term and a slower decaying attractive term. The attraction originates from dispersive van der Waals force due to induced dipoles between any two atoms or molecules. Since the dipole potential has a $\frac{1}{z^3}$ distance dependence, the potential for a pair of molecules has a $\frac{1}{z^6}$ shape. For the sake of computational convenience the repulsive term is approximated as the square of the attractive term. The potential takes the form

$$E_{LJ} = \epsilon \left(\left(\frac{z_m}{z} \right)^{12} - 2 \left(\frac{z_m}{z} \right)^{6} \right). \tag{2.16}$$

Here, z_m is the position of the minimum position of the potential and ϵ the binding energy. It is shown in Figure 2.3 in red.

While the repulsive forces only matter at close tip-surface distances, the attractive $\frac{1}{z^6}$ potentials between each tip atom and all surface atoms add up. For a sphere of radius R above an infinite surface at distance z Hamaker calculated [23] the sum of the dispersive potentials to be:

$$E_{vdW} = \frac{HR}{12z} \tag{2.17}$$

Here, H is the material dependent Hamaker constant. An example Hamaker-potential is

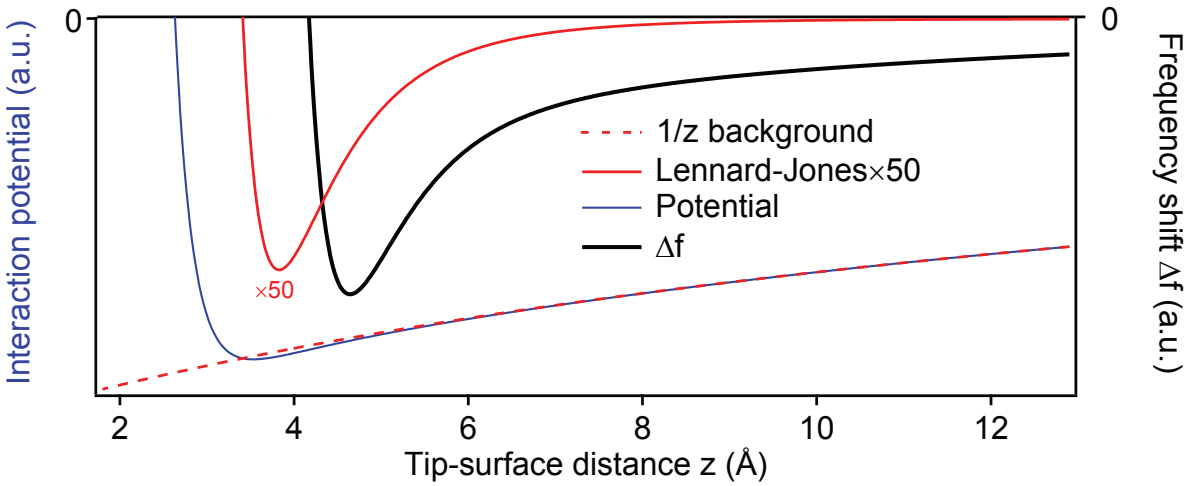

Figure 2.3: Modeled example interaction potential between tip and sample(blue), electrostatic (solid red) and large scale van der Waals 1/z (dashed red) contributions to the potential; resulting frequency shift (black) - second derivative of the potential.

plotted in Figure 2.3 as a red dashed line along with the resulting combined potential which is the sum of the Lennard-Jones- and the Hamaker contribution. Also seen in Figure 2.3 is the second derivative of the potential that is observed as frequency shift Δf in AFM.

Figure 2.3 shows a distance dependence of the frequency shift. It explains the contrast mechanism and resolution in frequency modulated AFM imaging at various distances between the tip and the surface. Within few Å the frequency shift changes its origin and hence the resolution. Above 6 Å tip-surface distance, in this example, only the long range attractive van der Waals force plays a role and only surface steps and larger molecular islands are visible. Between 5 Å and 6 Å the short ranged attractive forces dominate, making larger molecules distinguishable. At slightly above 4 Å the Δf stems from Pauli repulsion. In this regime individual atoms can be imaged.

2.2.3 Local Contact Potential Difference

In addition to the dispersive forces discussed above, electrostatic forces from charges, dipoles and the applied voltage cause an attraction of tip and surface. In the following, a method to detect such charges will be presented.

Being made of conducting materials, the tip and the sample form a capacitor with capacitance C. The energy E_C of this capacitor depends on the voltage V between the tip and sample. The force between the two sides of the capacitor in the direction perpendicular to the plane is the derivative of the energy E_C with respect to the corresponding coordinate.

$$E_C = \frac{1}{2}CV^2; \quad F = \frac{1}{2}\frac{\partial C}{\partial z}V^2. \tag{2.18}$$

Here, the derivative of the voltage is zero since it is held constant by the external power supply in typical experiments.

While a macroscopic capacitor can be free of electric fields and forces at zero bias voltage, this is not the case on the nanometer scale. Local charges and dipoles create electric fields that offset the voltage at which the electrostatic force in the capacitor is minimal. The AFM frequency shift, which is proportional to the second derivative of the energy, shows a parabola that is displaced by the so-called local contact potential difference (LCPD).

$$\Delta f \propto \frac{\partial^2 C}{\partial z^2}(V - \mathrm{LCPD})^2 \tag{2.19}$$

A positive charge on the sample surface has to be compensated with a negative bias voltage applied to the sample side. LCPD measurements can be used to determine the charge of single atoms on the surface [11] and intramolecular charge distributions of small molecules [12]. They are used in this thesis to determine the charge state of switching molecules.

The term contact potential difference originates from the Kelvin probe technique [24]. The difference in work functions in two metals that are electrically connected, i.e. their Fermi levels are aligned, leads to a charge at the interface. In a capacitor of known

capacitance C and the contact potential difference CPD, this charge is $Q = C \times \mathrm{CPD}$. When the capacitance is varied in a known way, like the change in distance of a plate capacitor, the CPD can be obtained by measuring the voltage and thereby the charge at the capacitor plate.

Even if the tip and surface are made from the same material and no charges or dipoles are located at the surface, there typically is a CPD. The main source is the Smoluchowski-dipole [25] of the sharp tip. Due to the kinetic term in the Hamiltonian, the electron density on a surface tends to be smoother than the corrugation presented by the positions of atomic core. As the tip is a highly corrugated surface, this results in a dipole pointing with its positive charge towards the sample surface. Such a dipole shifts the parabola in equation 2.19 towards positive bias voltage values. As a practical consequence, experimental values of the LCPD yield relative rather than absolute information on the variation in electric potential across different positions of the tip above the surface.

2.2.4 The experimental setup

The STM and AFM data that will be presented in the later chapters was acquired in two Createc-type STM-AFM setups. The basic design ideas of the setup will be layed out.

Surface science methods like STM rely on ultra high vacuum (UHV) conditions to ensure that the investigated surface and investigated adsorbate are preserved during examination. Therefore, the STM setup is incorporated into a UHV-chamber. After the sample is prepared in one part of the chamber it is transferred without leaving the vacuum into the STM.

Various pumps like the turbomolecular pump, the ion pump and the titan sublimation pump maintain a pressure of few 10^{-10} mbar during the preparation of the sample. In low temperature STM the cryostat temperature of $\sim$4.8 K creates the effect of a cryo-pump that reduces the pressure further below 10^{-11} mbar ensuring cleanness for several weeks of measurement time. The initial cleanness is visible in the STM itself.

Since most volatile impurities have higher condensation temperatures than the temperature of liquid helium, they are pumped efficiently by the cryostat. An exception is the hydrogen molecule (H_2) that is not visible in STM in coverages below a mono-layer and diffuses from outside through the valves into the setup. The presence of H_2 can be

detected in I-V curves at currents of several nA [26]. When a contamination is detected, the sample is re-prepared.

In studies of adsorbates on surfaces the sample is typically prepared by cleaning the metal surface and depositing the adsorbate on it. The cleaning is achieved by repeated cycles of bombardment with noble gas atoms at kinetic energies in the order of magnitude of 1 keV and subsequent annealing to temperatures that thermally restructure the surface. The deposition of the studied adsorbate is mostly done by heating bulk specimen of the adsorbate to the evaporation temperature while positioning the sample surface in front of the evaporation process.

The STM in the Besocke design [27], as is used in Createc machines, consists of three piezo crystals holding a disc shaped "ramp" which has a fourth piezo crystal in the center. On the central piezo the STM tip or the AFM sensor is mounted. The AFM sensor consists of another piezo crystal and a tuning-fork shaped cantilever on which the STM tip is mounted.

The four STM piezo crystals have the shape of a tube. They are electrically contacted in such a way that the length of the tube as well as the bending change applying a piezo voltage. On each of the three outer piezo crystals lies one of the three segments of the "ramp" disc. Each segment is slightly sloped forming a ramp that translates the rotation of the disc into vertical displacement of the tip. In this manner movements of the tip on the scale of a millimeter are facilitated, which are necessary during the transfer of the sample in and out the STM.

A substantial part of the measurement time is dedicated to the forming of the tip. For this purpose the tip is repeatedly inserted into the sample surface with varying bias voltages applied. After each treatment the tip is tested for scanning resolution and spectroscopic adequacy. For AFM experiments the treatment and testing are more extensive since tips with a low background frequency shift are needed.

The acquired spectra were analyzed using the Igor Pro software [28] while the images were acquired using the STMAFM 3.1 software provided by Createc and analyzed using WSxM 5.0 [29].

2.3 Molecules on metal surfaces

Some basic knowledge about phenomena that occur in molecules adsorbed on metal surfaces like chemisorption and physisorption as well as the Kondo effect that will serve as a gauge for the charge of the adsorbed molecule in Chapter 3 will be presented in the following. The lowering of the LUMO energy that will be observed and exploited for the determination of the adsorption geometry in Chapter 5 will be sketched.

2.3.1 Chemisorption

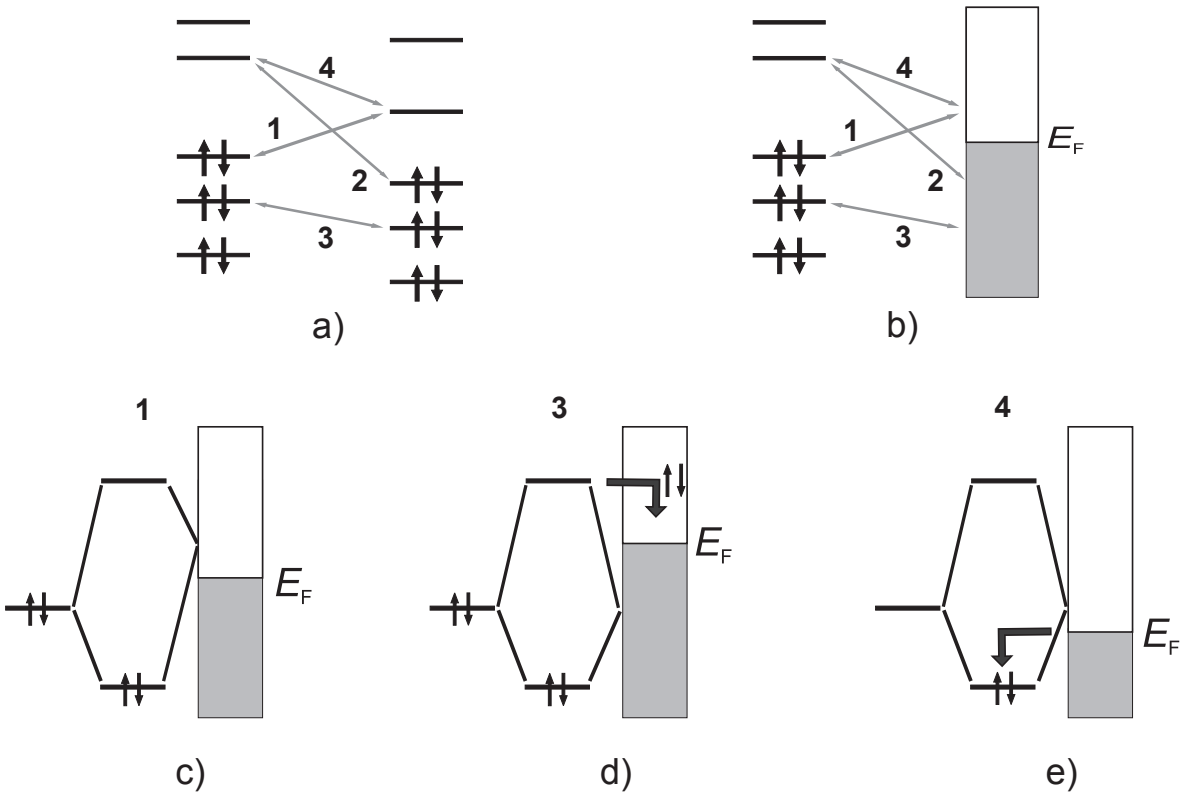

Figure 2.4: Schematic diagrams of (a) molecule–molecule orbital interactions and (b) molecule–metallic surface interactions. Cases (c), (d) and (e) represent the 1, 3 and 4 molecule–metallic surface interactions, respectively. Image taken from [30, 31].

Although chemisorption is rare on noble metal surfaces like gold and no chemisorbed molecules are studied in this work, it poses a clear picture of the evolution of the molecular orbitals of the adsorbates and their interaction with the states of the metallic surface.

The discussion of chemisorption follows the review of Hoffmann [30]. To introduce the basic concept of orbital hybridization we look at the well-known case of molecule-molecule bonding shown in Figure 2.4 a). Filled and unoccupied orbitals of one molecule can mix with filled and unoccupied orbitals of a second molecule. Hybridization creates an energetically lowered bonding and a higher anti-bonding orbital. If instead of the second molecule a solid is considered, essentially the same interactions take place with solid levels below and above the Fermi-level as sketched in 2.4 b). According to perturbation theory states lying closer on energy hybridize more.

In the case of a hybridization of an occupied state and an unoccupied state, like those marked as 1 and 2 in Figure 2.4, the bonding orbital is filled while the anti-bonding state is empty. This well-known mechanism of a chemical bond is sketched in Figure 2.4 c). Interaction of the type 3, shown in Figure 2.4 d), between occupied levels result in repulsion and are the source of steric effects.

Typically, the hybridization of unoccupied levels does not affect the bonding between molecules at all. On surfaces, however, it is possible that the bonding overlap of an unoccupied surface state and and unoccupied molecular orbital lies below the Fermi level of the solid. As illustrated in Figure 2.4 e) a bond can then be formed.

The bonding to a metal can deform organic molecules. A very simple example is Zeise's salt, where the ethylene molecule bends away its hydrogen groups from the platinum ion [32]. The ethylene donates electron density to the metal in a sigma-like overlap of atomic and the molecular π orbitals. Simultaneously, electron density is donated back by a pi-like overlap of the d-orbital and the π^* orbital. This interaction of the π system with the d-orbital results in a rehybridization from the flat sp^2 to the bent sp^3 configuration.

A chemical bond does not necessarily form between the adsorbate and the surface. If both the HOMO and the LUMO are energetically too far away from the Fermi-level upon adsorption or if there is insufficient spatial overlap of relevant states, the conditions for the formation of a bond that are depicted in Figure 2.4 are not met.

2.3.2 Orbital derived states in physisorption

As described previously in 2.2, the van der Waals forces between the molecule and a metal surface form an attractive potential for the molecule. Such cases in which van

der Waals forces are the dominating force of bonding between molecule and surface are termed physisorption. They show a characteristic bonding length of at least 2 Å and lead to quantitative rather than qualitative changes in the electronic structure of the constituents.

Between the two extreme cases of chemisorption and pure physisorption there exists a wide variety of cases with both contributions. Among the adsorbates that do not form full chemical bonds with the surface only the most inert lack significant hybridization between adsorbate and surface states. The sharp levels of an isolated molecule become broadened states of an adsorbate. The width of the resonance reflects the lifetime of an ionic excitation i.e. the time an electron (hole) can reside on the LUMO (HOMO) before it is conducted to the metal. The lifetimes of excited states in adsorbates on metals lie in the femtosecond range (e.g. [33]) as opposed to the isolated molecules where the lifetimes lie in the range of tens of nanoseconds [34].

Even when states of a metal surface do not mix with molecular states and the metal does not fill or empty the molecular orbitals, the proximity of the conducting surface alters the position of the molecular orbitals. A significant component of the energetic distance of the HOMO and the LUMO and hence, their distance to the Fermi-level, is the so-called on-site Coulomb repulsion U. Adding or removing an electron to the neutral molecule costs the energy that is needed to create the electric field of the charge. However, the image charge of the metal screens this electric field, leading to a reduction of the HOMO-LUMO gap. Both levels lie closer to the Fermi-level [35, 36].

The amount of screening and therefore the energy by which the levels are shifted depends strongly on the distance to the surface. As a consequence, molecular orbitals that are degenerate due to symmetry in the gas phase are split on the surface if they are situated on different sides of the molecule. A well-known example is the case of C_{60} on Au(111) where the triply degenerated LUMO splits upon adsorption [37].

2.3.3 The Kondo effect

While chemisorption and physisorption happen at energy scales of some eV down to some 100 meV, phenomena at few meV also play an important role in surface science. Magnetic adsorbates on surfaces show an interesting quantum phenomenon at low temperatures

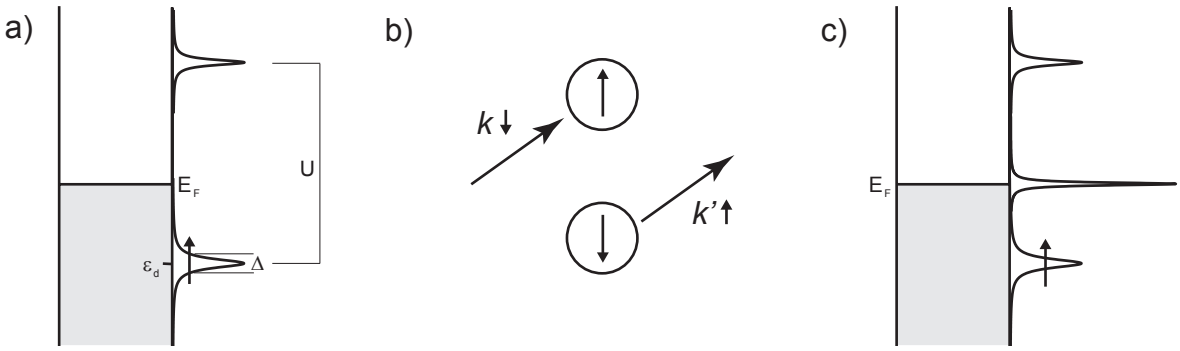

Figure 2.5: a) Anderson impurity model with the impurity energy ϵ_d Coulomb repulsion energy U and hybridization strength Δ; b) spin-flip scattering processes: conduction electron with momentum k and spin $\downarrow$ is scattered at the impurity with spin $\uparrow$ leaving the conduction electron with the momentum k' and simultaneously flipping both spins; sketch adapted from [39, 38]; c) Kondo effect leads to a density of states at E_F.

known as the Kondo effect. The basic terms and concepts relevant to the Kondo effect will be outlined following the descriptions in [38] and [39].

The first experimental evidence for a low energy scale quantum phenomenon stem from resistance measurements in the bulk of several metals in particular gold wires [40, 41]. Contrary to the expectation of a steadily decreasing resistance upon lowering the temperature, a resistance minimum appeared at a finite temperature. Along with the low temperature, diluted localized magnetic moments in the material seemed to be the key ingredient [42]. Motivated by this phenomenology J. Kondo developed the model that includes an additional scattering effect between the impurity and the conduction electrons, the Kondo effect. Originally, the model predicted an unphysical infinite increase of resistance for temperatures approaching 0 K, while being accurate above a certain characteristic temperature T_K [39]. Upon the development of Anderson's scaling theory [43] and the application of renormalization group methods[44] the behavior below T_K could be described correctly.

It has been further shown by [45] that the Kondo Hamiltonian describes a strong coupling regime of the Anderson impurity model [46], which will be described here. The main features of the model are on the one hand a localized level occupied by a single electron with spin $\frac{1}{2}$, historically an impurity d-shell level, and on the other hand a continuum of conduction electrons. The electronic level lies at an energy ϵ_d below the Fermi energy of the conductor and is therefore occupied. To occupy the level with an additional electron,

a Coulomb repulsion energy U has to be overcome and $\epsilon_d + U$ lies above the Fermi energy. Both energies, ϵ_d and $\epsilon_d + U$, have to lie considerably further than the impurity-level width Δ from the Fermi-energy. The model is described by the following Hamiltonian:

$$H = \epsilon_d(n_{d,\uparrow} + n_{d,\downarrow}) + U n_{d,\uparrow} n_{d,\downarrow} + \sum_{k,s} \epsilon_k n_{k,s} + \sum_{k,s} (V_k c^\dagger_{k,s} c_{d,s} + V_k^* c^\dagger_{d,s} c_{k,s}). \tag{2.20}$$

Here, ϵ_k is the energy of the conduction-electron state of momentum k, $n_{k,s}$ is the number operator for conduction electrons of momentum k and spin s, the latter having the two values $\downarrow$ and $\uparrow$. Analogously, $n_{d,s}$ is the number operator for the impurity state. Both number operators are compositions of creation and annihilation operators $c^\dagger_{d,s}\ c_{d,s}$ on the impurity and $c^\dagger_{k,s}\ c_{k,s}$ in the conduction band. The last summation term is the one responsible for the formation of the new state. The term describes the mixing of the conduction and impurity states and contains the coupling coefficient V_k that add up to the width of the impurity level $\Delta = \Sigma_k |V_k|^2 \delta(-\epsilon_k)$ [47]. The model is illustrated in Figure 2.5 a).

The spin of the impurity electron is degenerate and can interact with the conduction electrons. In Figure 2.5 b) an exchange process is sketched. The conduction electron with momentum k and spin $\downarrow$ is scattered at the impurity with spin $\uparrow$ leaving the conduction electron with the momentum k' and simultaneously flipping both spins [38]. Simultaneously, a spin excitation is created near the Fermi level that screens the impurity spin [39]. This leads to the rise of the resonance near the Fermi level that is seen in Figure 2.5 c) and is detectable by STM.

As mentioned above, the characteristic energy scale of the effect is the Kondo temperature T_K. Expressed with parameters of the Anderson impurity model it looks as follows [47, 39, 38]:

$$k_B T_K =\simeq \sqrt{\frac{2}{\pi}\Delta U}\ \exp\left(-\frac{\pi}{2\Delta}\left(\left|\frac{1}{\epsilon_d}\right| + \left|\frac{1}{\epsilon_d + U}\right|\right)^{-1}\right) \tag{2.21}$$

The form of the ratio in brackets is written in a way that makes it easier to discuss the change in Kondo temperature with the parameters of the impurity. This can be used to explain the presence and absence of the Kondo resonance upon a change in the parameters of the impurity.

2.4 Magnetism of Lanthanides

The magnetism of Dysprosium being a major object of interest in this work, some general remarks about lanthanide metals shall be made. The lanthanide row of the periodic table consists of elements with a partially filled 4f-shell. The partial filling of this shell is responsible for the magnetic and phosphorescent properties that make these materials widely used in technological applications.

2.4.1 Paramagnetism of 4f-shell electrons

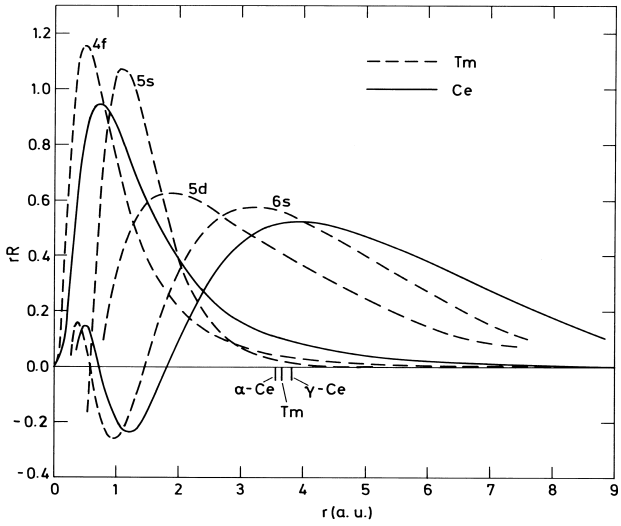

Figure 2.6: From [48]: Radial components of the 4f-wave functions of Ce(1 4f-electron) and Tm (13 4f-electrons)

According to the Aufbau principle, with rising element number the atomic shells are filled in the order of rising $n+l$, with n and l being the principle and azimuthal quantum number of the hydrogen-like atom respectively. The most peculiar thing about the 4f-shell is seen in Figure 2.6. The radial components of the wavefunctions of the example lanthonides Thulium and Cerium are plotted against the distance r to the atomic core. Strikingly, the 4f-shell, which is filled after the 5s, 5p and the 6s shells, shows most of its electron density significantly closer to the atom center than the 5s, 5d and, most prominently, the 6s shell. As a consequence, the 4f wave function does not significantly overlap with the wavefunctions of the neighboring atoms and therefore does not take part in the chemical bond.

The 4f-shell is an inner shell and as such insulated from the environment of the atom. At the same time it is only partially filled, which results in a magnetic moment from the spin and the orbital moment of the electrons. Unlike in the 3d-transition metals, the orbital moment of the electrons is never quenched and contributes to the magnetic moment [49].

In contrast to the d-shells, the ligand- or crystal-field in the 4f-shell is always weaker than the spin-orbit energy and the electron repulsion energy due to its isolated character. This ordering of energetic scales of magnitude makes the 4f-shell best described in the Russel-Saunders coupling scheme [50, 48]. The orbital quantum number L and the spin quantum number S of the whole shell are good quantum numbers. Their values in the ground state are given by the Hund's rules. Both vectors $\vec{L}$ and $\vec{S}$ add up to the total orbital momentum $\vec{J}$ with the quantum number J, whose value again is given by a Hund's rule. Each level represented by the term symbol ${}^{2S+1}L_J$ can split into up to $2J+1$ states.

The g_J-factor that is needed to connect the total orbital momentum quantum number with the corresponding magnetic moment, is given by the Landé formula [49, 51, 13]. With the quantum number M as the projection of the total orbital momentum on the z-axis and eigenvalue of J_z, the magnetization M_z of the atom is

$$\mathrm{M}_z = \mu_B g_j M. \tag{2.22}$$

From this follows that the highest possible component of the magnetic moment in the direction of the magnetic field is $g_j J$. It can be obtained experimentally by measurements of saturation magnetization at temperatures approaching $T = 0\,\mathrm{K}$ [52].

At higher temperatures T the magnetization in a magnetic field is given by the thermodynamic expectation value $\langle \mathrm{M}_z \rangle$:

$$\frac{\langle \mathrm{M}_z \rangle}{\mu_B g_j} = \langle M \rangle = \frac{\sum_M M \exp\left(\varepsilon(M)/k_B T\right)}{\sum_M \exp\left(\varepsilon(M)/k_B T\right)}. \tag{2.23}$$

Here, $\varepsilon(M)$ is the energy that contains the Zeeman energy $\varepsilon_Z = \mu_B g_j M B$, but can also contain other contributions like the electrostatic interaction with the crystal or ligand field.

The magnetic susceptibility χ, which is the initial slope of the magnetization curve, of

	$4f^N$	$^{2S+1}L_J$	g_j	$g_j J$	$g_j[J(J+1)]^{\frac{1}{2}}$	M_{eff}^{exp}
Ce^{3+}	$4f^1$	$^2F_{5/2}$	6/7	15/7	2.535	2.3-2.5
Pr^{3+}	$4f^2$	$^3H_4$	4/5	16/5	3.578	3.4-3.6
Nd^{3+}	$4f^3$	$^4I_{9/2}$	8/11	36/11	3.618	3.4-3.5
Pm^{3+}	$4f^4$	$^5I_4$	3/5	12/5	2.683	2.9
Sm^{3+}	$4f^5$	$^6H_{5/2}$	2/7	5/7	0.845	1.6
Eu^{3+}	$4f^6$	$^7F_0$	0	0	0	3.5
Gd^{3+}	$4f^7$	$^8S_{7/2}$	2	7	7.937	7.8-7.9
Tb^{3+}	$4f^8$	$^7F_6$	3/2	9	9.721	9.7-9.8
Dy^{3+}	$4f^9$	$^6H_{15/2}$	4/3	10	10.646	10.2-10.6
Ho^{3+}	$4f^{10}$	$^5I_8$	5/4	10	10.607	10.3-10.5
Er^{3+}	$4f^{11}$	$^4I_{15/2}$	6/5	9	9.581	9.4-9.5
Tm^{3+}	$4f^{12}$	$^3H_6$	7/6	7	7.561	7.5
Yb^{3+}	$4f^{13}$	$^2F_{7/2}$	8/7	4	4.536	4.5

Table 2.1: Characteristics of trivalent lanthanide ions according to [52, 53]: configuration, term-symbol of the Hund's rules ground state, corresponding g-factor, saturation magnetic moment $g_J J$ in units of μ_B, the effective magnetic moment from the Curie law [52] (in μ_B) and the effective magnetic moment (in μ_B) from measurements of the Curie constant (in μ_B) [53].

single paramagnetic ions follows Curie's law [49]:

$$\chi = \frac{\mu_0 g_J^2 \mu_B^2 J(J+1)}{3k_B T}. \tag{2.24}$$

It is then possible to obtain experimentally the effective magnetic moments $g_J[J(J+1)]^{\frac{1}{2}}$ from measurements of the susceptibility at different temperatures. The results of such measurements for the typically trivalent ions were compiled by van Vleck [53] and can be seen in table 2.1.

As a result of the isolated nature of the 4f-shell the experimentally observed effective magnetic moments agree with the Hund's rules values of the orbital moments. In table 2.1 the characteristics of the trivalent lanthanide ions for the non trivial configurations of the 4f-shell are presented. Except for samarium and europium, which show van-Vleck susceptibility [53], the Curie's law effective magnetic moments $g_J^2 J(J+1)$ match the measured values that were obtained for different salts of the lanthanides [53, 52]. This agreement validates the picture of the 4f-shell being in the Hund's rules ground state with J and M being good quantum numbers. The constant J of the ground state term

and the J, M basis are important ingredients in the formalism of the magnetic anisotropy of 4f electrons.

2.4.2 Ligand-field induced anisotropy of single ions

When incorporated in molecules or crystals, ions of lanthanides are affected by the electrostatic interaction with the chemical ligands or the neighboring atoms. The degeneracy of the $2J + 1$ states of the ground state level with term symbol ${}^{2S+1}L_J$ is lifted. As a result of this interaction the orbital moment L of the partially filled f-shell acquires one or more preferred directions. Due to the strong spin-orbit coupling the spin S of the shell aligns parallel or anti-parallel (depending on the configuration) with the orbital moment. One can describe the pronounced anisotropy of the total angular momentum J in terms of J, M and material dependent constants [48, 49, 50], as shall be done in the following.

The interaction energy ε_a of the 4f-shell with the ligand field is given by the integral over the charge density $\rho_{4f}(\mathbf{r})$ and the electrostatic potential φ_{lf} of the ligand. The potential in turn is given by the charge density $\rho(\mathbf{r})$ and the Coulomb law integral.

$$\varepsilon_a = \int e\rho_{4f}(\vec{r})\varphi_{cf}(\vec{r})d^3r \ , \quad \text{with} \quad \varphi_{lf}(\vec{r}) = -\int \frac{e\rho(\vec{r'})}{4\pi\epsilon_0|\vec{r} - \vec{r'}|}d^3r'. \tag{2.25}$$

Here, ϵ_0 is the vacuum permittivity and $-e$ is the electron charge. The potential can be expanded in terms of spherical harmonics.

$$\varphi_{lf}(\vec{r}) = \sum_{lm} A_l^m Y_{lm}(\hat{\vec{r}}) \ , \quad \text{with} \quad A_l^m = -(-1)^m \frac{4\pi}{2l+1} \int \frac{e\rho(\vec{r'})}{4\pi\epsilon_0 r'^{l+1}} Y_{l-m}(\hat{\vec{r'}})dr'^3 \ . \tag{2.26}$$

Here, the well-known spherical harmonics $Y_{lm}(\hat{\mathbf{r}})$ are evaluated on the vector $\hat{\mathbf{r}}$ that has unit length and points in the direction of the position vector $\mathbf{r}$. The summation over m goes from $-l$ to l. Computing the matrix elements of the interaction Hamiltonian involves integrating over eigenstates of the Laplace operator that are spherical harmonics themselves. Due to the properties of spherical harmonics, in the case of the interaction with f-electrons, the summation over l in Equation 2.26 only needs to go from 0 to 6. After further considerations of general properties of spherical harmonics and matrix

elements within the groundstate configuration only terms with even l are non-zero [50]. Although the first term in the summation has the largest contribution numerically, it contains harmonics with $l = 0$ and does not lead to a splitting of states. It will therefore be omitted in the following.

It is possible to further simplify the evaluation of matrix elements of $\varphi_{lf}(\mathbf{r})$ in Equation 2.26 by applying the Wigner-Eckart theorem [48, 54]. For a constant J, the matrix elements of $\varphi_{lf}(\mathbf{r})$ are proportional to operator equivalents that are written in terms of $\vec{J}$ operators.

$$H_{lf} = \sum_{l=2,4,6} \sum_{m=-l,\ldots,l} B_l^m \mathbf{O}_l^m(\vec{J}). \tag{2.27}$$

The terms with $l = 2$ contain the following second powers of components of $\vec{J}$:

$$\mathbf{O}_2^0 = 3J_z^2 - J(J+1)\ , \quad \text{and} \quad \mathbf{O}_2^2 = \frac{1}{2}(J_+^2 + J_-^2) = J_x^2 - J_y^2. \tag{2.28}$$

The corresponding coefficients B_2^0 and B_2^2 are widely known in literature as zero splitting parameters $D = 3B_2^0$ called axial anisotropy and $E = B_2^2$ the transverse anisotropy. The operators $\mathbf{O}_m^2$ for the remaining values of m would also be relevant for an arbitrary direction of the x, y and z-axis. However, if the axes are chosen such that first the absolute value of B_2^0 and then that of B_2^2 is maximized, the terms with $m = \pm 1, -2$ vanish.

In absence of a magnetic field a non-zero D will lift the degeneracy of states with different M. For negative values of D, the z-axis is the easy axis of anisotropy. The magnetic moment generated by the 4f-shell will tend to point along this axis.

Which terms of H_{lf} in Equation 2.27 are non-zero depends on the symmetry of the ligand or crystal field. In a cubic crystal field, for example, only the operators $\mathbf{O}_0^4$, $\mathbf{O}_4^4$, $\mathbf{O}_0^6$ and $\mathbf{O}_4^6$ contribute, while only the coefficients B_4^4 and B_6^4 are linearly independent. In lower symmetry such as in organic molecules, on the other hand, moments with $l = 4$ and higher are significantly lower and can be neglected. This is due to a faster fall-off as seen in the higher power in the denominator in the expansion 2.26 and higher length of coordination bonds compared to metallic bonds.

To develop an intuition, which ligand field for which M leads to a lower energy, a more

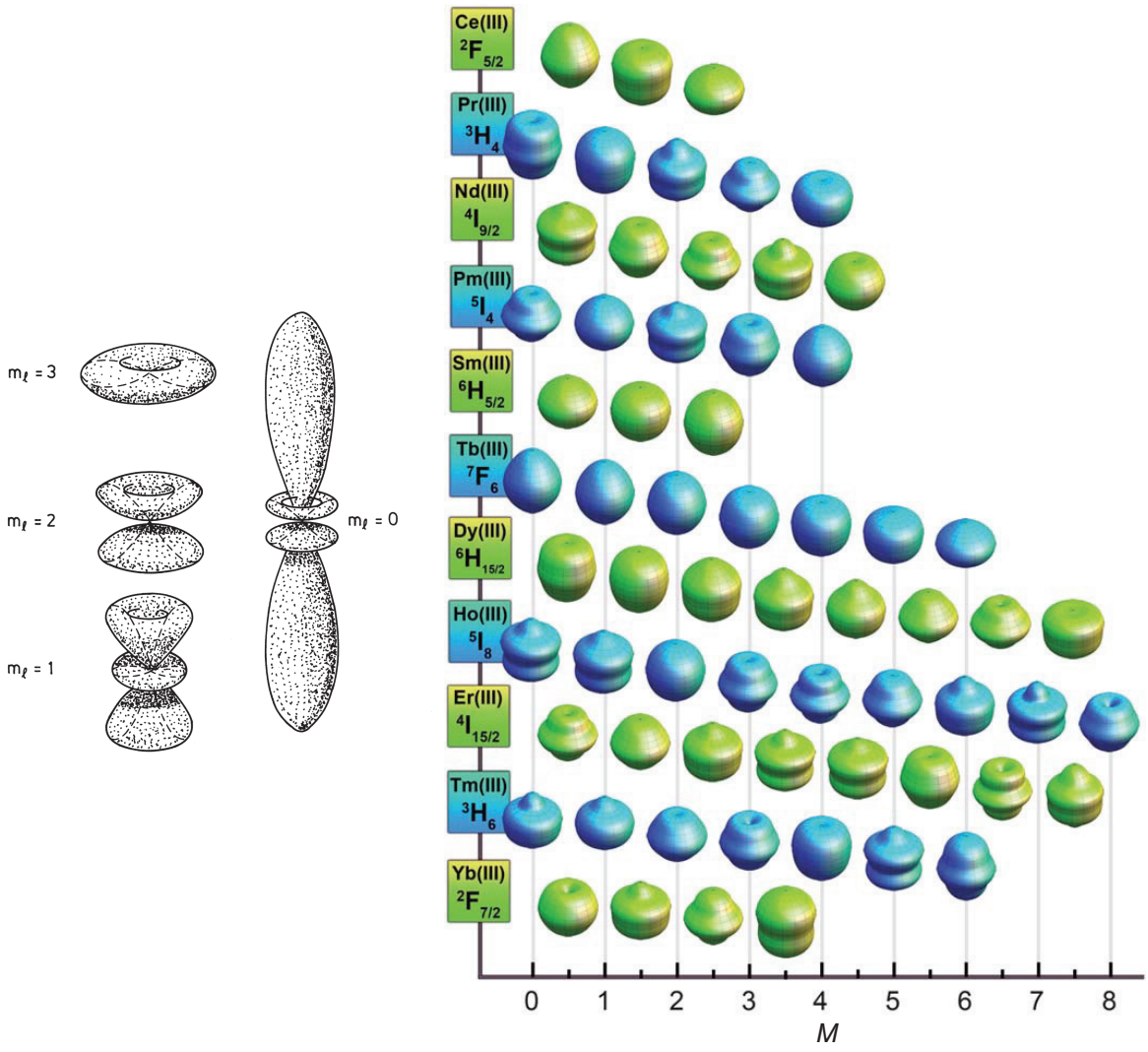

Figure 2.7: Left: angular variations of 4f wave function for various m_l [48]; right: angular dependence of the total 4f-charge density for M states composing the lowest spin-orbit coupled (J) state for each lanthanide [55, 56].

graphic approach has been taken by Rinehart and Long [55]. Instead of looking at the electric potential of the ligand, one can consider the shape of the charge density of the 4f-shell itself and how it will react to a particular ligand field. Figure 2.7 shows the shape of single electron f-orbitals for various values of the angular momentum quantum number m_l. For high values of m_l the 4f density is oblate shaped, while the $m_l = 0$ state is more cigar shaped.

When we consider the many electron total charge density for different lanthanides, which

is plotted in Figure 2.7 for various values of M, a similar pattern occurs for some of the elements. Elements with single- or few-electron configurations like cerium (Ce), praseodymium (Pr), terbium (Tb) and dysprosium (Dy) show also oblate shaped charge density distributions for high M, while being more cigar-shaped for low M.

The interaction energy of this charge density increases with smaller distance to negatively charged ligands, as seen in the equations 2.25. For the oblate shaped density distribution, coordination of ligands to the equatorial region are higher in energy, while ligands pointing towards the poles are lower [57]. Consequently, if there are three or more closest negatively charged ligand atoms lying in a plane with the Ce, Pr, Tb or Dy ion in the center, states with a cigar-shaped 4f-shell and small M will be lower in energy. The lowest order anisotropy constant, for example D or B_4^0 will have a positive value. If there are two negatively charged ligands coordinating from opposite sides of the ion, an oblate shaped 4f-shell corresponding to a high M will be energetically favored. The magnetic moment will align along the, so-called, easy axis of anisotropy.

2.5 X-ray absorption techniques

In addition to scanning probe techniques, X-ray absorption spectroscopy, performed in the group of Prof. Wolfgang Kuch, was used in this work. In particular, X-ray magnetic circular dichroism (XMCD) and X-ray natural linear dichroism (XNLD) was applied to determine the magnetization of a rare earth metal center of a molecular complex and the orientation of the atomic axis of the ion. The orientation of the ligands of this complex upon adsorption on the sample surface was determined by a combination of STM and the near edge X-ray absorption fine structure (NEXAFS). To illustrate how atomic orbitals affect the X-ray absorption cross section, the formula for the cross section will be derived following the description in the book of Stöhr [58].

In X-ray absorption spectroscopy, electrons from the completely filled inner shells of the atoms of one element are excited into empty states by an X-ray beam of a specific energy, polarization and incidence angle [58]. The latter two can be represented by the electric field vector $\vec{E}$ as well as the vector potential of the magnetic field $\vec{A}$. In absence of charges, as in a traveling electromagnetic wave, using the Coulomb gauge the two

quantities are simply related by:

$$\vec{E} = \frac{1}{c}\frac{\partial \vec{A}}{\partial t}. \tag{2.29}$$

Here, as in the rest of this section, cgs units are used following the work of Stöhr [58]. To illustrate the interaction between light and matter, an example plane wave can be plugged into the Hamiltonian of the excitation.

$$\vec{A} = \vec{\epsilon} A_0 \cos(\vec{k}\cdot\vec{r} - \omega t) = \vec{\epsilon}\frac{A_0}{2}(\mathrm{e}^{i(\vec{k}\cdot\vec{r}-\omega t)} + \mathrm{e}^{-i(\vec{k}\cdot\vec{r}-\omega t)}) \tag{2.30}$$

Due to the Coulomb gauge (equation 2.29) the unit vector $\vec{\epsilon}$ of the $\vec{A}$-field is identical to that of the $\vec{E}$-field in a plane wave. The magnitude of the wave vector is determined by the photon energy $\hbar\omega$ as $|\vec{k}| = \frac{\omega}{c} = \frac{2\pi}{\lambda}$, with λ being the wavelength. $\vec{k}$ and $\vec{\epsilon}$ are perpendicular to each other. The photon flux I of this plane wave, which is the number of photons per area per time, is the ratio of the energy flux of the electric field $\frac{E_0^2}{8\pi}$ and the photon energy.

$$I = \frac{E_0^2 c}{8\pi\hbar\omega} = \frac{A_0^2\omega}{8\pi\hbar c} \tag{2.31}$$

With that we can define the X-ray absorption cross section σ_X as the excitation probability $\Gamma_{i\to f}$ divided by the photon flux.

The transition probability is given by Fermi's golden rule. Within the time dependent perturbation theory the Hamiltonian of the atom is known while the interaction with the electromagnetic field is added as the perturbation. It is convenient to use the vector potential, since it directly enters the Hamiltonian of the interaction of an electron in an electromagnetic field. The perturbation has the form [13]:

$$V = -\frac{e}{mc}\vec{A}\cdot\vec{p} + \frac{e^2}{mc^2}\vec{A}^2. \tag{2.32}$$

For a many electron system $\vec{p}$ is the sum of all momenta of each individual electron and m is the corresponding sum of all their masses. The second term can be neglected as the numeric coefficient is very small. Within the so-called dipole approximation, the factor $\mathrm{e}^{\pm i\vec{k}\cdot\vec{r}}$ in the expression for $\vec{A}$ in Equation 2.30 is close to 1 and can be neglected as well. This is a consequence of $\vec{r}$ being much smaller than λ in typical atoms for X-ray energies.

Plugging the perturbation 2.32 into Fermi's golden rule, we obtain the transition rate to be:

$$\Gamma_{i\to f} = \frac{2\pi}{\hbar}\frac{e^2}{m^2c^2}A_0^2|\langle f|\vec{\epsilon}\cdot\vec{p}|i\rangle|^2\rho(\mathrm{E}_f). \tag{2.33}$$

Here, $|i\rangle$ and $\langle f|$ are the initial and final state and $\rho(\mathrm{E}_f)$ is the density of states at the energy of the final state that is probed by the spectroscopy. The expression 2.33 can be rewritten in terms of the position operator $\vec{r}$ using the relation $\langle f|\vec{p}|i\rangle = im\omega_{fi}\langle f|\vec{r}|i\rangle$ with $\hbar\omega_{fi}$ being the energy difference between the initial and the final state [13]. The X-ray cross section thus becomes:

$$\sigma_X = 16\pi^2\frac{e^2}{\hbar c}\hbar\omega|\langle f|\vec{\epsilon}\cdot\vec{r}|i\rangle|^2\rho(\mathrm{E}_f). \tag{2.34}$$

Two different X-ray techniques use Equation 2.34, XPS and XAS. In photoemission spectroscopy X-rays above the ionization energy excite the electron into a vacuum state. The energy of the free electron can be measured to determine the binding energy of the original core electron. In this work X-ray absorption spectroscopy (XAS) is used. X-rays probe empty bound states by exciting the core electron into these.

A major consequence of equation 2.34 are the dipole selection rules that explain the shape of the measured spectra. If we express the initial and final states in terms of spherical harmonics $R(r)Y_{lm}(\theta,\phi)$, then, within the dipole approximation, it can be shown that the indices l and m have to change each by $\pm1, 0$ [51]. l is called the orbital quantum number and is connected to the total angular momentum of the electron $\vec{L}$ by the relation $|\vec{L}|^2 = \hbar^2 l(l+1)$. m in turn is proportional to the projection of the angular momentum onto the z-axis. The spin of the electron is conserved [13].

From the s-shell the core electron is excited into the p-shell, which is called the K-edge in X-ray notation. From the p-shell (L-edge) the electron can be excited into an s-shell or a d-shell and so on. After the excitation of the core electron, the remaining hole has a total angular momentum $j = l \pm s$. The states differ in energy by the spin-orbit interaction leading to separate peaks in XAS for the corresponding states, e.g. L_2 with $j = 1/2$ and L_3 with $j = 3/2$. The projection of the total orbital momentum m_j of the excited electron, in turn, changes by 1 (-1) for right (left) polarized light [51].

Following the creation of the core hole, Auger processes take place leading to the emission of electrons from the atom. These secondary electrons either leave the sample or excite further secondary electrons that leave the sample. The emission of electrons in a metal sample can be conveniently used to experimentally determine the intensity of the X-ray absorption [58]. By measuring the electric current between the sample and ground the total electron yield, the amount of all electrons escaping the sample is determined. Since the travel path of electrons in the solid is very short, only X-ray absorption near the surface of the metal is measured.

2.5.1 Angle dependency of the K-edge

The analysis of the peak intensities near a particular absorption edge in X-ray absorption spectroscopy (NEXAFS) allows to determine the orientation of empty states like molecular π^*-orbitals and thereby the orientation of adsorbed molecules.

As we see in equation 2.34, the intensity of the XAS signal is directly proportional to the scalar product of the polarization vector of the X-ray beam and the position operator of the involved states. For an excitation from an isotropic core state with s symmetry, the spatial extent and orientation of the final state determine the value of the scalar product. Varying the incidence angle of the X-ray beam will change the intensity from an oriented final state like an empty π^* molecular orbital, making the orientation measurable.

A scaling factor $I(\theta)$ of the XAS intensity for a tilt angle θ of the probed final state of the excitation can be derived from equation 2.34. Instead of the position operator $\vec{r}$ we take a unit vector $\vec{o}$ in the direction of the orbital [59]. Let φ be azimuth angle of $\vec{o}$ and ϑ the angle to the surface normal. For a random distribution along the azimuth direction the product of the orbital vector and the polarization vector is averaged over it. With ϕ being the azimuth angle of the polarization vector, the scaling factor becomes:

$$I(\theta) = \frac{1}{2\pi}\int_0^{2\pi} (\vec{o}\cdot\vec{\epsilon})^2 d\varphi = \frac{1}{2\pi}\int_0^{2\pi} \left(\begin{pmatrix} \sin\vartheta\cos\varphi \\ \sin\vartheta\sin\varphi \\ \cos\vartheta \end{pmatrix} \cdot \begin{pmatrix} \sin\theta\cos\phi \\ \sin\theta\sin\phi \\ \cos\theta \end{pmatrix} \right)^2 d\varphi \tag{2.35}$$

$$= \cos^2\vartheta\cos^2\theta + \frac{1}{2}\sin^2\vartheta\sin^2\theta \tag{2.36}$$

Measuring the XAS intensity at two different angles, the tilt angle of the orbital can be determined. Since $\theta = 0°$ would correspond to propagation of the X-rays in the surface plane and is therefore not possible, typical values for the two angles are $\theta = 20°$ and $\theta = 90°$. From the ratio of the two intensities the average tilt of the orbital can be deduced.

As can be further seen in equation 2.36, recording the XAS at the so-called "magic angle" of around $\theta = 55°$ gives an intensity that is independent of the tilt angle. This is useful for comparisons to bulk or powder measurements or to measurements with unpolarized light.

2.5.2 X-ray Natural Linear Dichroism

A dichroism is the difference in absorption spectra for two different polarization states of light. The dependence of absorption on the orientation of linear polarized light described above is an example of linear dichroism. Another example is the determination of the magnetization by XA spectroscopy in rare earth atoms that has been described by Goedkoop and Thole [60, 61]. In the following the XNLD and XMCD techniques are described for the case of lanthanide magnetism.

As has been described before, in a ligand or crystal field the shape of the electron density of the 4f-shell is distorted from spherical symmetry, resulting in a magnetic moment. However, the distortion from spherical symmetry also leads to an angular dependence of XA intensities. As a consequence of the localized behavior of 4f electrons the intensities can be accurately simulated by atomic multiplet calculations using the so-called Cowan's code [62, 63].

The code of Cowan computes the wave functions, energy levels and dipole transition probabilities using the Hartree-Fock method. The wave functions are represented by a linear combination of Slater-determinants, the so-called multiplet.

The absorption process at the M edge of a lanthanide atom involves the electronic excitation of an electron from the 3d shell to the 4f shell:

$$3d^{10}4f^{n}|\alpha JM\rangle \rightarrow 3d^{9}4f^{n+1}|\alpha' J' M'\rangle$$

where α labels all quantum numbers except for J and M. While the initial state $|\alpha JM\rangle$

is the Hund's rules ground state and therefore unique, the final state has two open shells with potentially thousands of multiplets. Hundreds of these multiplets can be reached by dipole transitions that have to satisfy the conditions $J' - J = -1, 0, 1$.

The square of the transition matrix element and hence the cross section of the excitation can be factorized according to the Wigner-Eckart theorem [60, 63, 61]. The first factor is the square of the so-called Wigner 3j-symbol. The second factor is the reduced dipole matrix element, which is independent of orientation of the angular momentum [60].

$$\sigma^m_{\alpha J M \alpha' J' M'} \propto \begin{pmatrix} J & 1 & J' \\ M & m & -M' \end{pmatrix}^2 |\langle \alpha J || C^{(1)} || \alpha' J' \rangle|^2. \tag{2.37}$$

Here, $m = 0$ holds for linearly polarized light and $m = \pm 1$ for right or left circularly polarized light parallel to the magnetic field orientation. While the second factor, the reduced dipole matrix element, is proportional to the total strength of the spectral line, the square of the 3j-symbol determines how the total line strength is divided up among the individual line components. The 3j-symbol is responsible for the dependence of the cross section on the temperature and the magnetization [63]. With the degeneracy in M lifted, the states with the energetically lowest M are occupied according to the Boltzmann distribution $e^{\frac{\varepsilon(M)}{k_B T}}$. If, for example, the degeneracy is lifted by a magnetic field, then the levels split due to the Zeeman energy $\varepsilon = \mu_B g_j M B$. The temperature and field dependent cross section becomes [60]:

$$\sigma^m_{\alpha J M \alpha' J' M'}(B, T) \propto A^m_{JJ'}(B, T) |\langle \alpha J || C^{(1)} || \alpha' J' \rangle|^2, \tag{2.38}$$

where $A^m_{JJ'}(B, T)$ is the Boltzmann-weighted average of the 3j-symbol with $k_B T$ as the thermal energy

$$A^m_{JJ'}(B, T) = \frac{\sum_{M=-J}^{J} \begin{pmatrix} J & 1 & J' \\ M & m & -M' \end{pmatrix}^2 e^{\frac{\varepsilon(M)}{k_B T}}}{\sum_{M=-J}^{J} e^{\frac{\varepsilon(M)}{k_B T}}}. \tag{2.39}$$

The spectra at the M_5 edge of lanthanide metals typically consist of three characteristic

peaks that correspond to the change of $\Delta J = 0, \pm 1$. For these peaks the factors $A^m_{JJ'}(B,T)$ in the case of linearly polarized light take the following form [60]:

$A^0_{J,J+1}$	$A^0_{J,J}$	$A^0_{J,J-1}$
$\frac{(J+1)^2 - \langle M^2 \rangle}{(2J+3)(J+1)(2J+1)}$	$\frac{\langle M^2 \rangle}{J(J+1)(2J+1)}$	$\frac{J^2 - \langle M^2 \rangle}{J(2J-1)(2J+1)}$

(2.40)

Here, $\langle M^2 \rangle$ is the Boltzmann average of M^2 in the same manner in which the 3j-symbol is averaged in Equation 2.39.

The practical consequence of the relations 2.40 is that the relative peak intensities at the M_5 edge can be used to determine the square of the magnetization produced by the 4f-shell. A higher absolute value of magnetization in the direction of the polarization of light comes along with a higher intensity of the central $\Delta J = 0$ peak and lower $\Delta J = \pm 1$ side peaks.

Although Zeeman splitting has been considered in the above derivation of the result and not the case of crystal or ligand field splitting, ligand field effects can be studied using linearly polarized X-rays without a magnetic field [64]. Further, the ligand field parameters are part of the modeling of the spectra in the code of Cowan. Therefore, the linear dichroism in the absence of a magnetic field can be quantitatively evaluated simulating the XA spectra.

2.5.3 X-ray Magnetic Circular Dichroism

While the linear dichroism discussed before gives insights into the absolute value of the magnetization, circular dichroism is directly proportional to the magnetization itself.

To get an idea of the mechanism, one can look again at an excitation from an inner shell to a partially filled shell such as at the $L_{2,3}$ edge of a 3d transition metal or the $M_{4,5}$ of a rare earth. The absorption cross section of such an excitation depends on the occupation of the different Zeeman-split states and hence on the magnetic moment.

The amplitudes of the $\Delta J = 0, \pm 1$ intensities at the M_5 edge of lanthanide atoms as described in Equation 2.40, evaluated analogously for right- and left circularly polarized light $A^{\pm 1}_{J,J'}(B,T)$, have the following values [61]:

$$A^{\pm 1}_{J,J+1}(B,T) = \frac{(J+1)(J+2) \pm (2J+3)\langle M\rangle + \langle M^2\rangle}{2(2J+3)(J+1)(2J+1)} \tag{2.41}$$

$$A^{\pm 1}_{J,J}(B,T) = \frac{J(J+1) \mp \langle M\rangle - \langle M^2\rangle}{2J(J+1)(2J+1)} \tag{2.42}$$

$$A^{\pm 1}_{J,J-1}(B,T) = \frac{J(J+1) \mp (2J-1)\langle M\rangle + \langle M^2\rangle}{2J(2J-1)(2J+1)} \tag{2.43}$$

Here again, the thermal dependence from left hand side is in the Boltzmann weighted average of the quantum number M. For each peak at the M_5 edge, the difference in intensity between the left and right polarized light, which is defined as the XMCD signal, is proportional to the thermal expectation value of the projection of the total angular momentum onto the z-axis and therefore to the magnetization.

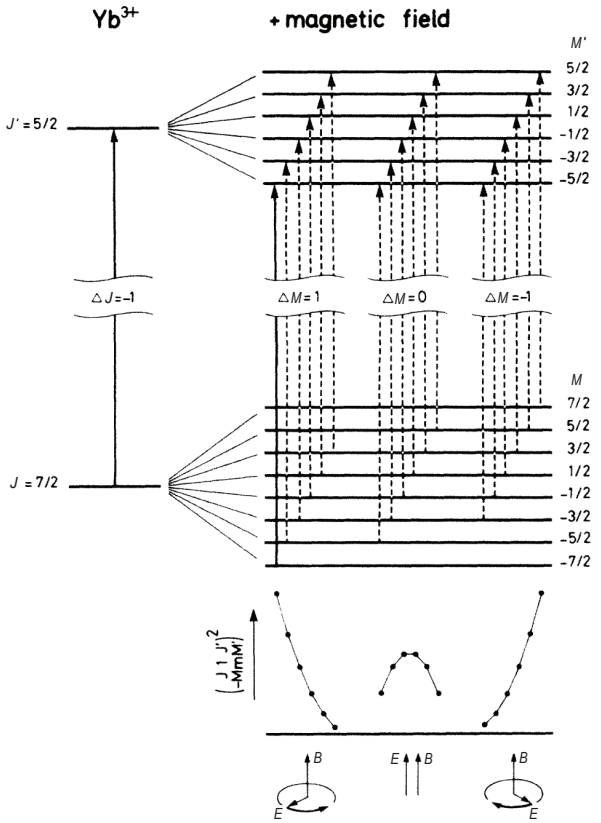

Figure 2.8: From [61, 65]: Left: Energy levels of the $3d^{10}4f^{13} \rightarrow 3d^9 4f^{14}$ transition of Yb^{3+} without a magnetic field; Right: degeneracy in M split by magnetic field. Dipole allowed transitions $|JM\rangle \rightarrow |J'M'\rangle$ indicated by the arrows, relative intensities given by the dots. Bottom: relative amplitudes of the dotted lines as given by the square of the 3-j symbol. The polarization of the light with respect to the magnetic field $\vec{H}$ required for the different ΔM channels is indicated at the bottom. Only the $M = -\frac{7}{2} \rightarrow M = -\frac{5}{2}$ line of the $\Delta M = 1$ channel indicated by the solid arrow is allowed at 0 K.

To get a more intuitive picture of the mechanism of the XMCD signal, we examine the spectroscopy of Yb^{3+} atoms from the thesis of Goedkoop [61, 65] that is depicted

in Figure 2.8. The spectrum consists of only the one $\Delta J = -1$ line at the M-edge, the transition $3d^{10}4f^{13}(^2F_{\frac{7}{2}}) \rightarrow 3d^9 4f^{14}(^2D_{\frac{5}{2}})$, while the M_4 line is dipole forbidden. A magnetic field H splits the energies of the initial and final levels by $-g\,\mu_B\,B\,M$. The dipole allowed transitions are indicated by arrow lines and grouped according to the ΔM and the corresponding three polarizations left and right circularly polarized and parallel linearly polarized.

If all levels were populated equally, no difference in absorption would arise for left and right circularly polarized light, as seen in the squares of the Wigner 3-j symbols that are proportional to the transition matrix element. Since the levels are populated according to the Boltzmann distribution, more transitions from lower lying initial states are available for absorption of left circularly polarized light and less absorption of right circularly polarized light takes place. The difference in absorption between the two polarizations is defined as the XMCD and is proportional to the magnetic moment of the probed atom. In the limit of 0 K only one transition is possible, the one that is indicated by the solid line in the Figure. The absorption line then is not visible for right circular polarized light nor for linear parallel polarized light.

2.6 Literature review on Tetrathiafulvalene and Tetracyanoethylene

Before the data on the charge transfer complex TTF/TCNE on Au(111) are presented, a brief overview of known results for the individual components on the surface will be given. This will give a basic understanding of the interactions between the surfaces and the molecules that will be helpful for the more complicated case of the mixture.

In general a molecular charge transfer complex consists of a donor molecule that typically shows a low ionization potential and donates electrons from the highest occupied molecular orbital (HOMO) to the lowest unoccupied molecular orbital (LUMO) of an acceptor molecule that is more electronegative than the donor. Energetically the complex is stabilized by the Coulomb attraction between the ions that compensates for the energy cost of the ionization of the two molecules. In the case of planar donor and acceptor molecules the Coulomb attraction between the centers of charge and hence the centers of mass of the molecules favors stacked configurations.

Noble metal surfaces readily donate or accept electrons, but are not particularly electropositive or -negative. Charge transfer with typical donors or acceptors still takes place. In particular tetrathiafulvalene (TTF) and tetracyanoethylene (TCNE) show charge transfer among others on the (111) surfaces of gold and copper, respectively, as will be recapitulated in the following.

2.6.1 TTF on Au(111)

The presence of charge transfer in the donor molecule TTF on the Au(111) surface was shown by STM and DFT by Fernandez-Torrente *et al.* [66] The adsorption of a molecular electron donor on Au(111) is characterized by the spontaneous formation of a superlattice of monomers spaced several nanometers apart caused by an intermolecular long-range repulsive potential. As can be seen in Figure 2.9 f)-h) the TTF molecules form arrays of monomers along the face-centered cubic fcc regions of the Au(111) herringbone reconstruction with a homogeneous pair distance of the monomers. Upon increase of molecular coverage this pair distance decreases as is plotted in Figure 2.9 i). The TTF molecules evidently repel each other and are forced to smaller distances by the abundance of molecules and the preference for the fcc sites over the hcp sites of the herringbone reconstruction. The repulsive interaction responsible for this is the Coulomb interaction

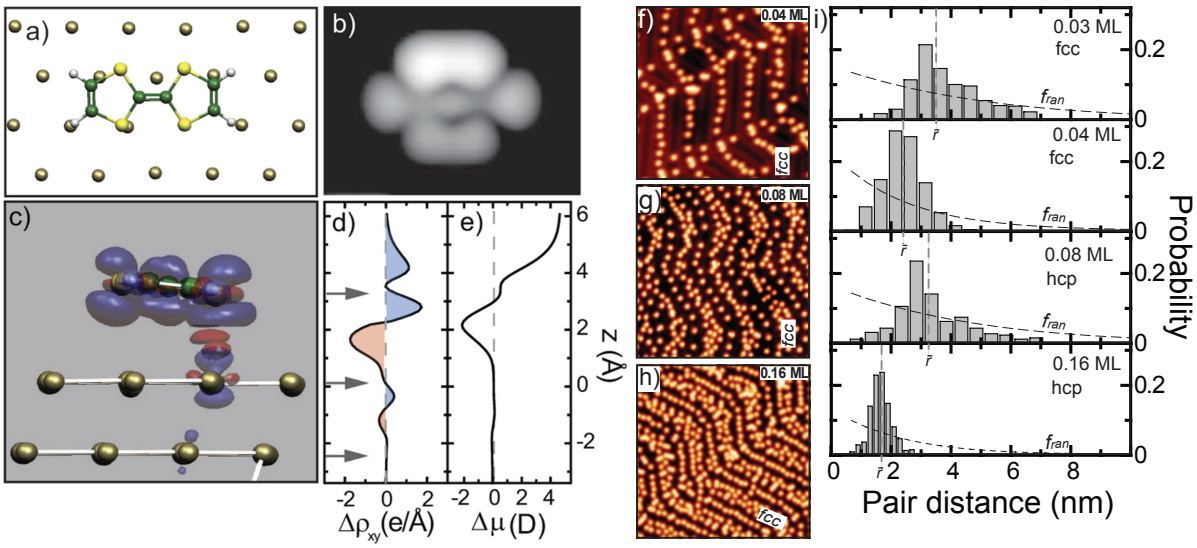

Figure 2.9: Results from DFT simulations and STM experiments [66] a) Fully relaxed configuration of TTF on Au(111). The uppermost two gold layers as well as the molecular degrees of freedom are relaxed until atomic forces are lower than 0.01 eV/Å. b) Tersoff-Hamann constant current image [15] of the molecule in a) (V=-0.5 V). c) Induced electronic density by the molecule surface interaction. d) Lateral (x-y planes) integration of the induced charge. The arrows show the vertical distance values at which the two topmost surface layers and the two binding S atoms lie. e) Accumulated induced dipole. Together with (d), it reveals that the molecule becomes positively charged. f)–h) STM images of TTF on Au(111) at various coverages. i) Pair distributions f of the one dimensional TTF arrays for the data shown in f) –(h). For 0.08 and 0.16 ML, the distributions are performed on hcp regions. More than 500 pairs are analyzed in each plot. The molecular coverage is determined from STM images of large surface areas, assuming that 1 ML corresponds to 2 molecules/nm^2. From the lowest to the largest coverage, an average pair distance is obtained $\overline{r}$ of 3.5, 2.5, 3.3, and 1.7 nm in the one-dimensional arrays. The corresponding 1D distribution functions for non-interacting particles f_{ran} are included.

as follows from ab-initio calculations of charging of the TTF on Au(111) [66].

The local interaction character between the surface Au and the S atoms of the TTF implies a sizable bonding strength and a large charge donation into the surface. Indeed, the adsorption energy after dipole corrections is -0.86 eV, and the surface to molecule distance is 2.76 Å. The electronic structure of the S atoms has a large contribution in the HOMO, which causes a large redistribution of electronic charge (Figure 2.9(c)). The charge donation is expressed by a partial decrease of the electron density in the whole molecular plane. The result is a positive charging of the molecule and the creation of a surplus of negative charge localized close to the S–Au bonds. Figure 2.9 (d) shows the

planar integration of charge. An excess of positive charge (∼0.6 e) is located around the molecule, and the corresponding screening negative charge (∼-0.4 e) is between the molecule and the first atomic layer.

While the molecule itself is rather flat, the TTF is tilted along the long axis of the molecule as can be seen in the calculations as well as in the STM images that are well reproduced by the Tersoff-Hamann simulations in Figure 2.9 (b). This tilt is due to the rather local interaction of one sulfur atom with one gold atom rather than a van-der-Waals interaction of the conduction electrons of the surface with the molecular orbitals of the TTF [66].

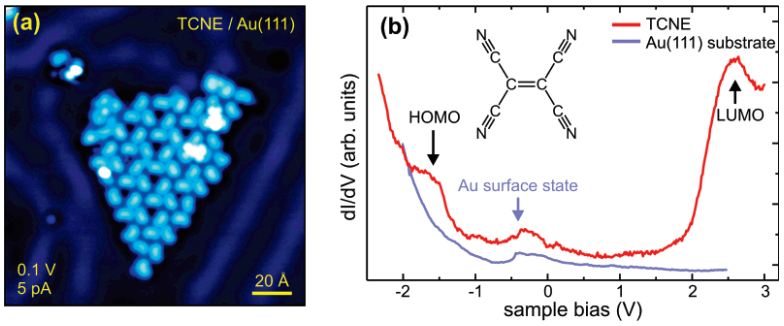

Figure 2.10: STM results of TCNE adsorption on Au(111) [67]. a) TCNE molecules order in a loose hexagonal pattern within the fcc domains of the Au(111) herringbone reconstruction. b) STS of TCNE/Au(111) shows a HOMO resonance at -1.5 eV and a LUMO resonance at +2.5 eV.

2.6.2 TCNE on Au(111)

In contrast to TTF, TCNE does not show charge transfer on the pure Au(111) surface as has been shown by Wegner *et al.* [67]. Figure 2.10 shows that TCNE adsorbates form open, loosely ordered islands within the larger (fcc) domains of the Au-herringbone reconstruction. Each molecule appears as an elongated protrusion in the STM topography (∼6 Å × 9 Å) with a slight kidney-like shape. Theoretical LDOS isosurfaces of TCNE in the planar view are square-like with clearly distinguishable nodal planes as opposed to the kidney-shaped molecules experimentally observed. Therefore the TCNE is likely not oriented with its molecular plane parallel to the Au(111) surface plane, but rather "side view" of the orbital is imaged. Tunneling spectroscopy of TCNE/Au(111) (Figure 2.10 b) shows peaks at -1.5 V and +2.5 V relative to the Fermi energy ($V = 0 \equiv E_F$), which are

assigned to the HOMO and LUMO states, respectively. TCNE molecules on Au(111) are easily manipulated by the STM tip as opposed to the copper (100) surface where chemisorption and charge transfer occur. The difference is explained by comparison of electron affinities (EA) of atomic and molecular elements as referenced to the neutral species. Atomic Au has the larger EA, 2.31 eV, of the two substrates and therefore is less likely to establish a strong charge-transfer bond by donating electrons to the TCNE molecules (EA = 3.17 eV). The intermolecular interaction dominates the TCNE behavior and TCNE cyano groups are not tightly bound to the Au substrate, leading to an out-of-plane ordering.

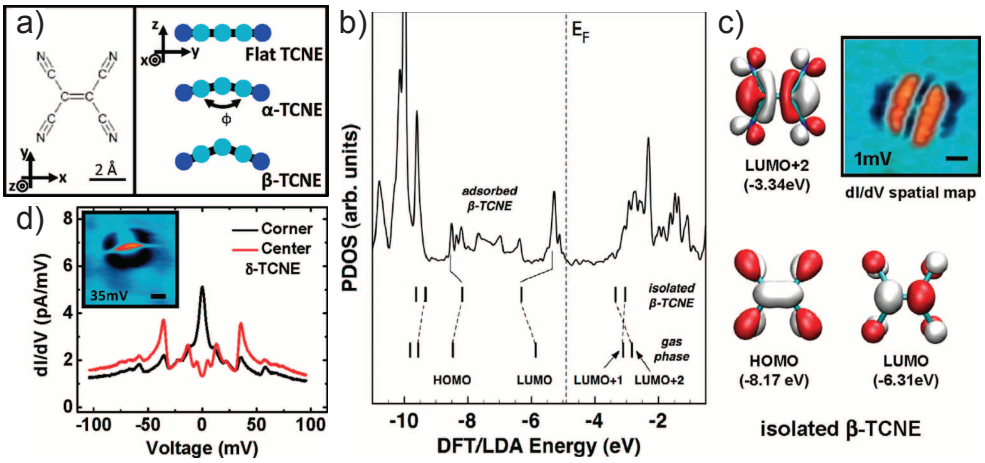

Figure 2.11: Charge states of TCNE on Cu(111) from [68]. a) Chemical structures of TCNE with illustration of bending angles of doubly charged α and β-states. b) The calculated LDOS of β-TCNE adsorbed on Cu(111). Molecular orbitals for isolated β-TCNE and isolated planar TCNE are shown for comparison. For clarity, orbitals are labeled by their occupation in planar TCNE. c) Calculated molecular orbitals for isolated β-TCNE. Also shown is the measured spatial map of the Kondo resonance from δ-TCNE, taken at 1 mV. d) Comparison of spectra with the tip over the corner and center of δ-TCNE at 5.3 K. Kondo side bands corresponding to inter- and intramolecular vibrational modes are more prominent with the tip over the center of the molecule. The inset is a spatial map of the dI/dV signal at 35 mV. Scale bars in insets of c) and d) are 5 Å.

2.6.3 TCNE on Cu(111)

While the difference in electron affinities of pure TCNE and the Au(111) surface is not sufficient to lead to charge transfer, electron donation from the more electropositive Cu(111) to TCNE is observed by STM [68]. Since the overall behavior of single TCNE

molecules on Cu(111) is strikingly similar to that of TCNE in the TTF/TCNE complex on Au(111) it will be described briefly.

TCNE adsorbs onto terraces of a cold (5.3 K), Cu(111) surface in five different states labeled α to ϵ [68]. Single TCNE molecules are reversibly switched between these states by applying voltage pulses with the tip of the STM. From α (and β) the molecule switches to δ via γ by applying a negative voltage, while the switching in the reverse direction occurs for the opposite polarity. Upon elevating the temperature to 55 K all molecules switch to the thermodynamically stable β-state. In Figure 2.11 a) the chemical structure as well as the bending configurations along the C=C bond of the α- and β-states deduced from DFT calculations are shown. As can be seen from the projected density of states of the β-state in Figure 2.11 b) the LUMO lies completely below the Fermi-level and is therefore occupied by two electrons. This result is in agreement with spatial dI/dV mappings at positive bias (Figure 2.11 c)) showing a density of states distribution resembling a higher unoccupied orbital. According to the calculations the orbital in question is the LUMO+2 which lies lower than the LUMO+1 due to the bending of the molecule (labeled by occupation in planar neutral TCNE). However Mulliken population analysis gives a net charge transfer from Cu to TCNE of ~0.4 e. In a back back-donation process [69] ~1.6 e are thought to be transferred from lower-lying orbitals of TCNE near E_F to the Cu surface.

Among the five states the β-and the δ-states are those with identical adsorption site and orientation, which makes them the relevant case for comparison to the TCNE in the rigid charge transfer complex. The δ-TCNE exhibits a butterfly-like shape and appears much taller than the other configurations, which is believed to be additional deformation related to the central C=C bond of the molecule. While no peaks that can be attributed to molecular orbitals are seen in dI/dV in the stable ± 0.5 V range, δ-TCNE shows a pronounced peak at the Fermi energy due to the Kondo effect as well as several vibrational sidebands all shown in Figure 2.11 d). The occupation of molecular orbitals in δ-TCNE must be distinct from the other states, since unpaired spin near the Fermi level is required for the Kondo resonance. On basis of DFT calculations it is reasoned that a lengthening of the C=C bond leads to a partial occupation of the LUMO+2 in δ-TCNE.

As can be guessed from the above studies the combination of the two molecules will form a charge transfer complex on the Au(111) surface in the following manner. The TTF

molecules donate electrons to the surface and the surrounding surface poses electropositive centers for attachment of the electron acceptor TCNE. The Coulomb attraction between the molecules and surface and the TCNE forces the molecules into the plane. The situation for the TCNE is then similar to that on Cu(111) with the interesting difference that it has no rotational or translational freedom in the plane due to steric hindrance by the TTF neighbors. Since TCNE is prone to switching between molecular deformations on the surface, it might also do so on in the charge transfer complex. This is what will be described in the following chapters.

3 Charge transfer complex TTF/TCNE on the Au(111) surface

Microscopic degrees of freedom are suitable for information storage or computing. As miniaturization approaches molecular scales the question arises whether and how information can be stored in single molecular arrangements. The challenge for basic research is to find as many answers to this question so that engineers of later generations with superior technologies have a wide choice of working principles to choose for the design of actual computing machines.

Even though the general physical principles are known at least in theory or from experiments in other fields, the interplay of different effects is beyond imagination or theoretical modeling and has to be tested experimentally.

The basic concept of digital computing is the bit, a unit of information that can have one of two values, and may therefore be physically implemented with a two-state device. The two memory states can be implemented in various ways, magnetization, resistance or holes in punched cards. For computation purposes however, it is necessary to be able to switch between the two states. In abstract terms the device is represented by a double well potential with stable states at the opposite ends and a set of stimuli to overcome the potential barrier. In the study presented here, the charge transfer complex composed of the electron donor molecule tetrathiafulvalene (TTF), the electron acceptor molecule tetracyanoethylene (TCNE) and the (111) termination of a gold single crystal is utilized to build a two-state device. The design for a memory array of single molecular bits and working principles of initialization readout and writing will be presented in the following two chapters.

The present chapter introduces the charge transfer complex TTF/TCNE on Au(111) and explores in detail the correlation of Kondo effect and molecular conformation of the acceptor molecule [70].

3.1 Deposition of the compound onto the surface

Both molecules, TTF and TCNE, were evaporated from powder by heating the respective evaporant to 315 - 320 K inside a pumped sealed glass tube connected via a leak-valve to the preparation chamber. A submonolayer of TTF was evaporated by placing the sputtering-annealing cleaned, < 220 K cold Au(111) crystal in front of the open leak valve for about 10 minutes. The very volatile TCNE was deposited by flooding the chamber with TCNE via the leak-valve to pressures above 10^{-8} mbar for a similar amount of time, effectively depositing more than 20 Langmuir of the substance. In order to obtain a submonolayer of the TTF-TCNE compound in the desired 1:1 stoichiometry the sample crystal was then annealed from 220 K to about 300 K, which is above the evaporation temperature of TCNE from the Au(111) surface but below the evaporation temperature from the coordinated structure with TTF, leaving only the coordinated TCNE on the surface.

3.2 Adsorption geometry

The TTF-TCNE mixture orders in three different phases of ordered molecular islands that are shown in the STM image Figure 3.1 a). The island in the middle consists of the checkerboard ordered phase in the upper part and the ordered rows of the more complicated row phase that is described in detail later. These two phases with interesting physical properties are the ones where the number of TTF molecules equals that of TCNE molecules. The left island exhibits a structure with an excess of TTF that is different from the two named structures. The TTF excess structure exhibits some similar properties as the other two, but the data is far less conclusive and further discussion of it will therefore be omitted.

The arrangement of the molecules in the checkerboard phase is shown as an overlay on the STM images in Figure 3.1 b) and that of the rows structure in d). From the STM image we conclude that the TTF and TCNE molecules assemble in ordered islands with a mainly flat adsorption geometry. Some molecules appear mostly dark on the STM images as if the respective TCNE sites were vacant. This, however, is not the case. The TCNE molecules are present albeit in a low conducting state. Figure 3.1 c) shows the

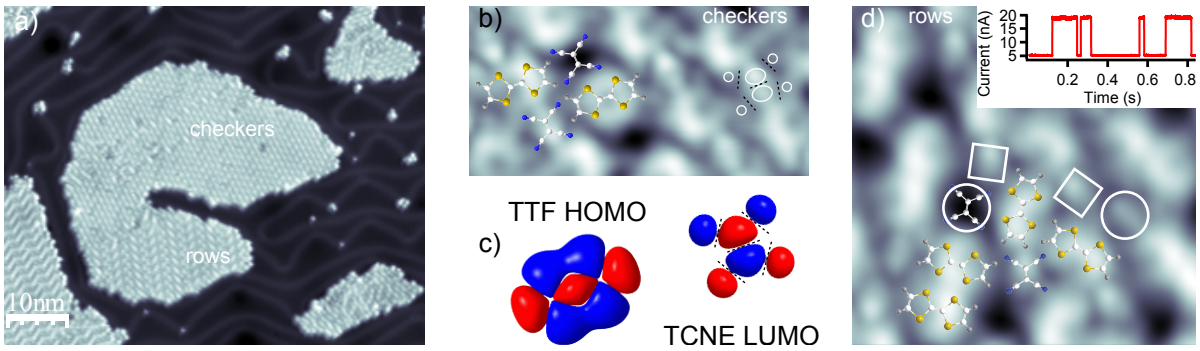

Figure 3.1: STM images of: a) ordered molecular islands on Au(111) surface with three different phases of the mixture; b) checkerboard structure with superimposed structural models of individual molecules at 12 mV, 0.2 nA STM feedback, seemingly missing TCNE molecule is in the low conducting state; white circles (black dashed lines) mark protrusions (depressions) analogously to that in c); c) calculated shape of the frontier orbitals of the acceptor TCNE and donor TTF, dashed lines mark nodal planes of TCNE; d) closeup of the rows phase at -30 mV; inset of d) current trace at -150 mV shows two steps.

frontier orbitals from DFT calculations[1], the LUMO of the acceptor TCNE and the HOMO of the electron donor TTF. These strongly hybridize with the Au states at the Fermi level, as will be shown later. The characteristic shapes of these orbitals are the shapes that are distinguishable in the STM images. TCNE appears with a protrusion around the C=C double bond intersected by the nodal plane through the double bond and surrounded by nodal planes across the single bond to the four cyano groups whose density of states blends in to the neighboring TTF molecules. In Figure 3.1 b) and c) the nodal planes are marked by dotted lines.

The TTF molecules, on the other hand, appear as a tilted donuts, the orientation of which is recognized by the distance to the neighbor molecules. In addition, the approximate dimensions of the molecules from the calculations, which are 4.5 Å×4.5 Å for TCNE and 5 Å×9.5 Å for TTF, match the ones from the STM images.

The most striking property of TCNE molecules in this complex is their switching behavior. In certain bias regimes like at -150 mV the molecules flicker between a high and low conductance state in a distinguished bistable behavior. As can be seen in the current over time trace in the inset of Figure 3.1 d) the molecule transitions randomly between the two states.

The flickering behavior can be easily visualized in STM imaging in Figure 3.2 a). As the

[1]Using the Gaussian 09 package, employing the 6-31G+dp basis set

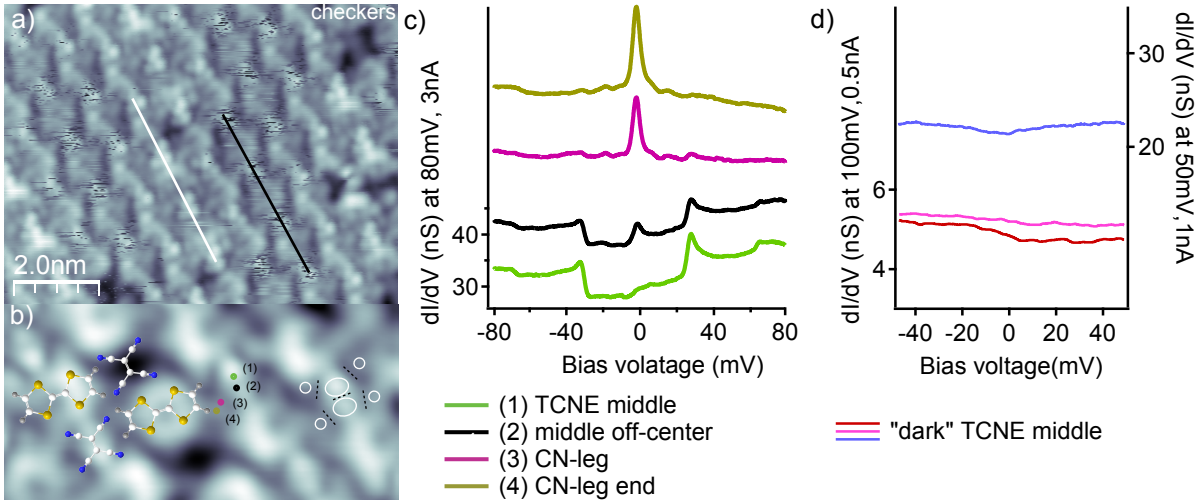

Figure 3.2: a) switching in the checkerboard phase at -350 mV, 0.3 nA; black (white) line on switching (non-switching); b) checkerboard structure at 12 mV, 0.2 nA STM , points (1)-(4) mark spectroscopy shown in c); c) dI/dV on different parts of the TCNE LUMO, vertically offset by 10 nS each for clarity; d) dI/dV on different dark TCNE molecules (not shown).

scanning proceeds in horizontal lines, the switching molecules can be in different states on different lines, leading to stripe shaped artifacts seen in the image. Such artifacts are visible on all images at bias voltages higher than +100 mV or lower than -100 mV. Larger regions with all TCNE molecules switching are interrupted by non-switching rows. The switching TCNEs can occur in single, double or multiple rows; such rows can have different lengths within an island and so forth. Such irregularities are present in the checkerboard phase but are completely absent in the row phase that is more regular and shows as a consequence reproducible switching data in a wider bias and current range. As can be seen in Figure 3.1 d) the row phase consists of alternating rows of pairs of TTF molecules oriented either parallel or nearly orthogonal to each other with TCNE molecules at the edges of the rows. The row phase and its structure along with the switching behavior of both phases will be treated in detail in chapter 4.

Whether charge transfer takes place in this mixture of donor and acceptor molecules and the surface, can be easily concluded from the dI/dV spectroscopy. Figure 3.2 c) shows differential conductance in the meV range around the Fermi level on different positions on the TCNE molecule that are depicted in b). The most prominent spectroscopic feature is the peak at zero bias voltage originating from the Kondo effect that appears on the TCNE LUMO and is absent on the nodal planes of the LUMO. The origin of this effect in

organic acceptor molecules on noble metal surfaces is discussed in previous works [71, 72] and is understood to be the formation of a new many body ground state from conduction electrons of the surface and the electron in the LUMO which is half-filled after charge transfer from the surface or neighboring molecules.

As can be seen from points (3) and (4) in Figure 3.2 c), the Kondo peak is also present between two diagonally adjacent TCNE molecules. In analogy to the case of other organic acceptor molecules [72] the LUMO of TCNE can be assumed to be elongated beyond the molecular backbone towards the cyano legs.

The distribution of charge between the two molecule species and the surface results from an interplay between both species as well as both species and the surface individually. TCNE alone does not exhibit charge transfer on the Au(111) surface due to non-planar adsorption with only two cyano groups oriented towards the metal, while charge transfer takes place on the Ag(100) and the Cu(100) surfaces, where TCNE is planarly adsorbed [67]. In crystals TTF and TCNE stack with the molecular planes facing each other at a distance of 3.1 Å [73] and exhibit charge transfer of about $0.5\,e$ per molecule [73, 74]. TTF on the other hand, is positively charged by about $0.5\,e$ on the Au(111) surface [66]. It is safe to assume for the present case that the electropositivity of the surface is increased by the donation of electrons from the adjacent TTF molecules to the surface facilitating a planar adsorption of TCNE as well as charge transfer from the surface to TCNE. From the presence of the Kondo resonance the amount of charge accepted by the TCNE can be gauged to be $1\,e^-$.

While a transfer of charge directly from the TTF to the TCNE molecule is also imaginable, the center of mass distance between the molecules of $5 - 10$ Å is certainly larger than a typical adsorption distance of 3 Å. Hence, the overlap of the TCNE LUMO with the TTF HOMO is significantly smaller than the overlap of the respective molecular frontier orbitals with the surface states. Therefore, the direct charge transfer is likely to play a negligible role.

Even if the charge accepted by the TCNE does not stem directly from the TTF molecule, the electrostatic potential of the charged neighboring TCNE and the change in local charge on the surface can induce additional charge transfer from the TTF to the surface. Therefore, the charge of the TTF can be assumed to lie between the single TTF case of $+0.5\ e$ and $+1\ e$. Another class of spectroscopic features seen in Figure 3.2 c) are

vibrational excitations that appear on the molecule as small steps. Where the intensity of the Kondo peak is diminished, the steps at ±30 mV that correspond to the rocking mode are of a large intensity that is comparable to the full intensity of the then reduced Kondo peak. This effect was discussed for the similar charge transfer complex of TCNQ with TTF as an interplay between the Kondo effect and vibrations [75]. Alternatively, the convolution of the Kondo peak and the vibrational excitation is an artifact of the actual movement of the molecule due to the excitation of the vibration. No density of states from the LUMO and hence no Kondo peak at zero bias voltage is observed above a vertical nodal plane. At the vibrational excitation energy however, adjacent parts of the orbital move into the junction adding the additional conductance associated with the Kondo state.

The central finding of the present chapter is the absence of the zero bias peak in the dI/dV spectroscopy on the low conducting TCNE molecules. Figure 3.2 d) shows three spectra measured on the central protrusion of three different low conducting TCNE molecules. For better comparability of the feature sizes the spectra are scaled according to their feedback parameters. Beside low-amplitude features that are different for all three spectra and therefore stem likely from tip vibrations, the dI/dV traces are flat. It will be shown in the following that the absence of the Kondo peak is not due to a different charge of the two states of the TCNE but due to differences in the hybridization.

3.3 Molecular configuration of the high and low states

Since the STM apparent heights offer information on electronic density of states and not the actual topography, the images contain only information on the position and orientation of the whole molecule and not on the individual atoms of which the molecule is composed. The low and high conductance of the respective state visible in STM can therefore have either a topographic or an electronic origin or a combination of both. Given that the Kondo-state contributes to the tunneling conduction some electronic contribution is certainly present.

From the point of view of possible applications, an intriguing explanation of the STM contrast would be the switching of charge state that, if true, would certainly result in a change of conductivity. This would pose a sub nano-scale implementation of a charge

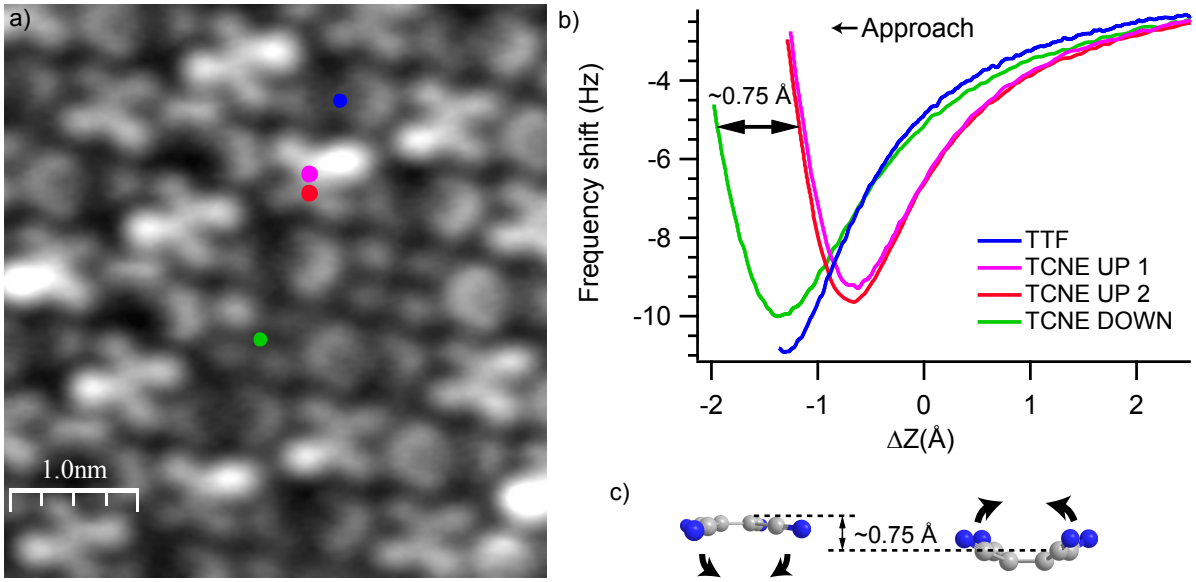

Figure 3.3: a) Constant-height (-2 Å from 57 pA 90 mV feedback) frequency shift df image of a TTF-TCNE molecular island, colored circles mark sites of df approach curves shown in b), the approach axis gives the distance from the constant-height plane fixed at 57 pA 90 mV STM feedback setting on a TCNE down molecule; c) sketch of TCNE bending as measured from approach curves. All data acquired with Xe-functionalized tips.

trap flash cell with a convenient readout mechanism. It will be shown in 3.4 that the two states have at least roughly the same charge.

3.3.1 Determination of topography from frequency shift contrast

To determine the actual topography AFM frequency shift imaging and spectroscopy have been performed. To have a well defined and inert tip apex a xenon atom has been placed on the lowest end of the tip. The interpretation of the constant-height frequency shift contrast depends on the actual height. Figure 3.3 b) shows several df approach curves on different sites of the molecular island that are indicated in Figure 3.3 a). The curves show the qualitative behavior of a Lennard-Jones potential with a long-ranged attractive part stemming from electrostatic forces and chemical interaction of probe and molecule and a short ranged repulsive part originating from the Pauli repulsion of the probe apex atom and the individual atoms that constitute the molecules [76]. The Pauli repulsion dominates the inter-atomic forces at close distances and therefore occurs only between the last tip atom and some few molecule atoms. The attractive force is composed of

several unknown electrostatic contributions from a larger part of the tip and the molecule such as the charges of the probe atom and the molecule or the shape of the metallic part of the tip and hence lacks lateral resolution on the sub-molecular scale. The repulsive part of the df approach curve contains the desired information on atomic heights.

To have comparable height measurements on different molecules, the height was determined from the long-range attractive region of the df approach curves. For this purpose the curves have been fitted with the second derivative with respect to the frequency of the Lennard-Jones potential 2.16 and the long-range attractive potential 2.17. The df signal in the region between 2 Å and 7 Å does not depend on the interaction between the tip and molecules and is therefore not shown in Figure 3.3 b). The df signal in this region depends only on the long-range forces between the tip and the sample at a certain height of the tip above the sample. When the df curves are shifted so that the long-range regions overlap, they are adjusted to the same plane of constant height.

The repulsive parts of the curves measured on the centers of the low (green) and high (red) TCNE molecule are displaced by about 0.75 Å. Hence, the central double bonded carbon atoms have a difference in height above the gold surface of the same amount as sketched in Figure 3.3 c). Thereby a major topographic difference between the two states of the bistability is evident. Analogously, since the plane of constant height of the df image in Figure 3.3 a) lies in the repulsive part of the approach curves for all molecular species, topographic information can be deduced from the df-contrast. At a sufficiently small region of the tip height z the df-z curve can be approximated as a straight line. For a sufficiently planar molecular arrangement, such as present here, the contrast of the image represents not only the frequency shift but also the actual atomic vertical distance to the underlying surface [11].

The deduced atomic configuration sketched in Figure 3.3 c) can be confirmed by simulating the df contrast in different contrast regimes and comparison with the experimental data. In Figure 3.4 a) an STM image of a part of a TTF-TCNE island is shown. The same area is imaged using AFM frequency shift at constant-height at different distances in b) and c). Figure 3.4 d) shows a zoom on two low TCNE molecules.

In order to predict the contrast resulting from various deviations from a perfectly flat adsorption, the df images were simulated using the program of Hapala *et al.* [77]. The df simulations for a model island of 8 TCNE and 8 TTF molecules shown in Figure 3.4 e)

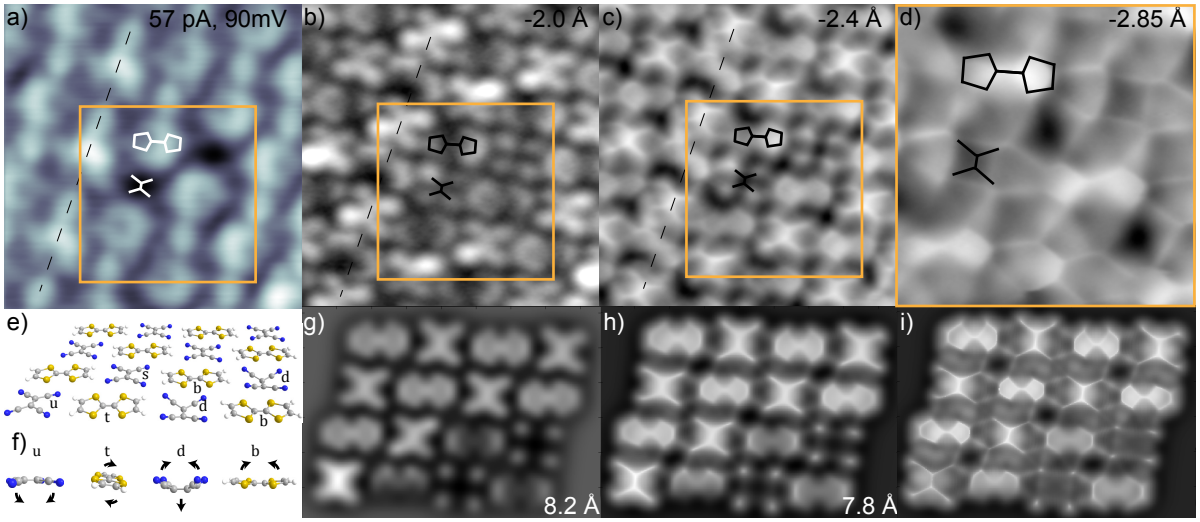

Figure 3.4: a) STM topography of TTF-TCNE island. Dashed line shows not switching TCNE row, two TCNE in the down state are visible on the right; b) - d) constant height (given with respect to feedback parameters in a)) df images at different approach heights (d) is a zoom in to the two low TCNEs); e) model of a TTF-TCNE island arrangement; deformed molecules marked by small letters; side view of the deformations in the lowest row are shown in f); g) - i) simulations of df contrast at different heights using the arrangement in e).

are obtained for three different heights above the surface plane, neglecting effects of charge [78]. The upper two rows of the model island are flat, while the lower two rows are deformed. The deformations of the molecules are sketched and labeled in Figure 3.4 f). u and d label the upward and downward bent TCNE molecules respectively and t and b label the tilted and bent TTFs in Figure 3.4 e) as well as f). Simulated as well as experimental data show the same evolution of contrast towards sharp lines between all neighboring atoms of the same molecule and even of neighboring molecules at lower constant-height planes.

From the qualitative agreement of the experimental data b) - d) with the simulated images g) - i) but also from the experimental data in b) alone one can confirm the sketched bends and tilts. The TTF molecules lie in the aforementioned deformed configurations. The legs of the TCNE molecule are bent in the direction of the surface normal resulting in the central double-bonded carbon atoms pointing either up or down. Thus the bistability has these two configurations as metastable states.

Within the height range that is dominated by the Pauli repulsion, the contrast mechanism varies [77] as can be seen in the qualitative difference between the images Figure 3.4 b)

and d). In b) the molecules resemble an assembly of balls that can be thought of as a convolution of the van der Waals spheres of the scanned atoms and the van der Waals sphere of the apex atom (here a Xe atom). In image d), on the other hand, the molecule rather resembles its skeletal model with rods at the positions of the chemical and hydrogen bonds. Initially, when the repulsive contributions start to dominate the df-image contrast, the functionalized tip and the scanned molecule are sufficiently stiff to not be deformed by the forces between them. When the tip is pushed closer onto the molecule, elastic deformations occur in the tip functionalization. The repulsion between probing Xe-atom and imaged atom becomes stronger than the force associated with the lateral spring constant of the tip apex. This leads to lateral displacement of the probe away from the imaged atom thus reducing the interaction and consequently the frequency shift. Stronger displacement of the tip is forced if the tip apex is placed directly above a center of an atom or a connecting line between atom centers that lie closer than the van der Waals diameter of the apex atom, leading to a higher frequency shift contrast on top of chemical bonds. The closer the bonded atoms are the smaller is the room for lateral relaxation and therefore the higher the frequency shift contrast enabling the discrimination of bond order [79] or hinting to close-lying atoms like in a hydrogen bond [80]. As a consequence of the elastic deformation of the tip the contrast mechanism within the same image varies. In particular, the interpretation of the df-contrast as actual topography that has been used for the image Figure 3.4 b) (same as Figure 3.4 a)) does not hold for Figure 3.4 d). Here, the apparent rods are brighter if they are actually higher as well as when they represent shorter bond lengths. The above presented analysis of height difference is, however, limited to the region of negative frequency shifts where the additional effect of bond lengths on the df-contrast is negligible.

3.3.2 Origin of energy barrier between states

Having established the clear picture of the conformations of the two states of the bistability, the origin of the energetic barrier between them can be deduced. An estimate for the deformation energy of the observed bending in the TCNE can be obtained from the same B3-LYP calculations that also give the frontier orbitals in Figure 3.1. Deforming the molecule along the 17 mV vibrational mode reproduces the bending and increases the energy by about 200 meV. This lies roughly in the same order of magnitude as the perceived energy barrier of 200 meV (estimated in chapter 4). The energy landscape is

governed by the van der Waals interactions and by the energetically stronger chemisorption to the degree that it occurs. The question is, whether the van der Waals forces are sufficient to induce such a strong bending and whether chemical forces that act in the direction of the bending are present.

An obvious contribution is the electrostatic attraction of oppositely charged molecules that squeezes the TTF/TCNE island and by exertion of force parallel to the surface induces deformation of individual molecules. Indeed, the island is densely packed forming a square lattice with a lattice constant equal to the calculated lengths of the molecules. Since there is no space left between the molecules, steric interaction certainly takes place.

Assuming a charge of 0.5 e - 1 e for TTF, -1 e for the TCNE and a lattice constant of 1 nm, the lattice energy per molecule of the TTF/TCNE islands is about 3-4 eV. This lies roughly in the same order of magnitude as the said 200 meV. Since the electrostatic force acts parallel to the surface and the molecule bends perpendicular to it, the force components have to be compared. For an angle of about 10° between the C≡N bond and the molecular plane that corresponds to about 0.5 Å measured height difference of the molecule center and the legs, the force in the direction parallel to the surface lies in the order of magnitude of 0.2 nN. Coulomb attraction at distances of 0.5-1 nm would produce the same forces and hence, would be sufficient to cause the observed bending.

The electrostatic interaction, however, acts mutually on the TTF and the visibly tilted and bent TTF molecules and it is not clear, to what proportions the force is divided between both species. If the deformation energy is divided between both molecular species, Coulomb repulsion alone might not be sufficient to explain the observed geometry of the dark state.

The need for additional effects aside from the squeezing of the island by the electrostatically attracted neighbor molecules is evident from the AFM data. As can be seen from the comparison of the AFM image in Figure 3.4 b) and the simulation in g) the bright TCNE molecules are rather planar with the cyano groups of the different states lying in the same plane. Would the molecule be more bent with the central C=C bond further away from the surface as is sketched in configuration u in Figure 3.4 e) and f), that C=C bond would also appear brighter in the AFM image. Instead, singular cyano legs appear brighter, implying a slight tilt along the diagonal of the molecule. This planar configuration of the bright state at the same distance of the cyano legs to the surface as in the strongly bent

dark state speaks against a squeezing by the electrostatically attracted neighboring TTF molecules as the sole origin of the bent of the dark state.

On the other hand, it is worth noting that cyano groups are bent upwards from the metal surface. Such bending can be facilitated by a slight change of hybridization from sp^2 towards sp^3 due to a backbonding with Au *d*-orbitals. Charge backdonation from transition metals to the strong π-acceptor TCNE is known for $V(TCNE)_2$ films [69] and TCNE on a Cu surface [68]. Bending away of the cyano legs from the metal is similar to the situation in Zeise's salt where the hydrogen legs in the structurally similar ethylene bend away from the central platinum ion [32] or in the similar case of acetylene on the Pt(111) surface [30]. In both cases the atomic d-orbital overlaps with the initially empty π^* molecular orbital and an electron is donated from the d-orbital to the π^* molecular orbital. The interaction of the central C=C double-bond with the d-like valence band would then cause one energy well of the bistability. In the bright state, where the central C=C double-bond is 0.75 Å further away from the surface, the second energy well is formed by the interaction between the electrophile cyano groups and the s-like conduction band. The steric squeezing of the island by the electrostatically attracted neighboring TTF molecules contributes to the barrier between the wells.

The TTF tilt and bending determine the presence of the bistability on the neighboring TCNE molecules. A row of non-switching TCNEs and TTF molecules that are tilted along the long molecular axis (visualized by molecule labeled t in Figure 3.4 e)) is marked by a dashed line in Figure 3.4 a) - c). This is contrasted by TTF molecules that are bent along the short molecular axis with the dithiolium rings pointing upwards. The central double bond of the neighboring bistable TCNE molecules points perpendicular to the short molecular axis of the TTF. The former tilt direction was observed in the case of single TTF molecules on a Au(111) surface [66], which hints at the latter tilt direction being induced by the interaction with the TCNE and therefore a sizable interaction between the two molecule species in the case of the switching TCNE. If the TCNE exerts a force on the TTF that is strong enough to alter the adsorption configuration, it likewise experiences a force from the TTF that contributes to a considerable part of the energy potential of the switching.

In addition to the bending, TTF as well as TCNE molecules show tilts out of the surface plane recognizable by one side of a molecule having a higher contrast than the opposite side. The direction of the tilt does not seem to follow a pattern along the island and is

indeed not necessarily the same for one and the same molecule after several switching events. This is just one of the irregularities of the arrangement in the molecules that are observed in the df images. Beyond the strong distinct deformations described above, both species show further minor deviations from planar arrangements like twists in all possible directions. All of these irregularities in tilt and twist not only change from switching event to switching event but also have an effect on the switching behavior as will be discussed in chapter 4.

3.4 Charge state of conformational states

The two states of the bistability have been shown to differ in conformation. However, the dI/dV data is also pointing to a different charge. The highly conducting state shows the Kondo resonance due to the charge transfer of one electron from the metal to the molecule. It has also a larger average atomic distance to the metal. The low conducting state can be assumed to be stronger coupled and exhibit a stronger hybridization with the metal states. The amount of transferred charge can deviate from exactly one electron, e.g. by a lower Coulomb repulsion energy that comes along with delocalization of the hybridized orbital or by a change in chemical potential upon stronger adsorption. The charging itself could then, if present, contribute significantly to the stability/bistability potential well of the system and is thus important for understanding of and eventual reproduction in different molecular systems. In the following a measurement of the charge of the two states will be presented that shows the charge of the two states to be identical within measurement accuracy.

3.4.1 Measurement of electric potential

Non-contact AFM measurements of the force gradient generally show a bias offset in the minimum of electrostatic attraction between the probe and the sample. This local contact potential difference (LCPD) is caused by the electric field of localized charges and dipoles at tip and sample and can be used to qualitatively investigate them. The exact correspondence between LCPD and electric field can not be determined without the exact knowledge of the electrostatic probe parameters such as its Smoluchowski dipole and are therefore not available. However, in the case of the charge transfer system

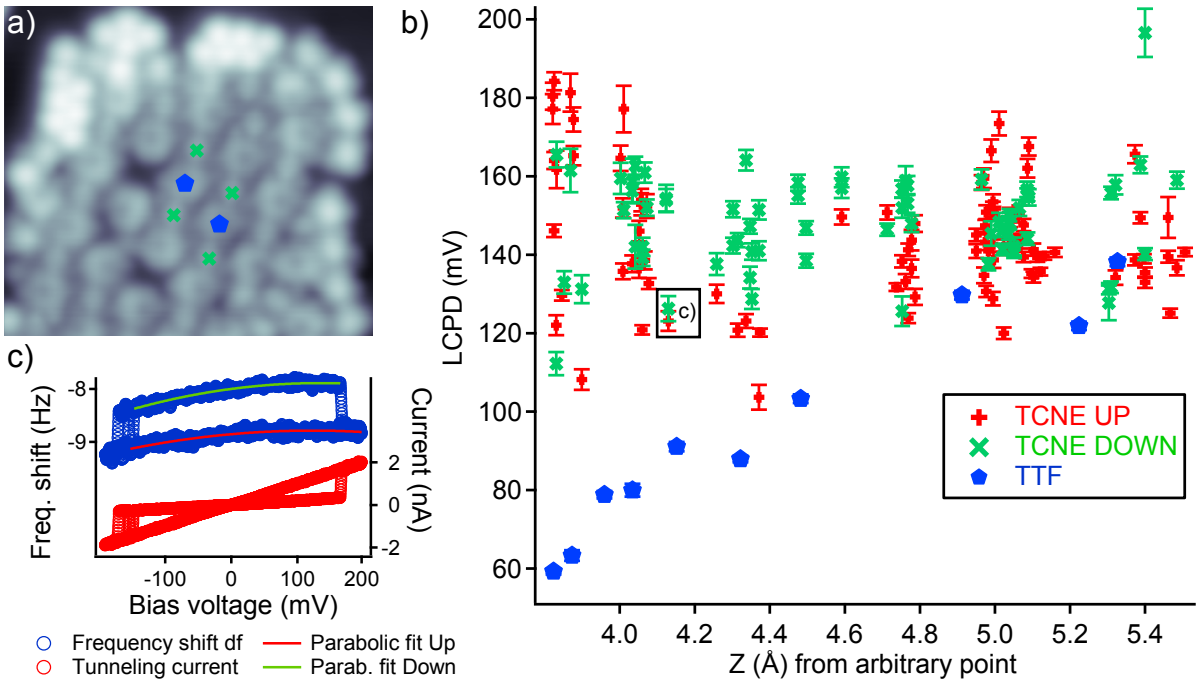

Figure 3.5: a) STM topography of TTF-TCNE island with Xe atoms distinguishable at the upper edge, df vs. bias ramps were measured at two TTF molecules (blue pentagons) and four TCNE molecules (green crosses), c) example df vs. bias and current vs. bias obtained from a TCNE in up and down state - switching between the two is visible in both signals; b) LCPD obtained from the parabolic fit of the df trace vs. vertical displacement on the molecules shown in a)

TTF-TCNE the exact charge of one state of the TCNE is known to be one electron as revealed by the presence of the Kondo resonance. The charge of the TTF, on the other hand, can be safely assumed to be between zero and one donated electron. In order to qualitatively determine the charge of the second TCNE state, the LCPD difference between the high conducting TCNE and the TTF can be used as a gauge.

The LCPD was measured on four TCNE molecules and two TTF molecules of one island as indicated in Figure 3.5 a). Three switching and one non-switching TCNE were used in order to account for variations of charge and steric landscape within the island. The functionalization by Xenon of the Au-tip provides chemical inertness at probe-molecule distances closer than the molecule-surface distance whereby closer approaches and higher spatial resolution can be achieved. During the approach from a constant-current STM feedback set point, the df vs. approach (denominated - Z) curve is recorded. The df vs. Z curve is compared to a Lennard-Jones fit of known height above the gold substrate

in order to obtain the current and molecule-independent approach height that is used in Figure 3.5 b). Figure 3.5 c) shows an LCPD bias ramp taken forward and backward. The high state is distinguishable by its higher conductance. The LCPD is extracted as the maximum point of a parabola fit to the df data. The frequency shift data was drift corrected using an ad hoc model with one linear and one exponentially decaying term and adjusted the first df value of the forward ramp to be the same as the last value of the backward ramp. After this correction, the largest source of error is the combination of noise in the df signal and the rather small region of stability that is available for the fit. In this example the molecule switches in the bistable regime of positive voltages and again in the bistable regime of negative voltages and exposes both states at one fixed height visible in the current as well as the frequency shift signal.

Since the LCPD varies with approach distance, LCPD approach curves such as Figure 3.5 b) rather than single LCPD values have to be taken into account for a meaningful interpretation. At further distances the spatial resolution of LCPD vanishes and the values for all three species cluster around the same value, which can be interpreted as the average value for the island. At closer approach distances the TTF LCPD signal is clearly lower than the TCNE signal indicating the more positive charge localized under the probe as expected. At even closer distances all LCPDs diverge to high values, however, a change in the excitation amplitude of the tuning fork (not shown) indicates that the probe is not necessarily in the non-contact regime and the interpretation of the LCPD changes from simple electrostatic properties of the surface. This leaves a region between 4.0 Å and 4.4 Å where the LCPD has some spatial resolution (as seen in the difference between the TTF and the TCNE) and can be interpreted in a straightforward manner as electrostatic signal of the molecules. Quantitatively, the difference in LCPD between the high and the low TCNE molecules in this region amounts to only 10 ± 15 meV, with the low TCNE showing insignificantly higher values. Meanwhile, the difference between the TTF molecule and the high TCNE, which is to be used to gauge the LCPD, is a significant 50 ± 15 meV. Assuming a charge difference of at least one between donor and acceptor and surface charge as the only source of electric field, the charge difference between the two TCNE molecules is as small as 0.1 ± 0.1 e. We can therefore safely assume the two TCNE states to have roughly the same charge and therefore the charge to have no significant effect on the bistability potential.

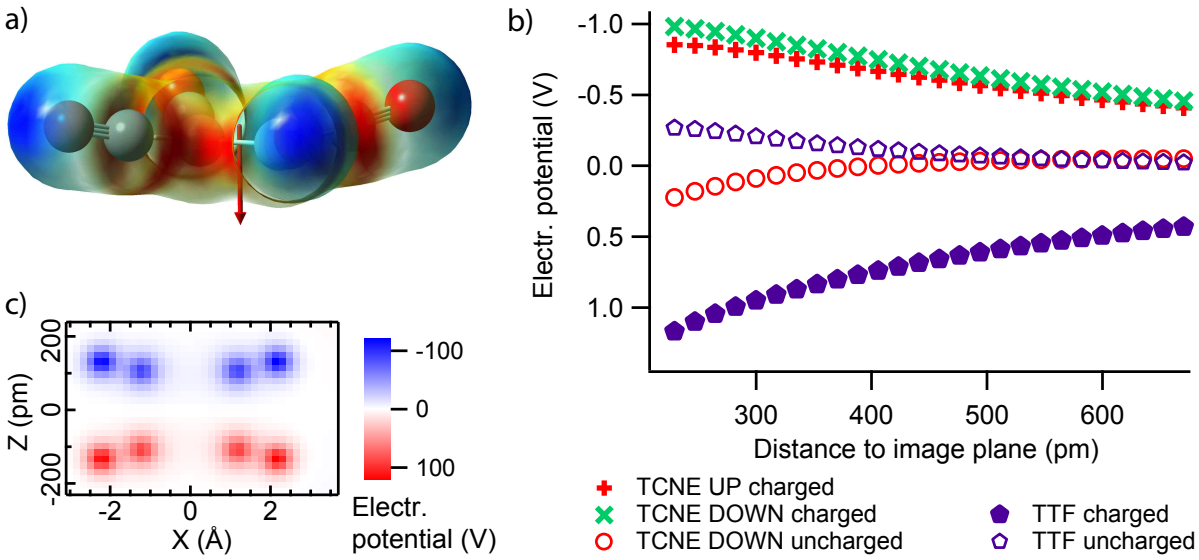

Figure 3.6: a) Total electron density from 6-311+G* B3LYP DFT calculation of a neutral TCNE molecule colored with the resulting electric potential (negative - blue, positive - red) and the electric dipole (red arrow); b) Electric potential averaged over a circle with 2.5 Å radius at various distances to the image plane of an arrangement of molecule and image molecule; c) example for the calculated potential of a negatively charged TCNE molecule and its charge image.

3.4.2 Comparison to simulated potential

The above conclusion is drawn under the assumption that only monopole charges are sources of electrostatic potential. Can we assume on-surface charge as the single source for electric field affecting the probe? Molecular dipoles create electrostatic fields as well. While the electric field of the monopole charge is screened by the image charge of the opposite value in the metal surface, the field of a dipole is enhanced since the image dipole has the same direction. The closer the image plane lies to the charge and dipole the stronger is the screening. For sufficiently small distance the dipole field can dominate the electrostatic interaction or at least make the situation too complicated for interpretation. Indeed, the more negatively partially charged upward bent cyano legs of the low TCNE lead to a dipole of up to 1.2 Debye pointing towards the metal surface while the slightly downward bent cyano legs of the high TCNE lead to a dipole of opposite direction. The sign reversal of the dipole field has to lead to a more positive LCPD for the low TCNE as compared to the high TCNE which indeed is observed to a small degree. The change of charge from more negative in the high state to more positive

in the low state would be observable as a more negative LCPD in the low state which is not observed. Since the two effects compete it is helpful to quantitatively determine the effect of image charges on the electrostatic potential which is done in the following using the electrostatic potential derived from DFT-B3LYP simulations of the molecules and a manual addition of the image potential approximation.

Image charges are a well known mathematical tool from classical electrostatics for the treatment of charge distributions in the vicinity of conducting surfaces. The charge carriers in the conducting surface rearrange to make the electric field lines perpendicular to the surface. This induced charge distribution is idealized as being located on a mathematical surface of zero thickness. In reality, it is spread out extending over a thickness of the order of 2 Å [81]. Whether the method of image charges is valid at distances in the order of magnitude of the size of the surface charge redistribution is not clear a priori. However, density functional theory provided in reference [81] shows that the approximation still holds for the right choice of image plane position. Surface-state and image-state energies can be experimentally determined using photoemission, inverse photoemission, and two-photon photoemission spectroscopies. An estimation of the position of the image plane for different surfaces of different metals has been done in [82].

In the case of Au(111) the image plane lies only a few picometers below the so called jellium edge which is the plane half an atomic layer spacing beyond the outermost atomic layer. A reasonably small center-of-mass distance of TCNE to the image plane lies in the order of 1.4 Å. The calculated spatial potential distribution of a bent TCNE molecule or a TTF molecule is added to its charge-inverted and inversely bent mirror image that is displaced by about 3 Å as seen in Figure 3.6 c). The calculations are done using the well established 6-311+G* basis set and the B3LYP functional implemented in the Gaussian 09 Software package by deforming the relaxed structure manually along the corresponding vibrational mode to achieve a bending compatible to the df contrast data and recalculating the electronic structure and electrostatic potential. Figure 3.6 a) shows the total electron density colored with the electrostatic potential and the dipole that results from the more negatively partially charged cyano legs. Different scenarios of charges of the molecules are compared in Figure 3.6 b). The effect of charge clearly dominates over the effect of the dipole. While the TCNE with the down-pointing dipole has a clearly higher potential than the up pointing dipole, the difference to the uncharged TTF or TCNE is considerably larger. The general trend of the measured LCPD is clearly

reproduced by a rather positively charged TTF and equally negatively charged TCNE molecules. Unlike in the LCPD data the potentials remain distinct at larger distances which is due to the model consisting of only one molecule and not an island of oppositely charged molecules that would yield an average potential at large distance.

3.5 Absence of the Kondo effect in the bent conformational state

As established above, TCNE exists in two equally charged states with one of the states exhibiting a clear Kondo state and the other at least a not visible Kondo state. The change in conformation evident from the df data can be assumed to go along with a change in hybridization with the surface electron states which in turn modifies the Kondo state. Within the formalism of the Anderson impurity model several parameters are governing the Kondo temperature T_K which is the energy scale of the Kondo effect [38].

$$k_B T_K \simeq \sqrt{2\Delta \frac{U}{\pi}} \exp\left(-\frac{\pi}{2\Delta}\left(\left|\frac{1}{\epsilon_S}\right| + \left|\frac{1}{\epsilon_S + U}\right|\right)^{-1}\right) \tag{3.1}$$

Here, ϵ_S is the energetic position of the singly occupied molecular state below the Fermi-level of the surface. Δ is the broadening of that molecular state due to hybridization with surface states. U is the Coulomb energy needed to add a second electron to the orbital. Both, ϵ_S and U, need to be larger than Δ. Since both TCNE states can be assumed to have a roughly similar spatial extension of the LUMO, U is also likely the same. On the other hand, the hybridization strength Δ and the position of the LUMO with respect to the Fermi level are very likely to depend on the adsorption geometry. As seen in the equation 3.1, a too small Δ or a too high ϵ_S, or a combination thereof, may lead to a Kondo temperature that is below the measurement temperature of 4.8 K and therefore a vanishing Kondo effect.

The bright TCNE molecules are flat or only slightly bent with the cyano groups facing the surface. In contrast, the dark TCNE molecules exhibit a bent configuration with the C=C bond being closest to the surface. The closer distance may go along with stronger bonding to the surface and eventually even a stronger hybridization Δ. However, the LUMO features a nodal plane at this position, whereas the electron-rich cyano groups

point upwards. Hence, any directional bonding and hybridization with the conduction electrons of the surface is expected to be small. In addition, the bent configuration rather hybridizes with the energetically lower lying d-band leading to a higher ϵ_S and hence an exponentially lower T_K.

3.6 Summary

The TTF/TCNE on Au(111) charge transfer complex poses an interesting two-state system from the point of view of basic research. The molecules adsorb in a checkerboard monolayer making them easy to investigate by STM. The TCNE molecules occur in two conformational states, which, at liquid helium temperatures, show similar stability. One of the conformations is flat, while the other is bent with the center C=C bond lying closer to the surface. All TCNE are singly charged with a charge of roughly one electron being donated by the surface to the LUMO of the TCNE.

The energy landscape with the barrier between the conformations is dominated by two competing energetic contributions. The first is the π accepting bond between the d-like surface electrons and the central C=C bond of the TCNE molecule. The bond energetically favors the bent configuration due to a rehybridization from sp^2 towards sp^3 at the two central C atoms. The second energetic contribution is the energetically disfavored bending of the molecule that forces it into flat state.

Whether the accepted electron in the LUMO is coupled to the d-band of the substrate or the conduction band changes the Kondo temperature drastically. Plausible trends in the parameters of the Anderson impurity model predict a higher Kondo temperature for the bent state. This is also observed.

Although the TCNE is not a charge switch, it undoubtedly can be used as a memory storage bit with the two conduction states with high on/off ratio as carriers of information. Additionally the Kondo many body state can be switched on and off which might become relevant in quantum information technology.

The route of controlling the switching by the tunneling current is presented in the next chapter.

4 Switching of Tetracyanoethylene in TCNE/TTF on Au(111)

In the following chapter the switching behavior of TCNE/TTF on Au(111) will be investigated in detail. Possible mechanisms will be discussed within the framework of vibrational excitations and the ladder climbing model.

As we have seen, the TCNE molecule is transitioning between two conformational states that have different electronic properties. Since the two conformations interact differently with the surface, with the neighboring molecules and the electric field of the tip, the two switching process directions might also differ and do so as will be described below. Switching from a metastable state to another can be seen as overcoming a potential barrier in a double-well potential. As the system is stable at the bottom of the potential well it has to be excited, either vibrationally within the potential to an energy level that has a smaller barrier to the second stable state, or electronically to an excited state with a potential landscape that has a lower or no barrier to the second state. The slower of the two steps, initial excitation or final transition, determines the overall switching rate. In the case of a vibrational excitation determining the switching rate the number of successive excitations needed can be inferred from the dependence on the electric current. In the case of TCNE the switching direction into the upward bent state (up) is dominated by the initial excitation while the reverse direction (down) is governed by the final transition as will be shown in the following.

4.1 Acquisition of time resolved data

The likelihood of a switching event, the rate, is the essential property of the process that can be easily measured and gives insight into the underlying physical mechanisms. The rate is measured by recording the occupation times of one molecule in a particular state and determining the decay times.

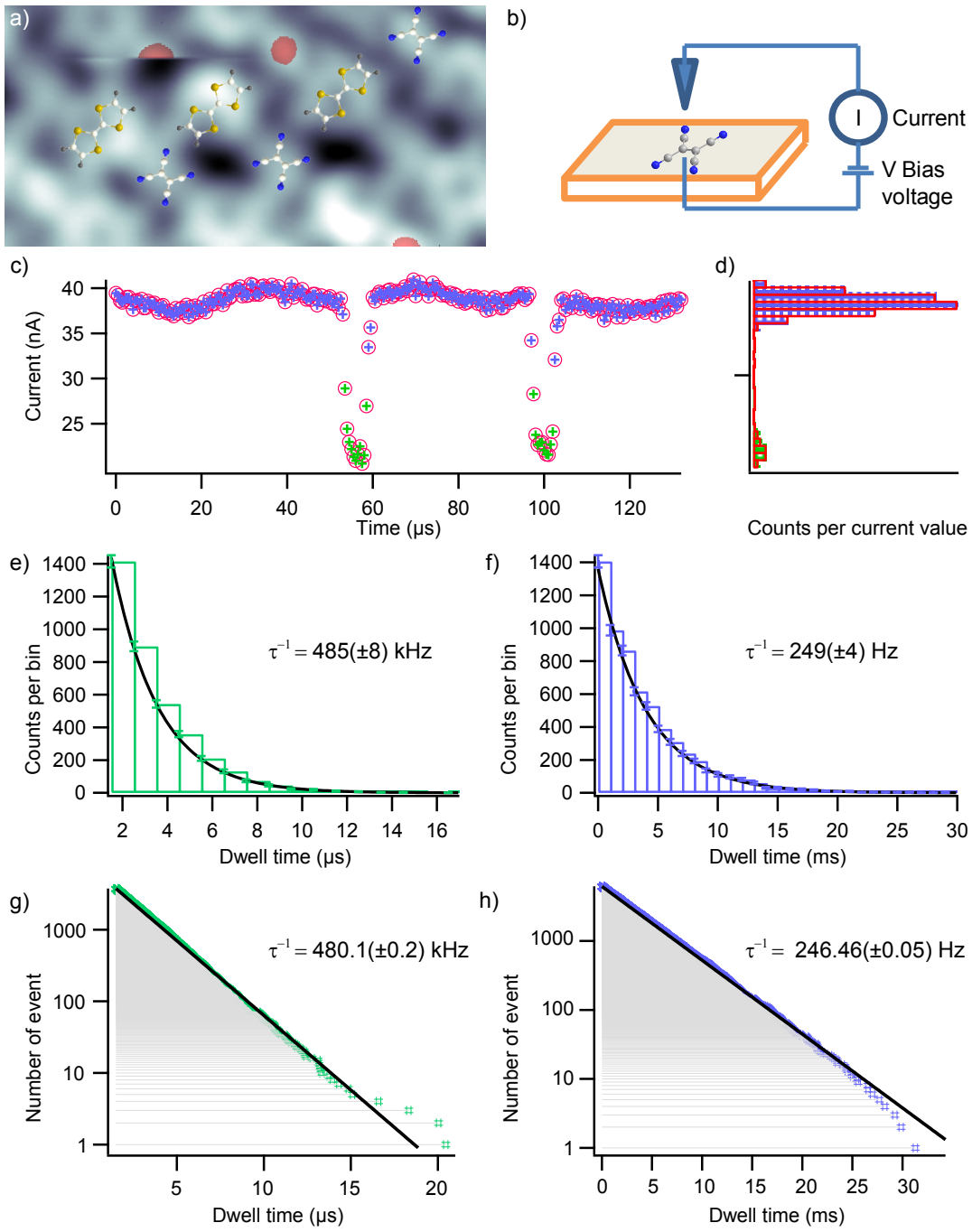

Figure 4.1: a) STM image (-70 mV, 0.25 nA) with overlaid structure models of TTF/TCNE, some switching molecules are marked red; b) sketch of measurement scheme; c) current trace (300 mV); d) histogram of current values shows two maxima low(green)/high(blue); e) f) switching rates up/down obtained from exponential decay rate in histogram of dwell times of low(green)/high(blue) current state; g) h) more accurate evaluation method.

The tip was placed above a TCNE molecule in one of the areas marked red in Figure 4.1 a) and the feedback was switched off while the current was recorded as sketched in b). For the detection of the current a Femto DHPCA-100 IV-converter operating at the bandwidth of 220 kHz was used. With a NI-PXI 5142 digitizer recording traces of 20 s to 100 s at a speed of one million samples per second is possible. Rates within the measurement bandwidth between 10 mHz and 0.5 MHz are detectable[1]. The experiment is performed using several different molecules, the presented data however stems from one molecule for a particular graph of rate vs. current or voltage.

Covering many orders of magnitudes of timescales inevitably goes along with accumulating big amounts of data, several hundreds GB in the present case. Hence the evaluation must proceed automatically, ideally applying the same algorithm on all data sets. This makes the choice of method, how to determine the rate, crucial. The simplest method to determine a rate of switching from one state would be to divide the overall dwell time in this state by the number of the switching events, thus obtaining the average dwell time, the reciprocal of the rate. For this purpose a histogram of the current vs. time trace seen in Figure. 4.1 c) is generated. The overall dwell time is easily obtained as the area of the corresponding peak from a current vs. time histogram as seen in Figure. 4.1 d). The histogram shows also the threshold current that separates the two conductance states. Using this threshold level one can obtain the number of switching events as the number of level crossings in the current vs. time trace, as was done in the present case using the Igor Pro software.

However, this simple method fails at the limit of the measurement bandwidth or slightly outside of it, namely if the average dwell time is longer than the overall measurement time or shorter than the time resolution. Since the switching is a random process (as will be shown), dwell times within the measurement bandwidth are observed for processes with rates that are clearly outside the bandwidth. The bandwidth limit poses a selection bias on the observed dwell times and the limit value itself will appear as the average dwell time rather than the real value. The solution to the limited bandwidth problem is the decay time analysis. In the steady state approximation the solutions of a rate equation follow an exponential decay. In a given time interval the probability for the system to remain in a state decreases by a constant factor. From the histogram of dwell times (Figure 4.1 e),f)), with a suitable bin width, one can see the validity of the steady

[1]This corresponds to a time resolution of 100 s to 2 μs

state assumption and determine the decay constant which is identical to the average dwell time. The problem of the limited bandwidth vanishes as one resorts to compare the probabilities of dwell times that occur within the measurement range. The applicability of the method is limited by the choice of the suitable bin width. A too long time interval reduces the number of bins and therefore the accuracy, while a too short time interval gives too long decay times. The average dwell time method can give an estimate for a suitable bin width but is only applicable within the measurement bandwidth. A manual adjustment of the binning would contradict the requirement of having the same algorithm for all data sets.

To avoid binning the dwell times, one can interpret the measurement of switching events as a decay experiment, where all molecules start in one state and an increasing fraction of molecules decays into the other state over time. Instead of examining many molecules switching one time, we look at one molecule switching. The evaluation is done by putting all dwell times of one state into a descending sorted list of events. Plotting the list index for each event over the corresponding dwell time (see Figure 4.1 g) and h)) reveals the exponential decay of the state over time. The method was used for initialized occupations by Miyamachi et al. [83]. The method behaves considerably more stable in automatic evaluations. Since it contains the same information as the histogram method, no further distinction will be made between the two.

As has been mentioned above, the molecular arrangement shows subtle variations in tilt of the individual molecules that can change from switching event to switching event. It would not be surprising if the switching behavior and therefore the rate, would be affected by the changes in arrangement. And indeed strong changes in the rate of at least one switching direction are observed. This is of course a major complication since the molecular arrangement can be observed only by scanning and not during recording of a current trace. To resolve this complication we assume that there exists one particular arrangement of the whole island that is more likely and more stable and we can still study it neglecting the less stable arrangements that will inevitably decay into the stable one. The part of the data from the unstable arrangements is excluded from evaluation in two ways. First, the occurrence of a second rate can clearly be seen as a second decay time in the histogram of dwell times. In such case only the rate that corresponds to the longer total time spent in the state is chosen as the only investigated one. Second, complete sequences of measurements for a certain bias and molecule are not considered

in the evaluation if the arrangement change is seen in the current trace by eye without further statistical tools. The case is considered instable for further investigation.

The selection procedure is made that strict in order to yield smooth regular dependencies of the rate on current and bias. However, the selection procedure is well-founded since only properties of the current traces themselves and not the rates obtained from them are criteria for selection.

4.2 The ladderclimbing model

The ladder-climbing model has been developed originally for laser induced dissociation [84] and is widely known in transport experiments since the works of D.M Eigler on Xe on Ni(110) [85] and B.C. Stipe on O_2 on Pt(111)[86][87] as well as theoretical literature[88][89] associated with the underlying physical processes. In these works Stipe et al. observed vibrational modes of O_2 on Pt(111) and excited the corresponding vibrations with the electrical current of a scanning tunneling microscope in order to trigger dissociation or simple rotation on the surface of the molecule. The order of the process (the number of electrons needed for a particular dissociation or rotation event) was inferred from the dependence of the rate on the current. The comparison of inelastic excitations visible in dI/dV and the order of the process at each bias voltage showed unambiguously the vibrational modes forming the reaction path. From the order of the process and the excitation energy a measure of the effective barrier can be estimated. In the following the ladder-climbing model will be sketched with a focus on the relationship between the experimental observables and the order of reaction.

The model consists of a set of consecutively excitable vibrational levels (the "ladder") that exist on the left side of a reaction barrier that the molecule overcomes by reaching a sufficiently high level n_{max}. The vibrations are excited by an external stimulus like light, collisions or, in our case, an electric current. The photons, electrons or collision partners need a sufficient energy to excite at least one excitation. Since the potential of vibrational excitations is harmonic, one rung of the ladder is climbed at a time. In the case of an electric excitation the generation of vibrations can be viewed as linear to the electric current [89]. For an external current I and a level n, into which the system is excited, one can define a cross section Φ_n of the interaction with the electron. Then, one can define an effective current $\widetilde{I}_n$.

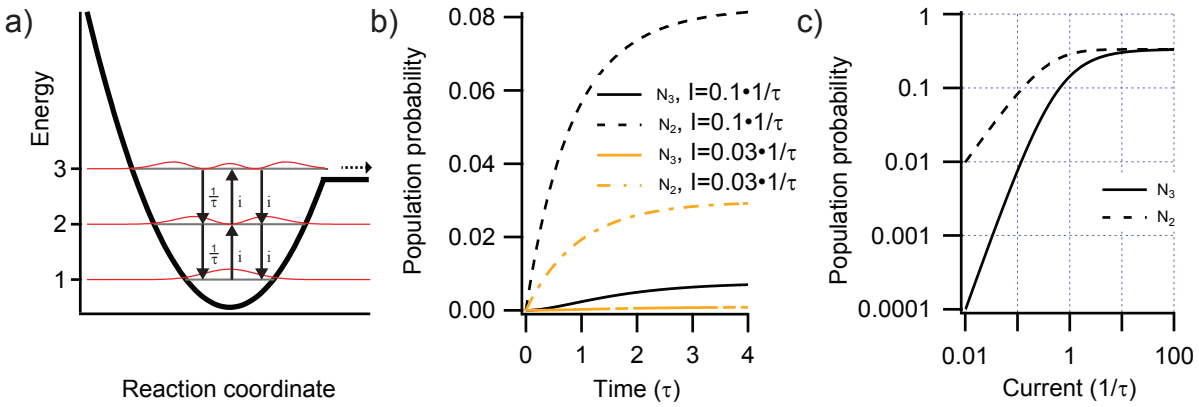

Figure 4.2: a) Sketch of a truncated harmonic oszillator potential with arrows marking excitations/deexcitations between levels; b) population probabilities N_2(dashed), N_3(solid) of the levels 2 and 3 for the currents 0.1 $\frac{1}{\tau}$(black) and 0.03 $\frac{1}{\tau}$ (yellow) ; c) stationary distribution of population probabilities N_2(dashed), N_3(solid) vs. current.

The excited molecule may be coupled to a bath, in our case the surface, which poses a relaxation path from the state n to a lower state after an average time τ_n. Bath induced excitations can be neglected at temperatures low enough that full population of the lowest level can be assumed in the absence of the current. Additionally, the current (or originally the photons) can induce deexcitations from level n with the cross section Φ_n. The situation can be described by a system of rate equations in the form of

$$\begin{aligned}
\dot{N}_1 &= -\widetilde{I}_2 N_1 + \frac{1}{\tau_2} N_2 + \widetilde{I}_2 N_2 \\
\dot{N}_2 &= \widetilde{I}_2 N_1 - \frac{1}{\tau_2} N_2 - \widetilde{I}_2 N_2 - \widetilde{I}_3 N_2 + \frac{1}{\tau_3} N_3 + \widetilde{I}_3 N_3 \\
\dot{N}_3 &= \widetilde{I}_3 N_2 - \frac{1}{\tau_3} N_3 - \widetilde{I}_3 N_3 - \widetilde{I}_4 N_3 + \frac{1}{\tau_4} N_4 + \widetilde{I}_4 N_4 \\
\dot{N}_4 &= ....
\end{aligned}$$

Here, N_i is the population probability of the ith vibrational level. Although the system overcomes the reaction barrier upon reaching $n_{\max}$, this happens on a substantially longer time scale than τ. In this quasi-stationary state, the sum of all probabilities can still be thought of as nearly constant $\frac{d}{dt}\sum_i N_i \simeq 0$ at all times before the switching event.

In order to obtain the experimental observable, the switching rate, the switching is modeled by defining the highest excitable level n_{max} just above the reaction barrier from which the switching occurs with a rate that is proportional to the population probability

$N_{n_{max}}$. The model is then called the truncated harmonic oscillator.

The truncation can be seen as an approximation for either a more realistic potential shape or for vibrationally assisted tunneling [90]. From each level there is a certain rate to tunnel into the other side of the reaction barrier. For levels below $n_{\max}$ however, the tunneling rate is negligible compared to the bath induced relaxation rate into the lower levels. This rate increases for higher levels and dominates for the last level $n_{\max}$ over the relaxation into the lower levels.

Figure 4.2 a) visualizes the model for the simplified case of a system with three vibrational levels and all $\Phi_n = 1$. In 4.2 b) the solutions of the population probability of the second and the third levels are shown for an example currents of one electron per ten(thirty) bath induced relaxation times τ. The system starts with only the lowest level being populated and evolves into a stationary state with constant occupation of all states in the limit of long times. As can be seen in 4.2 c) at low currents the final population probability increases as a power law. Consequently measuring the switching rate vs. the current tells the number of ladder levels needed to switch the molecule and together with the excitation energy an estimate for the barrier height can be obtained.

Besides a direct excitation of vibrations, the electric current can induce excitations into ionic states from which the system relaxes into a vibrationally excited state[91]. Such coherent excitations can excite the vibration along the reaction coordinate by multiple steps in contrast to the incoherent single step excitations described above. The coherent excitations can dominate the reaction process at low currents when the vibrational lifetimes τ are smaller than the average time between successive electron tunneling events [89]. As in the incoherent case, the rate follows a power law dependence on the electric current. Since the power law depends on the height of the reaction barrier, the electron energy and the energy of the vibration mode along the reaction coordinate, different powers are observed for different tunneling bias voltages [86].

Another mechanism that strongly depends on the bias voltages is the anharmonic coupling of a high frequency mode to the reaction coordinate mode [92]. At sufficient energies of the tunneling electron an energetically higher lying mode is excited which then relaxes into the reaction coordinate mode. This is observed as a threshold voltage for a switching with a rate that is linearly dependent on the electric current.

4.3 Order of reaction - estimation of potential barrier height

As we have seen, the TCNE molecule can be switched between two stable states with large on/off conduction ratio that can be used as bits in computation or digital memory storage. In order to explore the possibility of applications and also to obtain a working principle that can be transferred to other molecular systems the energy landscape of the switching has to be investigated in more detail.

The scanned images presented previously were acquired at bias voltages smaller than ±90 mV where no switching up was observed on the timescales of several hours and the switching down showed a rate in the order of magnitude of 0.2 mHz. This makes scanning at the speed of one image per hour possible, which is necessary due to the slow speed of the AFM feedback. From a survey of STM images low rates like the 0.2 mHz or the values in the following two paragraphs can be obtained.

It is noteworthy to point out that there is no detectable threshold voltage for the down switching process. Switching was observed at voltages as low as -1.5 mV indicating a probably thermal activation of the process that will be discussed towards the end of this chapter.

A voltage value of ±90 mV could be stated as the threshold voltage for the switching up based on sporadic occurrence of switching events in STM images at this voltage. However, only two such events were recorded, one at +90 mV and one at −90 mV, which is statistically insignificant. A reasonable definition of threshold voltage would be a voltage above which and within a defined timescale the process occurs with statistical significance. This is the case for voltages above 108 mV for the switching up process, a value that will be discussed in the context of available vibrational modes. The order of magnitude for the timescale and the statistical significance can reasonably be chosen as about two hours and at least ten events at a current below 300 pA. A strength of the electric current has to be postulated since it marks the timescale at which electrons are available for excitation of the switching process. In a very similar voltage range between 110 mV and 130 mV the rate of the switching down increases from the hardly measurable base level of 0.2 mHz to a clear signal in the order of magnitude of around 1 Hz. It is the switching mechanism that dominates above this voltage region that we will focus on in the following.

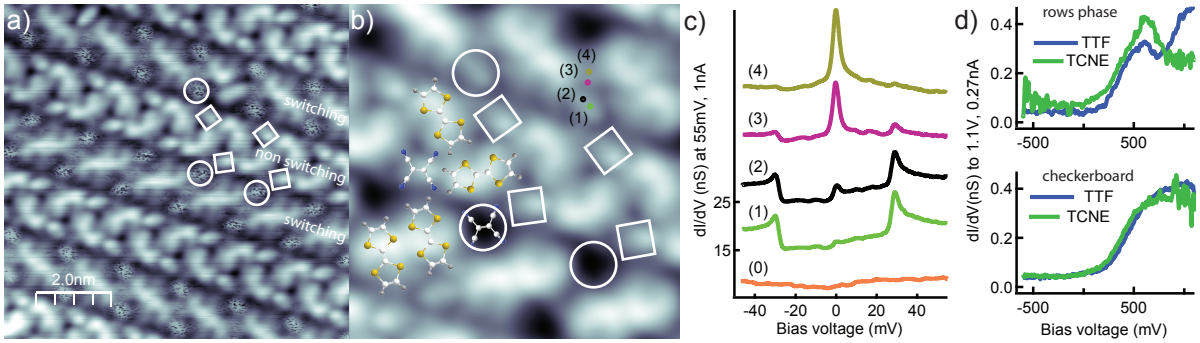

Figure 4.3: a) STM image of bistable molecules in the row phase at -340 mV; white circles(rectangles) mark (non-)switching TCNE, b) Closeup at -30 mV, colored dots mark localizations of spectra shown in c) dI/dV on different parts of the high TCNE LUMO (1)-(4) and a low conducting TCNE (0) (not shown); d) dI/dV on TCNE and TTF, Y-axis scaled as if STM-feedback opened at 1.1 V, 0.27 nA on the TTF and TCNE molecules in the row and checkerboard phase).

4.3.1 Two phases with similar adsorption

In analogy to the checkerboard phase of TTF/TCNE, also the row phase that was introduced in 3.2 exhibits switching between two states and will help to understand the switching process. While the stripe-like row phase appears different from the pattern of the checkerboard phase on the first glance, a closer look reveals that it is rather similar regarding the arrangement of the molecules of the two different species with respect to each other and the resulting interaction between the molecules as well as the interaction of the molecules with the surface. Having two variations of the same energy landscape that are qualitatively similar but quantitatively different, allows experimental access to different parts of that landscape with the same set of some experimental parameters. In addition, a wider range of different experimental parameters is available on the two different phases. In particular, the row phase shows no irregularities aside from island boundaries and survives a higher electrical power before decomposition, allowing a higher portion of the potential landscape to be investigated. The checkerboard phase on the other hand is found more often and is insensitive to impurities during the growth process; therefore more data on it could be acquired in particular AFM topography data.

STM topography and spectroscopy of the row phase can be seen in Figure 4.3. The arrangement consists of rows of 2 TTF and two TCNE molecules. Rows with switching TCNEs alternate with rows of non switching molecules. As can be seen from Figure 4.3 b)

the switching and the non-switching TCNE molecules differ in the orientation with respect to the TTF neighbors and the tilt of the respective TTF neighbor in the same manner as in the checkerboard phase. The C=C axis of the switching TCNE is perpendicular to the long axis of the TTF which is tilted along its short axis. The molecular axis of the non-switching TCNE on the other hand is more parallel to the long axis of the TTF which is tilted along its long axis. The latter tilt direction was observed in the case of single TTF molecules on a Au(111) surface [66], which hints at the former tilt direction being induced by the interaction with the TCNE and therefore a sizable interaction between the two molecule species in the case of the switching TCNE. If the TCNE exerts a force on the TTF that is strong enough to alter the adsorption configuration, it likewise experiences a force from the TTF that contributes to the energy landscape of the switching.

The occurrence of charge transfer between the TCNE molecule in the high conducting state and the gold surface can be concluded in a similar manner as for the checkerboard phase. This is indicated by the very similar appearing peaks at zero bias shown in Figure 4.3 c) that is analogously attributed to the formation of the Kondo state. Just as in the other phase the zero bias peak is located at the cyano legs of the TCNE molecule while the strongly enhanced vibrational steps at about 30 mV are prominent in the center of the molecule. Both features are absent in the low conducting state as can be seen in Figure 4.3 c). Both the Kondo-effect and the vibrational excitations are very sensitive to the interaction of the molecule with the surface. Therefore the similarity in spectroscopy of both states is a sign of a similar adsorption configuration and a similar environment that acts on the TCNE in the two phases.

Information about the distance and overlap of the unoccupied molecular orbitals of the TCNE and the TTF molecules can be inferred from dI/dV spectroscopy in the positive eV range. For better comparison the spectra on TTF and TCNE in the row phase and the checkerboard phase shown in Figure 4.3 d) were scaled to have the same current value at a certain bias voltage. A strong onset of differential conductance can be seen between 300 mV and 400 mV for both molecules in both phases. This similar density of states cannot so easily be attributed to the LUMO of the molecules, since the HOMO of the electron donor TTF is supposed to lie close to the Fermi level and the TTF can certainly be assumed to have a HOMO-LUMO gap in the range of some eV. An explanation has been proposed for similar data on the TTF TCNQ charge transfer complex [93].

Calculations showed the formations of delocalized bands that have been confirmed by the presence of bound states with a distinct dispersion of bound states visible in dI/dV spectroscopy. We did not observe such bound states, since the sharp onset of density of states, which is also the expected energy region for bound states, is outside of the bias range, where the TCNE does not switch. Indeed, the dI/dV presented in Figure 4.3 d) can only be be understood as a weighted average of two dI/dV spectroscopies in which the weighting coefficients are unknown due to unknown residence times of the states.

A considerable overlap of the unoccupied orbitals of the TTF and TCNE molecules in both phases can be concluded, even though the density of states at electron energies above ∼500 mV is increasingly difficult to probe. Since the orbitals are located at the molecules, an overlap hints at a small intermolecular distance and therefore a steric interaction that is similarly present in both phases.

4.3.2 Estimation of the energy barrier height in the row phase

A first estimate of the barrier height can be gained from Figure 4.4. The rates for the two switching directions are measured for different currents at two bias voltages in the regime of predominant occupation in the high state above 200 mV. The data points in Figure 4.4 a) were taken from two different molecules that are shown in Figure 4.4 b). While some outliers are present, the values for both molecules are mostly the same and the data from both molecules can be combined in the analysis.

Figure 4.4 a) shows a linear dependence on the current, which means that single tunneling electrons with these energies can trigger switching events in both directions. From this, a barrier height lower than 230 mV can be concluded.

The rates into the high conducting state at 300 mV are by an order of magnitude higher than those at 230 mV. Following the ladder climbing model this is either caused by the population of higher vibrational levels of the same mode or by the excitation of an energetically higher vibrational mode that allows the transition from the first excited state. An alternative explanation is the interaction with electronic density of states of the high molecule that sets in at this bias voltages and the associated increase in excitation cross section.

The rate into the low conducting state is considerably lower and roughly the same for both voltages. It is, however, governed by the same power law as the rate into the high

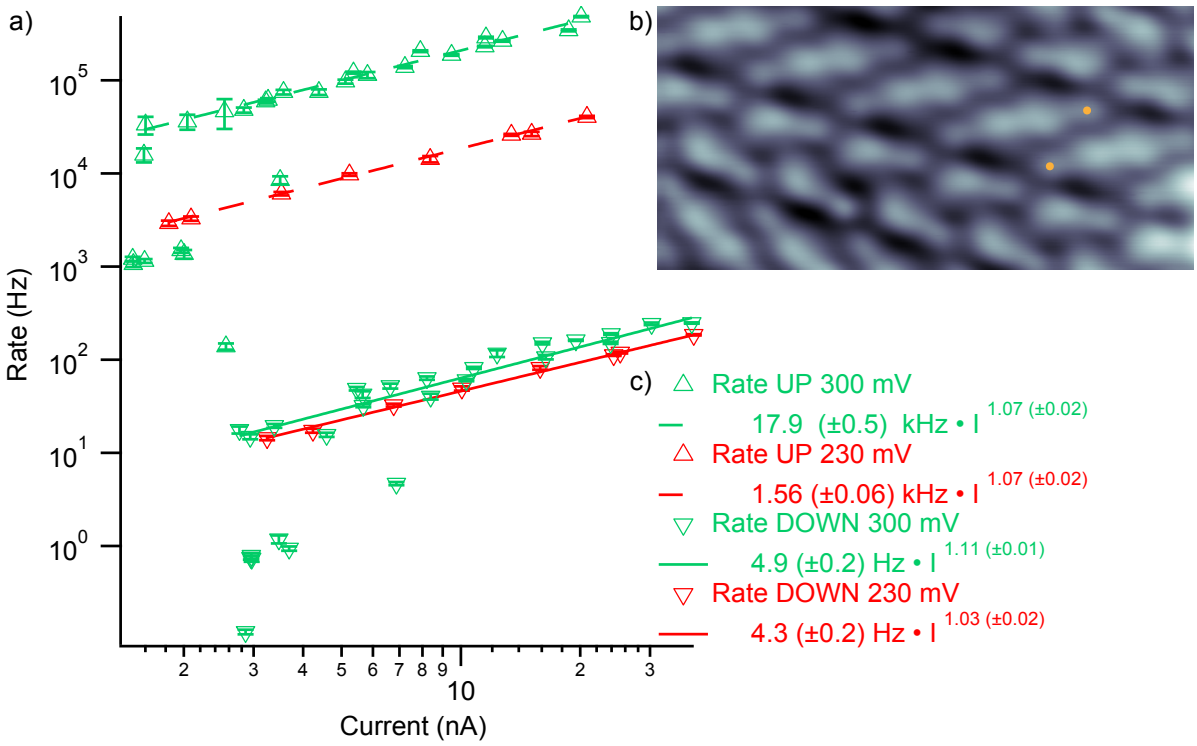

Figure 4.4: a) Rates into high/low state of two molecules shown as up/down pointing triangles for 230 mV (red) and 300 mV (green) in the row phase; power law fits; outliers that are significantly too low are excluded from fits. b) STM image 3nA, 300mV, investigated molecules marked with orange dots; c) fit parameters of power law fit $y_0 + AI^N$.

state. From this it can be concluded that fewer vibrational modes contribute to this direction of the reaction pathway, in particular no modes with energies between 230 mV and 300 mV.

At voltage magnitudes that are about one half of the above mentioned, one tunneling electron is not sufficient to excite a switching event. In Figure 4.5 the rates for both switching directions vs. the current at a voltage of -110 mV that is close to the stability regime of ±90 mV are presented. The rates for both directions are closer to each other than at higher voltages, while the rate of switching up is also orders of magnitude lower. The power law fit for the up switching gives a power $N = 1.88 \pm 0.03$ which corresponds to roughly two electrons needed to switch. At this lower bias voltage vibrational modes that involve stretching of the bonds are not excited by electrons resulting in more electrons needed to overcome the same energy barrier. The deviation from integer values can originate from different reaction paths with different number of vibrational levels

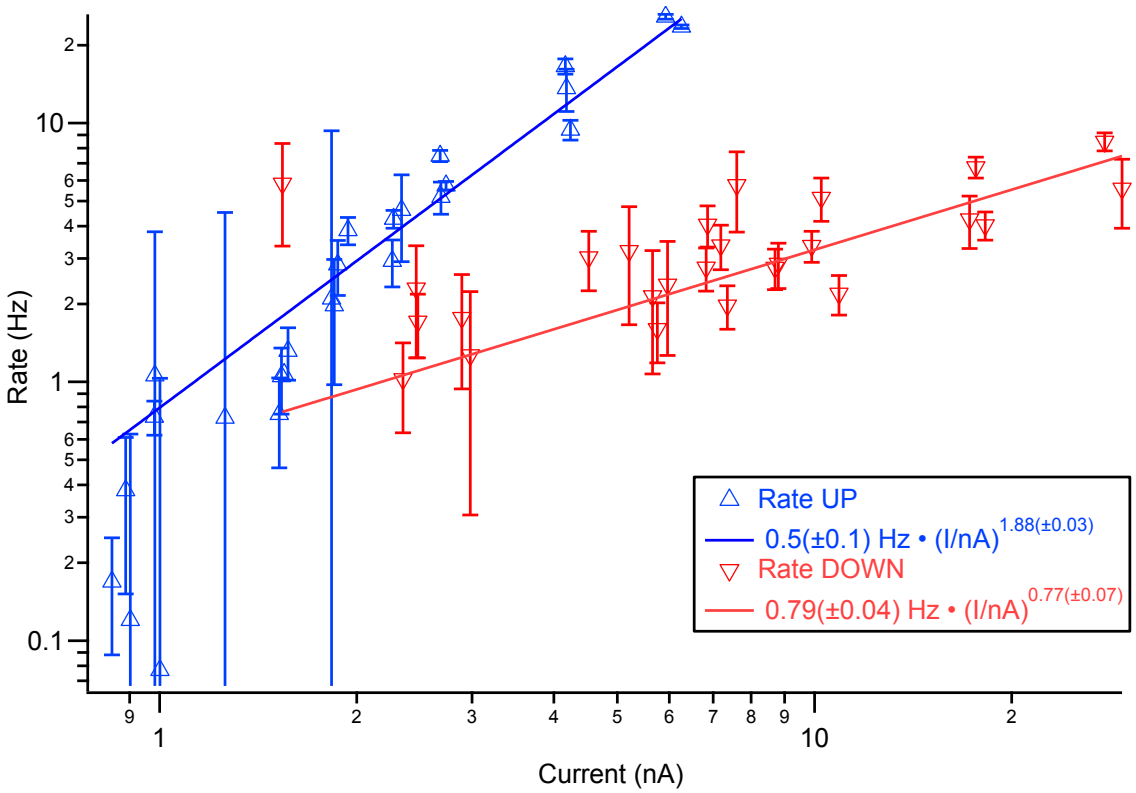

Figure 4.5: Rates into high/low state of two molecules in the row phase shown as up/down pointing triangles at -110 mV in the row phase; power law fits $y_0 + AI^N$.

contributing with different probabilities to the switching. The power-law fit for the down switching direction is not only deviating from integer values, but is also lower than one, a behavior not explained by the ladder climbing model that will be discussed in more detail for the checkerboard phase in the following section.

In Figure 4.6 a) and b) a comparison of rates at a broader voltage range is presented. Rates were obtained at different bias voltages while the current in the low state was kept roughly the same. All rates increase with increasing electron energies. Assuming a current induced mechanism this increase can be interpreted as the onset of energetically higher vibrational modes of the molecule [87], here the 3 C-C stretching modes (124 mV-161 mV), the C=C stretching mode (177 mV) and the 4 C≡N stretching modes (275 mV-283 mV) of the molecule in vacuum[2]. All mentioned modes being in-plane vibrations, none of them is likely part of the reaction coordinate for the observed out-of-plane deformation

[2]According to B3-LYP aug-ccvdz DFT

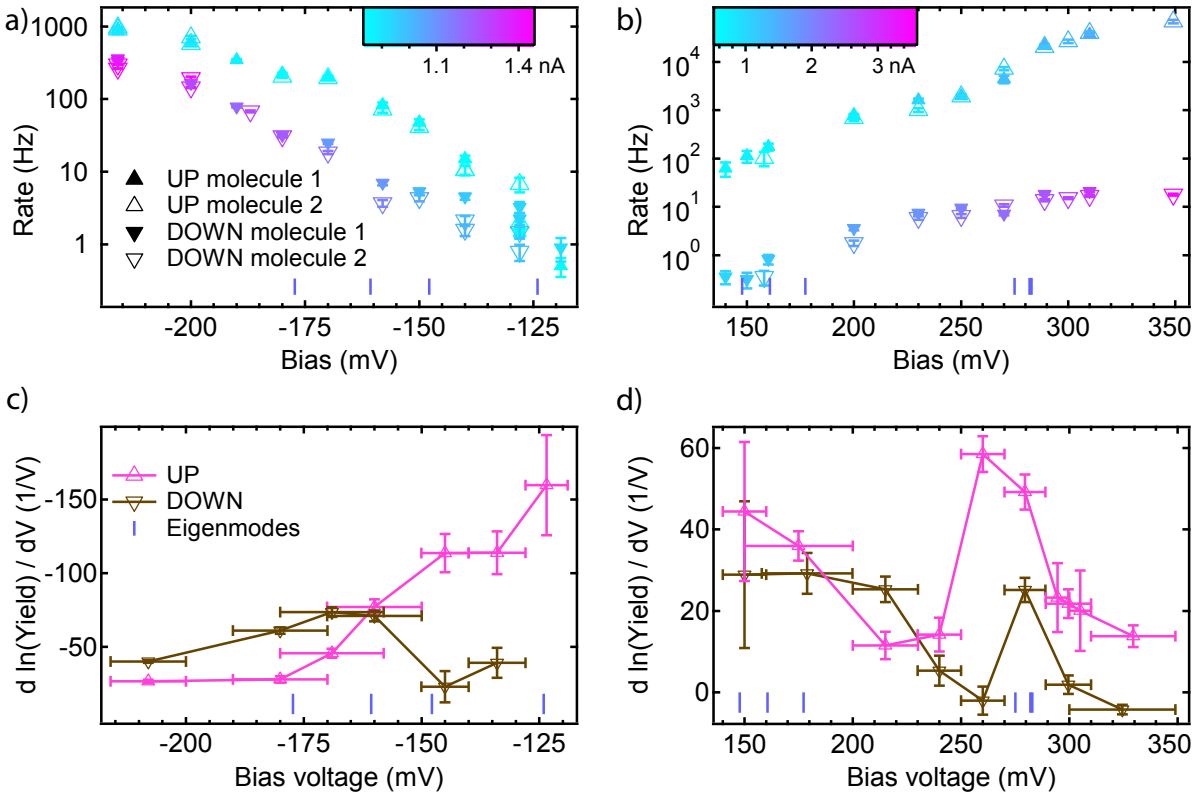

Figure 4.6: a) Rates into high/low state of two molecules in the row phase shown as up/down pointing triangles at negative bias voltages b) at positive bias voltages; color codes indicate current through molecule in original state. c) derivatives with respect to the voltage of the natural logarithms of the per electron yields at negative voltages and d) at positive voltages; pink (brown) up (down) pointing triangles for switching into the high (low) state; blue vertical bars indicate positions of vibrational eigenmodes in the shown range.

of the molecule. Therefore, the increase in rate observed in Figure 4.6 a) and b) can be attributed to anharmonic coupling of these modes to the reaction coordinate. All other vibration modes lie, at least in the free molecule, below 80 mV.

To assign the increase in rate to particular vibrational frequencies, the derivative of the logarithm is plotted in Figure 4.6 c) and d). At both voltages the rate into the high state increases faster than the rate into the low state except in a voltage region around the 177 mV C=C stretching mode. There, switching from the low state into the high state stagnates, while the switching into the low state gains in rate. The opposite situation is observed around the energy of the C-C stretching vibration that is symmetric around the molecular axis at 147 mV. The rate into the low state remains rather constant around

this energy, while the rate from the low state into the high state increases measurably. The different role of different modes speaks for a rather asymmetric shape of the reaction barrier.

The two switching into the low state behaves differently at different bias polarities. While the molecules switch into the high state at similar rates for both voltage signs, the switching from the high into the low state is by two orders of magnitudes slower at positive bias. Effects of the local density of states that can cause such a polarity dependence [94] have been discussed within a resonance model, in which an incident electron becomes temporarily captured by molecular orbitals localized in a resonant state resulting in excitation of molecular vibrations. Although dI/dV as a measure of LDOS is not easily available at all bias voltages at which switching occurs and the LDOS of both states is rather flat in the range of ±150 mV, where the asymmetry of the rates with respect to bias polarity is clearly present already, such effects can explain why the reaction yield is strongly influenced by whether the electron was injected to the molecule or extracted from it.

A scenario with the opposite role of the electronic density of states is thinkable. The electronic density of states of molecular levels that are hybridized with the Fermi level might provide a tunneling path for the electrons with shorter interaction time of the electrons with the molecule and therefore a smaller interaction cross section for vibrational excitations. Such an electronic density of states might be the one visible in the dI/dV above 200 mV in Figure 4.3 d) in the high conducting state. The scenario would explain the present reduction of the switching rate from the high into the low state.

Another prominent feature visible in the increase of switching rates in Figure 4.6 d) is the increase around the energy of the 4 C≡N stretching modes (275 mV-283 mV) of the TCNE molecule. While the increase is very prominent for the up direction and even visible to the naked eye in b), it is much less pronounced for the switching into the low state. Whether this is due to the overall lower rates at positive bias voltages or a result of the asymmetry of the reaction barrier cannot be deduced without comparable data at negative voltages.

In order to estimate the dimensions of the reaction barrier within the truncated barrier approximation, the need for two ladder excitations at 110 mV and for one excitation at 230 mV point at a threshold value of about 200 mV, that has to be overcome. This

barrier height is three orders of magnitude higher than the thermal energy at 5 K, the temperature at which the states are stable, but it is also still two orders of magnitude higher than the thermal energy at 50 K, when all molecules are in the low state, as we will see in section 4.6

4.4 Saturation effects of current driven excitation in the checkerboard phase

In contrast to the up direction the down switching does not follow the ladder climbing model. Although that holds in both the checkerboard and the row phases, we will turn to the checkerboard phase, in which the size of the effect is larger.

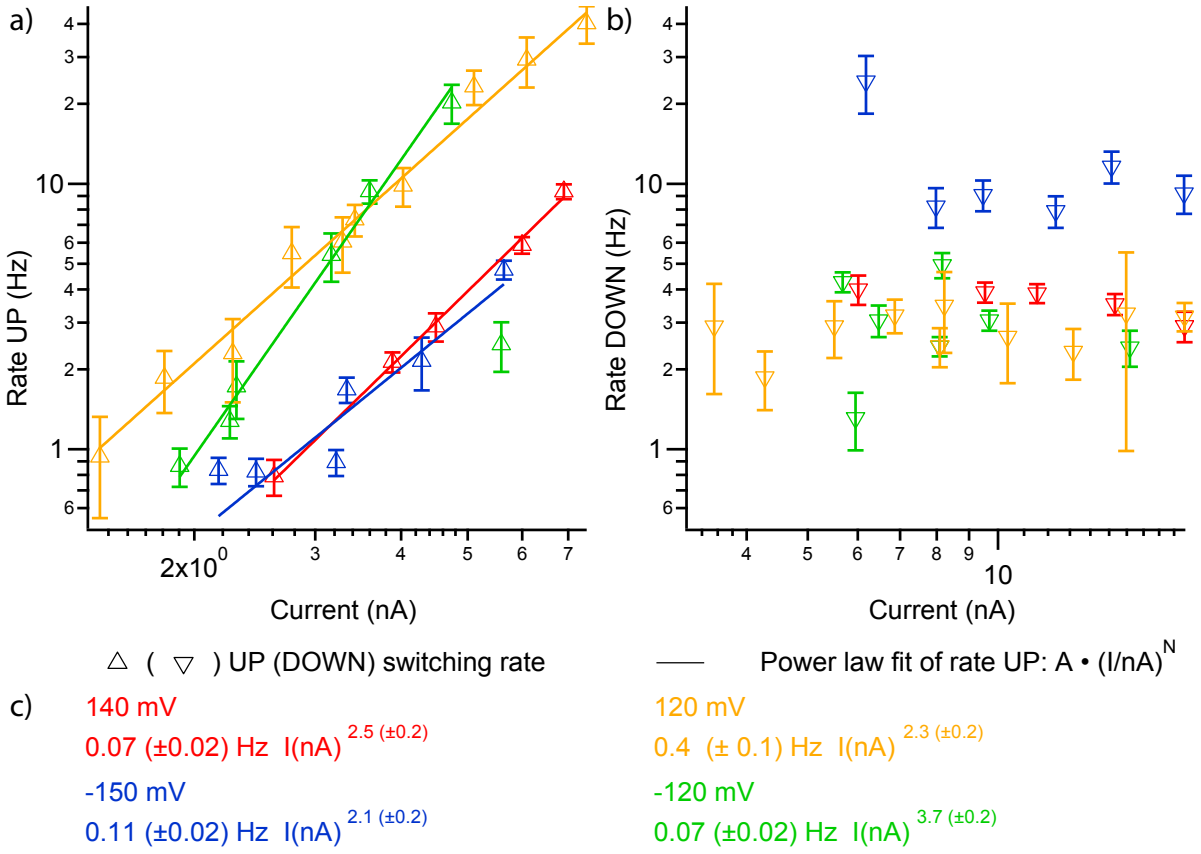

Figure 4.7: a),b)Rates into high/low state of different molecules in the checkerboard phase shown as up/down pointing triangles at different bias voltages. c) fit parameters of power law fit $y_0 + AI^N$.

As can be seen in Figure 4.7 a) the rates of switching into the high state lie on straight lines in the log-log plot and fit power laws with powers of about $N = 2$. Therefore the switching process into the high state in the checkerboard phase is governed by the same need for two electrons as the same direction at similar voltages in the row phase. Since for one voltage the data has been acquired on the same molecule but not all voltages were measured on the same molecule the absolute values of the rates can vary, while the power law behavior is the same.

The switching into the low state on the other hand behaves completely differently. In Figure 4.7 b) it can be seen that the rate for the down switching, at least in this range, does not depend on the current. For positive as well as negative values of bias voltage the rates are similar or at least of the same order of magnitude across one order of magnitude of tunneling current. While the exact threshold is not detectable with the setup, some tunneling current is needed to induce the switching. This is confirmed by retracting the tip by 10 Å (outside of the tunneling regime) above the measured molecule for a certain time with sufficient voltage applied and checking the STM images for changes in state. Since some tunneling current is needed to increase the rate from the baseline of some μHz, but above a certain value of current the rate stagnates, the underlying switching mechanism can be considered saturated.

What mechanism in addition to the current causes the switching into the low state in the saturated regime, is however, not obvious. Since the switching rate does not show a power law dependence on the tunneling current, the switching cannot be induced by electron excitations alone. Alternative stimuli that can induce conformational changes are the temperature and the electric field that can change the reaction landscape and assist a conformational change [95] or even induce it entirely [96]. The electric field component in the z-direction can be ruled out as the only driving force since the rates are similar at both polarities. Furthermore the size of the tunneling current at a given bias depends on the tip height above the sample which in turn determines the size of electric field. The rate being independent of the current also means that it does not depend on the electric field strength. At least in the voltage range of $\pm\{120...150\}$ mV the electric field either does not play a role or its effect saturates similarly to that of the tunneling current.

A similar behavior of the switching down is found in the row phase as can be seen in the power law fit of the rates in Figure 4.5. The clearly sublinear dependence of the switching down rate on the current can be seen as the onset of saturation.

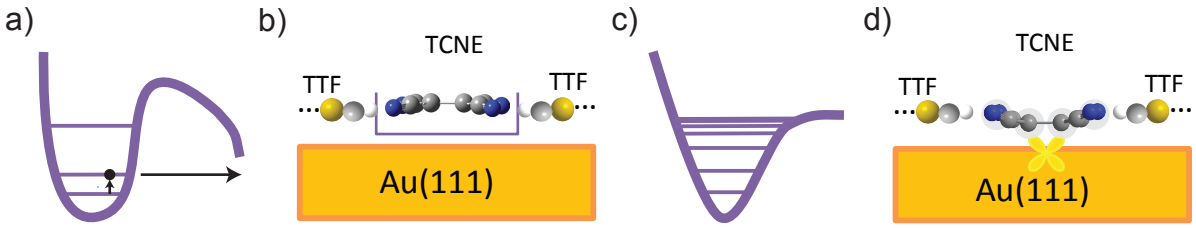

Figure 4.8: a) box-like potential - increasing energy spacing; b) TCNE in box-like potential created by steric interaction with TTF; c) shallow dissociation potential - decreasing energy spacing; d) attractive interaction due to hybridization of d-orbital of Au and the TCNE-LUMO dominate.

The saturation effect can be explained by considering that the switching in both directions probably requires the tunneling current, but also contains an additional step that is not influenced by the parameters of the junction and is significantly slower than the current induced step and therefore dominates the speed of the switching. After the system is excited in the first step to a certain intermediate level, the second step proceeds thermally induced or by tunneling [90]. A saturation would then occur and the rate of the second step would be indeed independent of the current if no further excitations by the current are possible from the intermediate level. The population of the intermediate level would reach an equilibrium between excitation, relaxation and deexcitation for some value of the electric current and the overall speed of reaction would stagnate for higher currents.

This scenario is difficult to imagine in the case of vibrational ladder climbing as the first step excitation, since higher lying vibrational levels are always available for excitation in a harmonic potential. Whether the second step is thermally induced or proceeds by tunneling, the barrier that has to be overcome is thinner from an energetically higher lying intermediate level and hence the rate of the second step process would be higher for a higher electrical current. This implies either a strong deviation from the harmonic shape of the reaction potential or a non-vibrational intermediate state.

A possible non-vibrational intermediate state might be the excitation of an electron into the singly occupied LUMO of the TCNE molecule that lies energetically close to the Fermi level and spatially convenient for an occupation by a tunneling current electron. However the excitation of the LUMO as the intermediate state in question would not explain the rather sharp onset of switching at $\pm 90\,\mathrm{mV}$. The apparent symmetry around the Fermi energy rather implies an inelastic excitation.

A gap in the vibrational spectrum can be explained by an anharmonicity in the vibrational potential along the reaction path of a suitable shape as illustrated in Figure 4.8 a). While the energy levels in a harmonic potential are equidistant, a more box-like potential can lead to level spacings that strongly increase with increasing level number. In this case the electron energy that is sufficient to excite the first level could be insufficient for the excitation of higher levels, leading to saturation of the excited level population and the saturation of the switching rate that depends on it. Interestingly, the overall switching rate would then be of the order of magnitude of the rate of the second step. As illustrated in Figure 4.8 b), it is the steric repulsive interaction with the neighboring molecules that facilitates the box-like potential.

In a typical adsorption potential that is illustrated in Figure 4.8 c) the anharmonicity is shallower than a harmonic potential, leading to a decreasing level spacing. This potential behaves like the truncated harmonic oscillator described in 4.2. In the low state the attractive interaction between TCNE and the surface switching up direction, on the other hand, is dominated by the attractive interaction of the TCNE molecule with the surface which is most likely caused by a hybridization of d-like states of the metal surface and the TCNE-LUMO.

In more general terms, the energetic potential of the reaction path is composed of a part that can be expressed as some combination of vibrational modes and the reaction barrier. If the reaction barrier is hindering the respective vibrations it induces a steep anharmonicity. In such an anharmonic potential, models that base on the truncated harmonic oscillator picture can fail in describing the dependence of the rate on the current.

Similar to the row phase the up switching rate increases considerably with increased bias voltage as can be seen in Figure 4.9 a). Given that vibrational modes are available for excitations in the shown energy range up to 270 mV the increase in rate is expected. The switching rate into the low state on the other hand is not dependent on the bias voltage as can be seen in Figure 4.9 b) at least for positive voltages. This suggests that possibly only few vibrational modes around 100 mV couple to the reaction path and only the excitation of these few modes causes switching. Alternatively, the same mechanism that reduces the increase in rate of switching into the low state at positive biases in the row phase can also be responsible here.

Contrary to the behavior at positive bias the down rate increases when increasing the electron energy at negative bias as shown in Figure 4.10. Although the absolute values are lower, the increase is similar to that of the direction into the high conducting state, suggesting a similar increase in the excited vibrational modes upon increase of electron energy. In particular around -270 mV an upward trend is visible by the naked eye for both switching directions.

Since the difference to the case of positive bias voltages, where the down switching rate stagnates, is the presence of molecular density of states at positive bias, the different behavior can be rationalized in terms of different tunneling pathways. At positive bias voltages the elastic tunneling through the molecular density of states dominates the tunneling process reducing the effective cross section of inelastic tunneling thereby reducing the switching rate that depends on inelastic excitations. This interpretation suggests that at positive, as well as negative, voltages that correspond to the energetically highest vibrational modes of TCNE the switching rates for both directions would show a power law dependence on the current, the data, however, is not available.

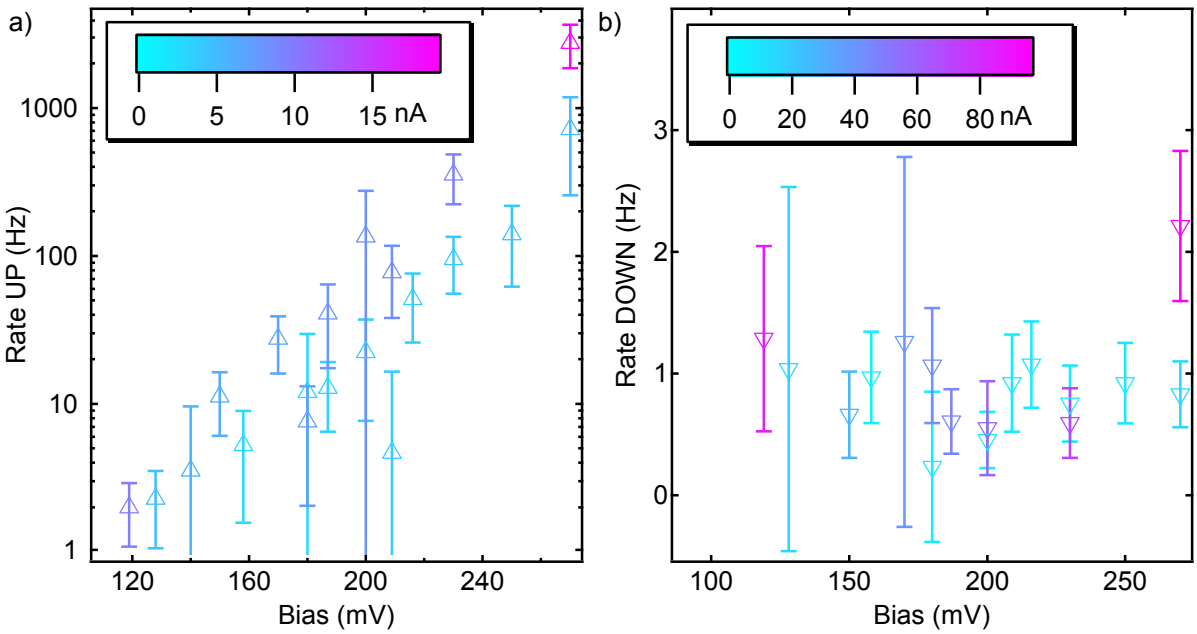

Figure 4.9: a)/b)Rates into high/low state of two molecules in the checkerboard phase shown as up/down pointing triangles at positive bias voltages. Color codes indicate current through molecule in original state.

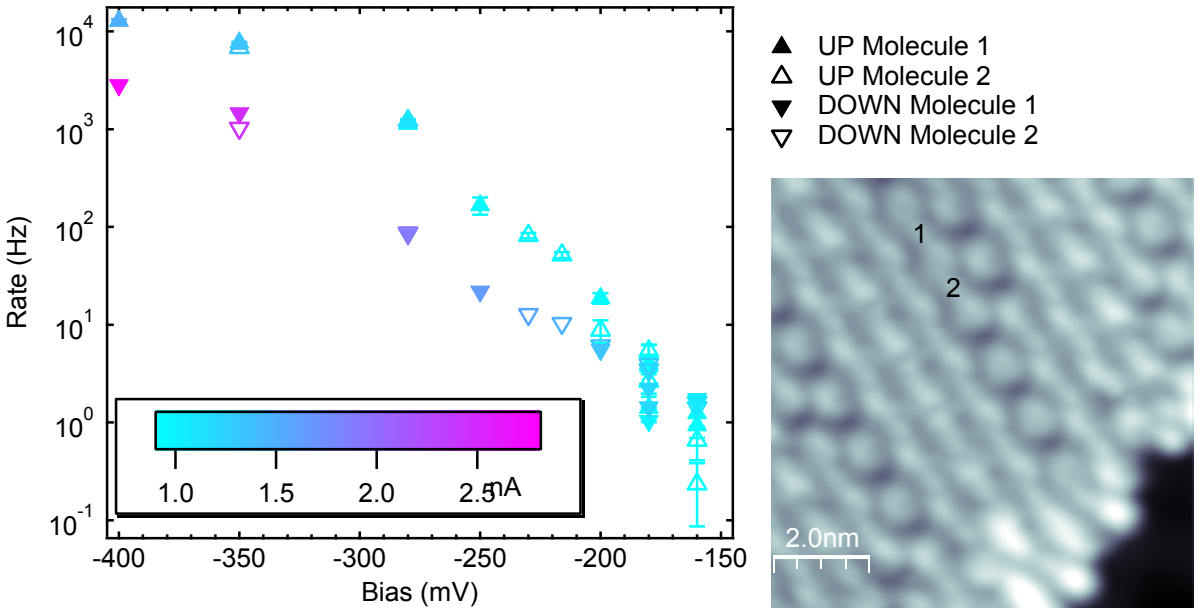

Figure 4.10: Rates into high/low state of two molecules in the checkerboard phase shown as up/down pointing triangles at negative bias voltages. Color codes indicate current through molecule in original state.

4.5 Effects of environment on switching

It is necessary to mention that not all current time traces recorded on the checkerboard phase show the clear characteristic of one single switching rate given for a specific current-voltage set point. Some traces are segmented into periods with rates that differ by orders of magnitude, which is even visible by eye in the raw data without the help of statistical evaluation. The segmentation is considerably rarer in the row phase. The definite explanation is unknown, however it could be attributed to structural changes in the island e.g. changes of TTF tilt that change the steric environment for the TCNE molecules and thus the energy landscape of the switching. While there are differences of switching behavior and TTF tilt in the checkerboard phase in different unit cells, all unit cells of the row phase are identical with respect to switching behavior and TTF tilt.

During statistical evaluation dwell time histograms of the current traces were fitted with two exponentials instead of one. The rate obtained from that with longer time integral is considered as the one mainly measured during the trace. Nevertheless outliers are still present in the shown data in particular in the row phase as shown in Figure 4.4, indicating a second stable configuration of the island with different switching landscapes

of the individual molecules. In the case of the row phase however the majority of the rate vs. current data points lies on the power law fit curve allowing to neglect the outliers for the fit. In the case of the checkerboard phase the data sets that were excluded from this work consist mostly of rate vs. current data points that could be fitted with the same functional dependences as that included, but have too many outliers to produce reasonable numerical fits.

4.6 Stability of conformational states and rates at higher temperature.

The previous discussion of the conformational change is easily visualized as the motion along a reaction coordinate in a double well potential. It was shown above that at least one of the wells has a depth of a certain order of magnitude ($\approx$ 200-300 mV). More information on the parameters of the potential e.g. if one of the conformational states is energetically lower than the other, would require the variation of more experimental parameters. As the equilibrium population density of the vibrational states changes with temperature [97] imaging the switching molecules at higher temperatures and comparing the stability regimes to lower temperatures can provide further insights.

In the previous discussion higher vibrational levels were assumed to be populated by the tunneling current. Since the lowest lying vibrational modes ($\approx$ 10 mV) are energetically well above k_BT at $T = 4\ K$ ($\approx$ 0.4 mV) the system lies in the vibrational ground state. The situation is different at $T = 50\ K$ ($\approx$ 4 mV) when the thermal energy is in the same order of magnitude as some vibrational modes. The population density of an excitation is the sizable Boltzmann factor $e^{-\frac{E_1}{k_BT}} \approx \frac{1}{10}$, where E_1 is the 1st excitation energy of the energetically lowest lying mode.

STM images at different bias voltages were recorded at $T = 50\ K$ as seen in Figure 4.11 and show different stability behavior of TCNE molecules at different voltages. Let us compare this stability behavior with the one at $T = 4\ K$ that was discussed previously.

The fairly simple bistability behavior of the low temperature regime is contrasted by the higher diversity at the higher temperature. In Figure 4.11 constant-current STM images of a TCNE-TTF island taken at 50 K at different bias voltages 400 mV, 700 mV, 90 mV, -300 mV are presented. Similar to the low temperature case, rows with similar

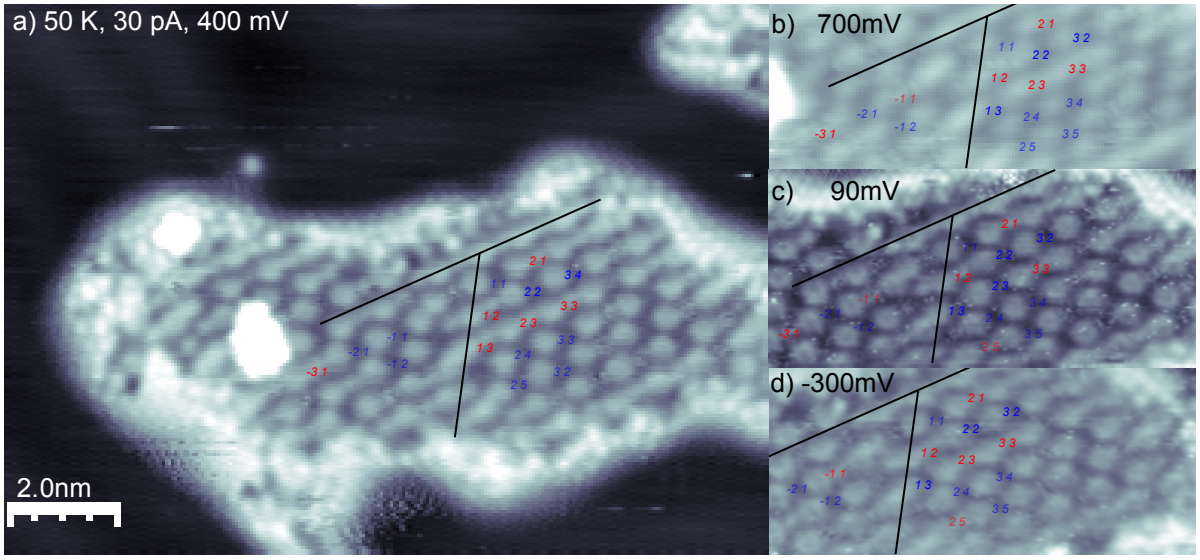

Figure 4.11: Constant-current STM images at 30 pA of a TCNE-TTF island at different bias voltages: 400 mV, 700 mV, 90 mV, -300 mV a)-d) respectively. Several TCNE molecules marked with numbers of red(blue) color if they appear rather high(low) in the respective image. Several molecules appear flickering throughout the series.

stability within them alternate in the island. Rows of always stably high appearing TCNE molecules are present. The most striking difference is the presence of molecules that appear in the low state independently of the bias, whereas in the low temperature case all TCNE molecules appear high at positive voltages above ≈200 mV. The second difference is the presence of flickering molecules below 100 mV and above ≈200 mV. A minor difference are TCNE molecules that flicker and appear rather high or low depending on the voltage.

Molecules that appear in only one state (here high) regardless of temperature and electronic stimuli are clearly predominantly in their thermodynamically stable state. The energy well of the low state is for these molecules either too shallow or absent. Analogously the low only molecules are in their thermodynamically stable state while for the flickering molecules both states have the same energy. From this follows that the relative energetic position of the two conformations changes along the molecular island. The energy well of the high state however is available for every TCNE molecule.

Not only vibrational modes of the free molecule are populated by temperature but also center of mass motions of the molecules in the steric potential created by their neighbors. At this elevated temperature the molecules see an effectively denser island around them

and all steric effects are amplified. This can contribute to the pronounced stability of the low state. It is however unlikely to change the trend in stability e.g. make a less stable state to the more stable one.

It is worth to mention that the vibrational modes populated by the temperature need not be the same as the modes populated by the electric current. The tunneling electrons deposit energy in the particular mode through inelastic excitations only if the cross-section of the respective excitation is non-zero. On the other hand, all modes can be considered equally well populated thermally because the molecule is well coupled to the substrate that acts as thermal bath.

4.7 Controlled switching

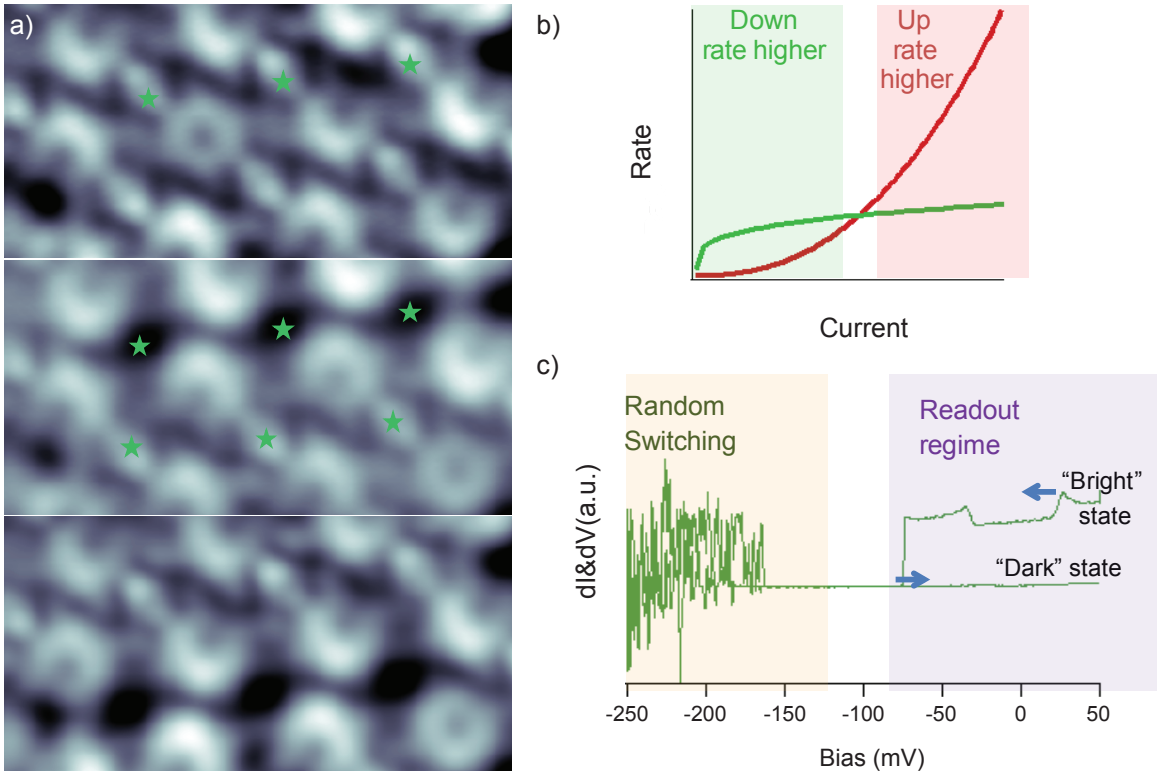

Figure 4.12: a) Three images of the same six molecules. Manipulations marked by green stars. b) Rates of switching up (red) and down (green) vs. tunneling current. c) bias voltage is ramped to the instable regime and back with selected switching preference.

As we have seen in section 4.4 the two switching directions behave very differently under

the variation of the electric circuit parameters bias and voltage. This opens the possibility for the application as memory device for which the control procedure will be described in the following.

As is illustrated in Figure 4.12 a) a set of six molecules that can be viewed as a molecular digital memory array of six bits. Here it is set into the example configurations all six molecules in the high state, three molecules in the down state and three in the up state, all states reversed to the previous configuration corresponding "111111", "000111","111000" respectively. The system shows no fatigue after millions of single switching events, meaning that the switching can be performed an unlimited number of times. The principle that is exploited to increase the probability of the desired outcome of the random switching event is shown in Figure 4.12 b). A current can be chosen by setting the height of the STM tip above the surface such that the rate of switching into the high state or the rate into down state is dramatically higher than that of the reverse process. The bias voltage is then ramped out of the stable regime into the regime of random switching and back into the stable regime as can be seen in Figure 4.12 c). With the tip height set for the desired high or low state, the molecule is likely but not guaranteed to end in this state at the end of the ramp. If the molecule does not switch into the desired state the procedure can be repeated.

4.8 Summary

The TTF/TCNE on Au(111) charge transfer complex adsorbs in at least two ordered phases with similar electronic and conformational structure of the TCNE molecules. While the atomic configuration of the phase discussed in chapter 3 is known very well, the second phase offers higher stability at elevated voltages, which allows more thorough investigation of the switching rates. For the discussion of the switching phenomena in the charge transfer complex the results of the two phases can be combined.

Utilizing the ladder climbing model, the number of inelastic excitations via tunneling electrons needed to facilitate the switching from the bent conformational state into the flat state is determined. Comparing different numbers of electrons at different bias voltages, the reaction barrier height can be estimated. From the fact that one excitation suffices to switch the TCNE at electron energies around 230 mV, but two are needed at

energies between 110 mV 150 mV that excite C-C stretch vibrations, an effective barrier height in the order of magnitude of 200 mV is estimated.

While this barrier height seems to be higher than the thermal energy at room temperature, already at a moderately elevated temperature of 50 K only the bent state can be observed. This implies an asymmetric energy landscape with the bent state as the thermodynamically stable state.

The switching from the flat state is suppressed at positive bias voltages. This is possibly due to a reduction of the cross section of vibrational excitations by an alternative elastic tunneling path through an elevated density of electronic states in the flat conformation at positive bias voltages.

The route to controlled switching into the desired state is opened up by the qualitatively different behavior of the switching rates. Possibly due to a gap in the vibrational excitation spectrum facilitated by repulsive interaction with neighboring molecules the switching rate shows a less than linear dependence on the tunneling current. This speaks for a two-step process with a current independent, likely thermally induced second step. The asymmetry of the switching behavior can be exploited to find parameters of voltage and current which favor the switching rate into one state or the other, allowing controlled probabilistic switching.

5 Magnetic anisotropy in a single-ion lanthanide complex on the surface

The magnetic moment is well established as a degree of freedom in computing and memory storage [98, 99]. As single magnets that represent one bit of information approach the molecular scale, not only does the amount of potentially stored information increase, but also new methods of quantum computation become available [100, 98]. Among other practical concerns the magnetic moment needs to be stabilized [101]. In magnets composed of hundreds of atoms and even in single-molecule magnets (SMM) with several metal ions, this stabilization is mainly facilitated by exchange coupling [102, 103, 104, 105, 106, 107]. The even more important factor in the definition of the magnetic moment as memory unit is the magnetic anisotropy, preferably along the direction of a single axis. This is true for all sizes of magnets but is especially important for single-ion complexes [108, 109, 110, 111]. Here, the anisotropy is also responsible for the stabilization of the moment, since exchange coupling is not necessarily available.

The transition between states of different magnetic moment is facilitated by thermal excitations. By increasing the energy barrier between the two ground states with opposite magnetic moment and the excited states and by reducing the admixing between the relevant states, the so-called anisotropy barrier is formed. Avoiding the admixing of states with opposite magnetic moment is important in order to reduce the effect of tunneling of magnetization. As explained in section 2.4.2, the magnetic anisotropy of the 4f rare earth ions is the result of the interaction between the ligand- or crystal-field and the orbital angular momentum of the ion. Due to the strong spin-orbit coupling, at least in the Hund's rules ground state, the spin of the 4f-shell is strictly parallel or strictly anti-parallel (depending on the number of electrons) to the orbital angular momentum for all realistic magnetic fields. The resulting large total angular momentum and hence, a large magnetic moment in the second half of the lanthanide row, makes elements like terbium, dysprosium or holmium interesting for magnetic applications.

In some SMMs a big anisotropy barrier is achieved in an environment of pronounced symmetry, as for example in terbium and dysprosium double-decker molecules $TbPc_2$ and $DyPc_2$ [112]. There, the metal ion is embedded in an four-fold cylindrical symmetry between two phthalocyanine molecules. The configuration then strongly favors ground states with oblate shaped density distribution of the 4f-orbital, which are also the states with the highest magnetic moment. Another approach involves dysprosium and ligand fields with a low symmetry [57]. The low symmetry also favors the oblate shaped density distribution and thereby induces a uniaxial anisotropy with a high anisotropy barrier and a high magnetic moment.

In addition to a stable magnetic moment an electric readout mechanism would be convenient. Such a readout mechanism was accomplished for the above mentioned terbium double-decker SMM [113]. When placed between the two leads of a gated electric transport device, the magnetic state of the 4f-shell and even the nuclear spin state could be detected.

Within this work a combination of the two approaches is investigated. When an organic molecule with a dysprosium (Dy) center is adsorbed on a metal surface, its symmetry is lowered. As a consequence a pronounced uniaxial anisotropy arises. At the same time, the molecule is contacted by an electric lead which could potentially serve as an electric readout. Although an electric readout has not been realized for the molecular complex studied in this work, the presented approach is advantageous because of its simplicity and universality. It promises a high potential for various chemical agents that can perform as hosts for the information carrying magnetic moment.

In the following, the results of a combined STM and XA spectroscopy study of the complex dysprosium-tris(1,1,1-trifluoro-4-(2-thienyl)-2,4-butanedionate) ($Dy(tta)_3$) are presented. The complex was synthesized by Prof. Dr. Constantin Czekelius. The X-ray absorption (XA) measurements were performed by Dr. Matthias Bernien in the research group of Prof. Dr. Wolfgang Kuch.

In order to get insights in the effect of adsorption of the complex on the 4f-shell of the central metal ion, XA spectroscopy has been performed at the high-field diffractometer of the beamline UE46-PGM1 at BESSY II, using p- or circularly polarized X-rays. The absorption of linearly polarized light is sensitive to the orientation and filling of the 4f-shell while circularly polarized X-rays are sensitive to the orientation and size of

magnetic moment that originates from it. The XA spectra are simulated using multiplet theory implemented in the code of Cowan [63]. The exact anisotropy of $Dy(tta)_3$ on Au(111) is deduced from the dependence of the magnetization on the magnetic field strength and orientation. To obtain the magnetization the X-ray Magnetic Circular Dichroism (XMCD) signal is recorded. This signal is proportional to the magnetization up to the magnetic dipole term T_z that is included in the multiplet simulation of the XA spectra.

From the angle and field-dependent magnetization data, the size of the anisotropy barrier can be approximated. Since the data is taken at one temperature only, the lower energy level differences are known quite well, while the higher are unknown. Dynamic measurements would be able to determine the total barrier, but are, as of now, not available for sub-monolayers.

The following chapter follows closely the paper of Bernien and Stoll [114]. All STM experiments and interpretation thereof has been done in the AG Franke by Paul Stoll. All XAS experiments and simulations of the spectra as well as the interpretation thereof has been done by Dr. Matthias Bernien in the AG Kuch. The determination of the anisotropy parameters from the magnetization curves has been redone for the purpose of consistent figure style and is in agreement with the values presented in the paper [114].

5.1 Experimental details

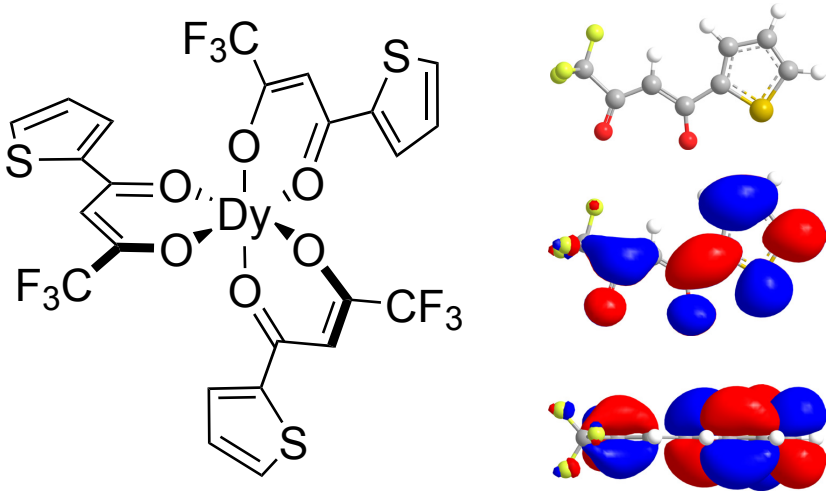

Figure 5.1: Left: Structure of $Dy(tta)_3$ [114]. Right: tta ligand (top), 6-31+g* [115, 116, 117, 118] calculated LUMO sideview (center), LUMO top view (bottom).

The $Dy(tta)_3(H_2O)_2$ complex with the structure shown in Figure 5.1 was prepared in the group of Prof. Dr. Czekelius as the dihydrate $Dy(tta)_3(H_2O)_2$ according to well known synthesis methods [119, 120]. The evaporation of the dihydrate was studied by mass spectrometry in the group of Prof. Dr. Czekelius to establish that the water ligands are cleaved off well below the evaporation temperature of 463 K [114]. Also, no fragments of hydrolysis are detected. These studies show that $Dy(tta)_3$ can be evaporated without decomposition.

These molecules were evaporated from a Knudsen cell at 470 K onto an atomically clean Au(111) surface held at room temperature in ultrahigh vacuum. The sample was then annealed to 385 K to allow for self-assembly on the surface.

The prepared sample was cooled down and transferred under ultrahigh vacuum conditions into a custom-made scanning tunneling microscope (STM) with a working temperature of 4.8 K. All STM images were recorded in constant-current mode with a Au-coated tungsten tip. Differential conductance spectra were acquired with fixed tip-sample distance or activated feedback loop as indicated in the respective figure captions, using a lock-in amplifier.

X-ray absorption (XA) spectra were measured at the highfield diffractometer of the beamline UE46-PGM1 at BESSY II, using *p*-polarized or circularly polarized X-rays. No

spectral changes at the O-K, Dy-$M_{4,5}$ edges have been observed on the time scale of the experiment. Furthermore, no changes of the magnetic response were observed. Thus, X-ray-induced degradation (beam damage) of the molecules can be excluded. The XA signal was recorded in total electron yield mode measuring the drain current of the sample as a function of photon energy. For the X-ray magnetic circular dichroism (XMCD) measurements, an external magnetic field was applied parallel to the photon propagation direction. All X-ray natural linear dichroism (XNLD) spectra were measured in a small magnetic field of 20 mT applied parallel to the k vector of the X-rays, to ensure efficient extraction of the secondary electrons at a temperature of 4.5 K. All XA measurements were performed at the same surface coverage of 0.2 ML.

5.2 Molecular configuration on the Au(111) surface

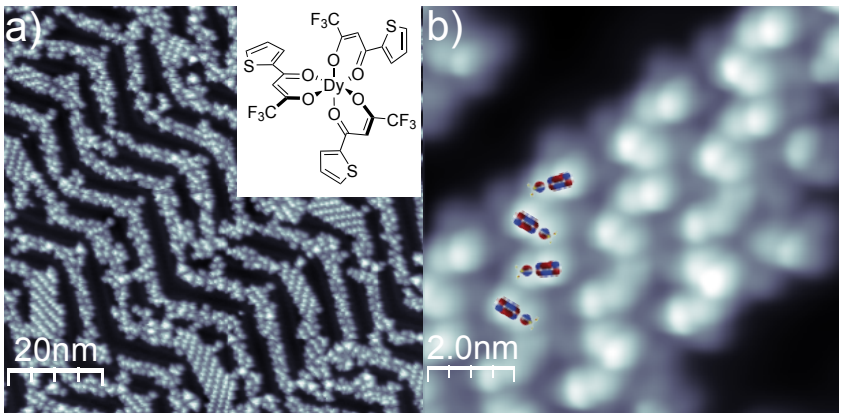

Figure 5.2: (a) STM image of the $Dy(tta)_3$ complex on Au(111). The islands of densely packed $Dy(tta)_3$ complexes align along the herringbone reconstruction ($V = 0.5\,V$, $I = 75\,pA$). Inset: Chemical structure of$Dy(tta)_3$. (b) Close-up STM image of the molecular islands. A regular zigzag alignment of the molecules within these islands can be observed. A smaller and larger lobe separated by a nodal plane can be identified ($V = 0.3\,V$, $I = 50\,pA$).

The structure of $Dy(tta)_3$ as shown in the left part of Figure 5.1 promises a strong adsorption onto the gold surface due to the thienyl terminations at the three organic ligands of the complex. Due to the three-dimensional geometry, however, only two of the three ligands should be able to adsorb onto the surface. Along with this ideal scenario, decomposition of the complex is also thinkable. When studying magnetic properties with XAS, a result that is averaged over a macroscopic number of molecules is obtained. It

can be verified by STM that the adsorption configuration is identical for all molecules on the surface.

Upon deposition the $Dy(tta)_3$ molecules accumulate along the herringbone reconstruction of the Au(111) surface as can be seen in Figure 5.2. At surface coverages close to a full monolayer the restricted area for adsorption forces densely packed molecular arrangements, which align along the herringbone reconstruction. A closeup view of the STM images reveals features of uniform appearance. Figure 5.2 b) shows that each unit consists of two bright oval-shaped protrusions with slightly different apparent height and background protrusions, which are less well defined. The size of these units matches well with the molecular size and their uniformity reveals that the molecules are intact on the surface. Comparison of the LUMO shape of the singly charged tta ligand (superimposed on the STM image) with the oval protrusions suggests that one tta moiety is standing upright with respect to the surface. The other two ligands are seen as the lower protrusions in the STM images, partially located underneath the upper ligand as sketched in the inset of Figure 5.3.

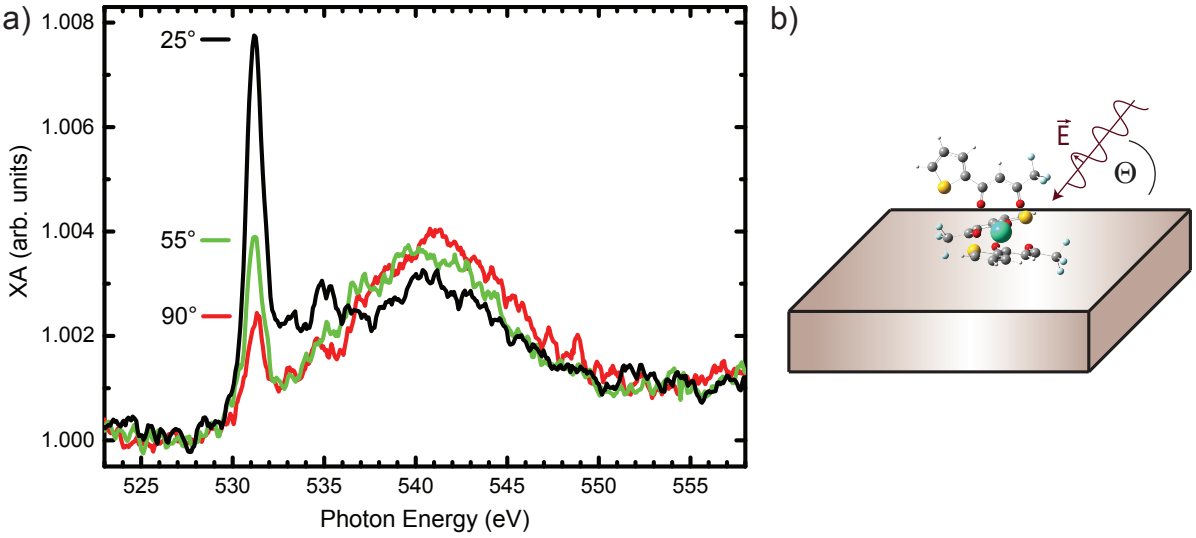

Figure 5.3: a) X-ray absorption spectra of the O K edge of 0.2 ML $Dy(tta)_3$ on Au(111), recorded with angles of 25°, 55°, and 90° between the polarization vector of the linearly polarized X-rays and the surface normal. b) Sketch of the adsorption geometry with direction of X-ray beam and *E*-field vector.

This adsorption scenario leads to the assumption that the complex changes coordination geometry upon binding to the surface. A more reliable determination of the orientation

of the ligands on the surface can be obtained by near-edge X-ray absorption fine structure (NEXAFS) that has been discussed in detail in chapter 2.5. Figure 5.3 a) shows angle-dependent spectra taken at the oxygen K edge, which represent transitions from the O 1s core levels to unoccupied molecular states. All spectra exhibit a pronounced π^* resonance at 531.2 eV photon energy with its intensity being highest when the incidence angle of the X-rays is strongly grazing. This situation corresponds to the polarization vector of the exciting X-rays being closest to the surface normal demonstrated in Figure 5.3 b). Therefore, the π electronic systems around the oxygen atoms, and thus the C–O bonds, must on average exhibit an orientation more parallel to the surface. Assuming random azimuthal orientations of the molecules as also seen in STM images, the NEXAFS spectra are quantitatively evaluated as described in detail in section 2.5.1. The measured angle dependence matches a scenario in which two of the ligands are fully parallel to the surface, while the third one is standing upright with its plane parallel to the surface normal, consistent with the STM results.

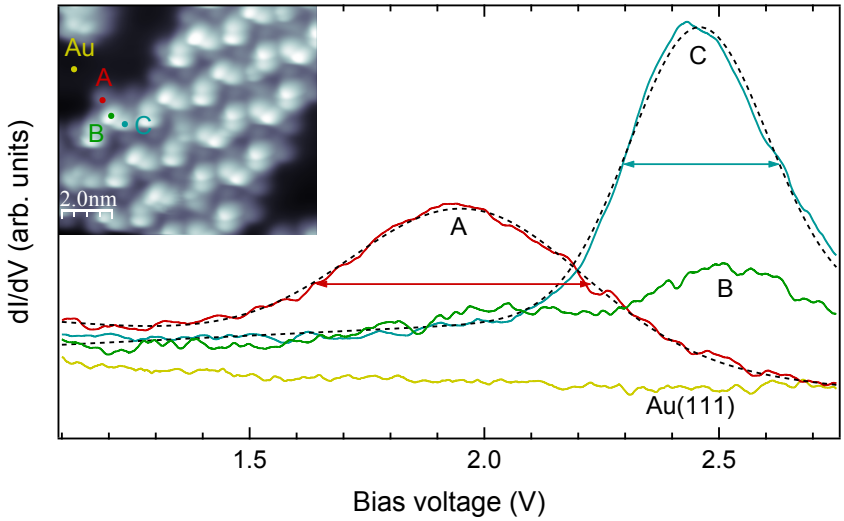

Figure 5.4: Differential conductance spectra recorded in constant-current mode at different sites of the $Dy(tta)_3$ molecules as color-coded onto the STM image ($V_{mod} = 5\,mV$, $I = 100\,pA$ for A, C; $V_{mod} = 15\,mV$, $I = 59\,pA$ for B). The spectrum recorded on the lower ligand (A, red) shows a broad resonance at 1860 meV, the one at the edge of the upper ligand (C, blue) shows a sharper resonance shifted to higher energy (2460 meV). The spectrum at the center (B, green) of the molecule shows a double-peak structure due to both contributions. Red and blue arrows indicate the full width at half maximum (FWHM) of the fitted Gaussian lineshapes (dashed lines). The reference spectrum on Au (yellow) is flat.

The geometry of the adsorbed molecules is also reflected in the electronic structure of

the organic ligands as measured by scanning tunneling spectroscopy. In Figure 5.4 the differential conductance spectra (dI/dV) with submolecular resolution are presented. Spectra taken on the upper ligands (location C) exhibit a resonance at 2460 meV with a full width at half maximum (FWHM) of 350 meV. Spectra on the lower ligand (location A) show a peak that is energetically down-shifted by about 500 meV and significantly broader (FWHM = 580 meV). This behavior evidences a stronger hybridization with the substrate, leading to energy-level broadening and downshifting of the resonance due to stronger screening of the tunneling electrons [37]. When tunneling through both types of ligands, i.e., through the center of the molecule (location B), both peaks can be detected simultaneously. Hence, the spatially resolved spectra corroborate the picture of one upright-oriented ligand, which is hardly affected by the underlying substrate, and two ligands, which are almost flat on the gold surface.

5.3 Magnetic anisotropy of Dy(tta)$_3$

The flat adsorption geometry of the two negatively charged β-diketone groups implies a coordination towards the central ion from opposite directions. The predominant ligand field distorts the 4f-shell charge cloud from spherical symmetry. This on the one hand, lifts the degeneracy of the projection J_z of the total orbital angular momentum $\vec{J}$, the M-quantum number, resulting in an anisotropy of the magnetization. On the other hand, the XA spectroscopy will differ for different angles between the polarization vector $\vec{E}$ of the X-rays and the quantization axis of the ion as well as for different polarization of the X-rays.

5.3.1 Orientation of Dy(tta)$_3$ 4f orbitals

To determine the preferred direction of the magnetization, XA measurements with linearly polarized X-rays have been carried out and compared to simulated spectra. Figure 5.5 shows XA spectra recorded at different X-ray incident angles. The peaks correspond to transitions from the filled 3d shell to the open 4f shell with the lower energy part deriving from the $3d_{5/2}$ and the higher energy transitions deriving from the $3d_{3/2}$ states, respectively. The characteristic triplet structure at the M_5 edge stems from transitions with $J = 0, \pm 1$ as has been described in detail in section 2.5.2. It is known from the

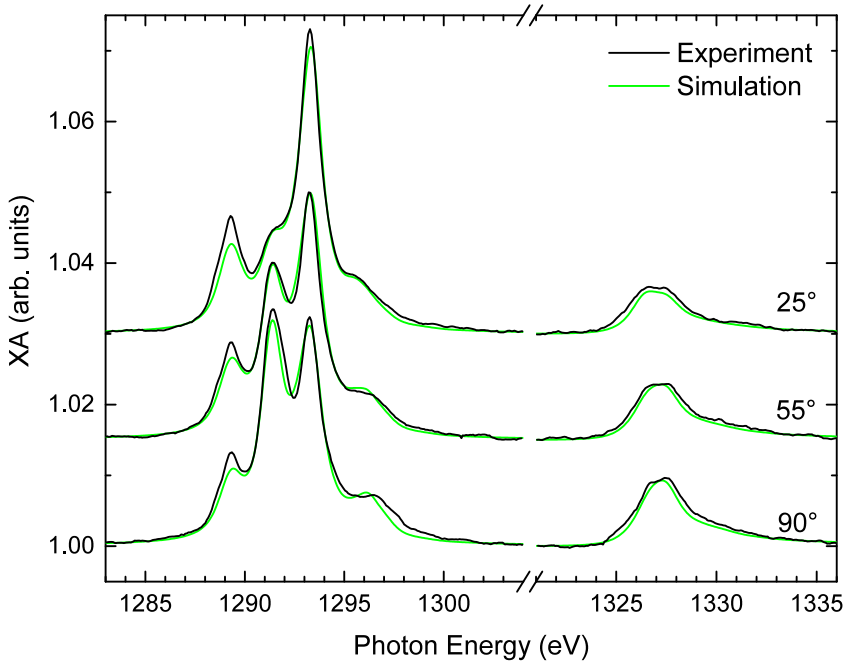

Figure 5.5: XA spectra (black lines) of 0.2 ML $Dy(tta)_3$ on Au(111), recorded at the Dy-$M_{4,5}$ edges with angles of 25°, 55°, and 90° between the E vector of the X-rays and the surface normal at a temperature of 4.5 K. Green lines are simulated spectra obtained from multiplet calculations. The spectra are offset for clarity.

work of Goedkoop and Thole [61] that for linearly polarized light the intensity of the $J = 0$ peak increases with the square of the magnetization, while the intensities of the $J = \pm 1$ peaks decrease. Hence, the low intensity of the middle peak of the M_5 edge for 25° between the E vector and the surface normal compared to a high intensity of the peak for the E being parallel to the surface evidences a predominant magnetization direction in the surface plane.

The line shape for the magic angle of 55° agrees with that of a calculation of a 3+ oxidation state [61], as expected for the molecule with three monovalent tta-ligands. In addition, the agreement of the measured line shape with a calculated line shape of a free ion evidences an unperturbed character of the measured 4f-shell of the Dy atoms.

Not only the preferred orientation of magnetization in absence of a magnetic field can be inferred from XA spectroscopy, but also the magnetization in a magnetic field, which is important for deducing the size and the orientation of the magnetic anisotropy. As explained in 2.5.3, XMCD signals are the difference between two spectra recorded with opposite helicities of circularly polarized X-rays and are proportional to the magnetization projected onto the k-vector of the X-rays [61, 121]. In Figure 5.6 Dy $M_{4,5}$ XA spectra for circularly polarized X-rays and the corresponding XMCD difference curves taken in a magnetic field of 6 T and a temperature of 4.5 K are presented. The XMCD signal

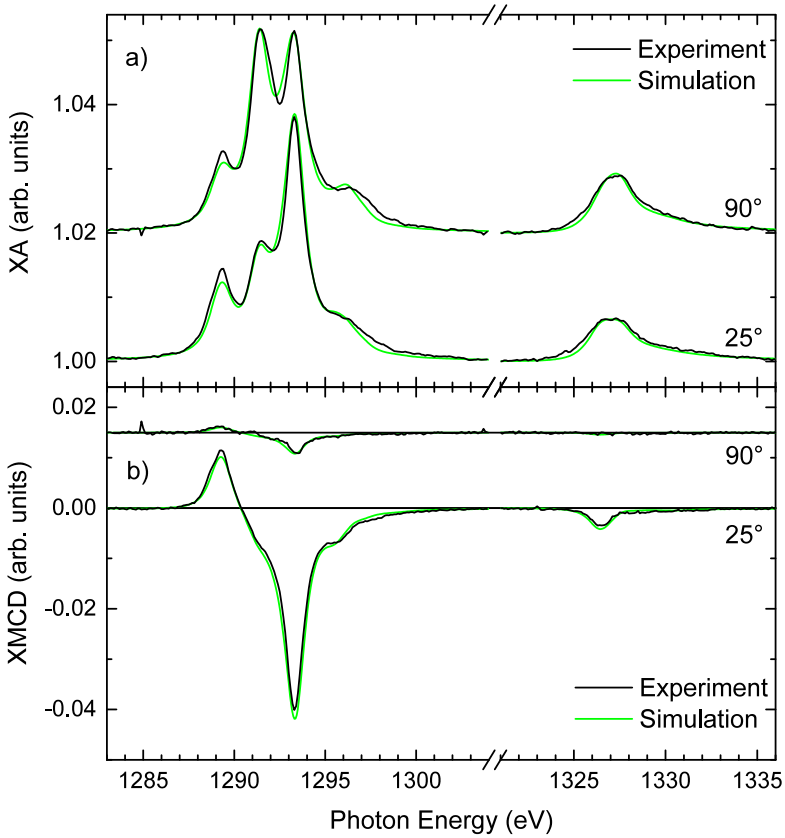

Figure 5.6: a) Dy-$M_{4,5}$ XA spectra (black lines) recorded under 90° and 25° incidence angles in an applied magnetic field of 6 T parallel to the k vector of the circularly polarized X-rays at a temperature of 4.5 K; the spectra are offset for clarity; b) the XMCD signal reflects a sizable magnetic moment of the Dy core for 25° incidence; green lines are simulated spectra obtained from multiplet calculations.

at 25° grazing incidence is 8.7 times higher compared to the one in the perpendicular direction. The strong angle dependence of the XMCD signal further hints at a large magnetic anisotropy due to the distinct ligand field.

To quantify this magnetic anisotropy we recorded the XMCD signal as a function of the magnitude and the direction of the external magnetic field. The integrated Dy-M_5-XMCD signal at 35° and 90° incidence angles is shown in Figure 5.7 a). The magnetization curve at 35° shows a steep increase and seems to saturate already at about 2 T. The XMCD signal in the vertical direction is very small and does not reach saturation up to 6 T. The integrated Dy-M_5-XMCD as a function of angle between the magnetic field and the surface is shown in Figure 5.7 b) for B = 6 T and T = 4.5 K. The XMCD is maximum at grazing directions and minimum when the magnetic field is applied normal to the surface.

The magnetization can be modeled as the magnetization of the 4f-shell in the applied magnetic field. Unlike in lanthanide bis(phthalocyaninato) complexes, where an unpaired electron is delocalized on the phthalocyanine ligands [122], each of the three tta ligands

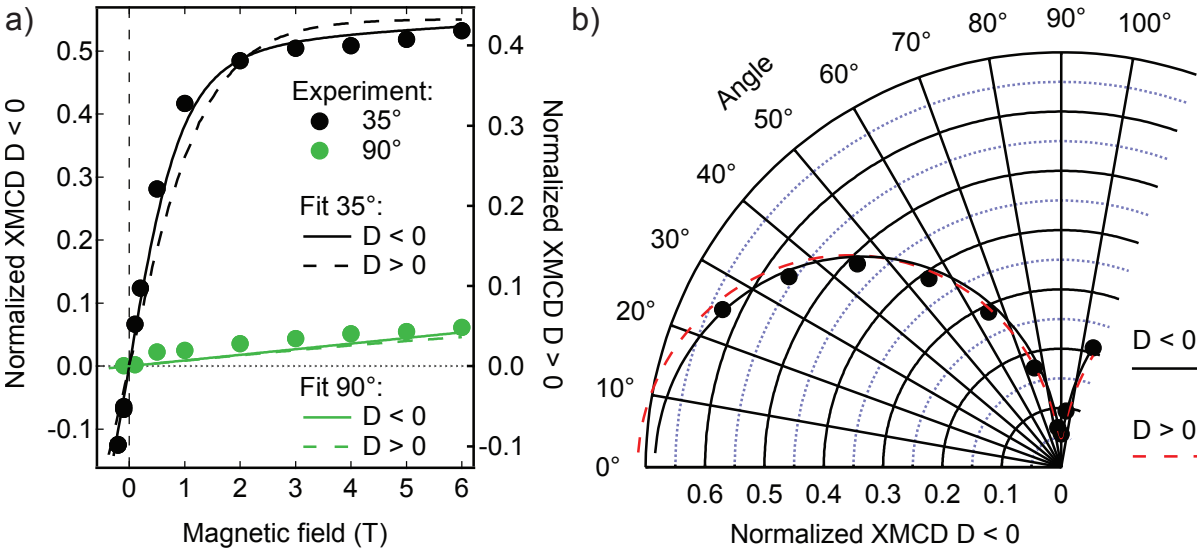

Figure 5.7: a) Magnetic field dependence of the integrated Dy-M_5 XMCD signal at 35° and 90° incidence angles; fit for $D < 0$ depicted by solid lines, for $D > 0$ by dashed lines; the XMCD signal is normalized to its saturated value on the left vertical axis for $D < 0$ and on the right axis for $D > 0$; b) angle dependence of the integrated Dy-M5 XMCD in an applied magnetic field of 6 T. All measurements were carried out at a temperature of 4.5 K with magnetic field and X-ray beam along the indicated angles.

in the free $Dy(tta)_3$ complex is singly negatively charged but has an even number of electrons. Since the Dy ion and the ligands are in their stable oxidation states a scenario in which additional unpaired spins on the ligands are created upon adsorption onto Au(111) is highly unlikely. Due to the shielded nature of the 4f electrons, the angular momentum L is not expected to be quenched by the ligand field. Due to its large size the spin-orbit coupling is easily treated in the Russel-Saunders (LS) scheme with the lowest multiplet given by Hund's rules as J = 15/2 for the nine 4f electrons of a Dy^{3+} ion [123].

A simple model Hamiltonian with a Zeeman term and a zero-field splitting parameter D acting on the spin-orbit coupled states $|JM\rangle$ can be used to describe the magnetization curves:

$$H = \mu_B g_J \vec{B} \cdot \vec{J} + D J_z^2, \tag{5.1}$$

with μ_B being the Bohr magneton and $g_J = 4/3$ the Landé g factor. Although the direction of the z-axis in the Hamiltonian is not known a priori, the strong preference of the magnetization to point parallel to the surface plane hints at two options. Either,

the z-axis lies in the surface plane and the zero field splitting parameter D is negative, favoring high M values. Since the molecules are randomly oriented along the azimuth, the observed magnetization is an average of a random distribution of this easy axis of anisotropy. Alternatively, the z-axis lies perpendicular to the surface plane and D is positive, disfavoring a magnetization perpendicular to the surface. The magnetic moment is then mostly precessing around the hard z-axis.

The fit curves in Figure 5.7 are obtained by diagonalizing 5.1 for each value of $\vec{B}$ and calculating the Boltzman-weighted average of the expectation value of the magnetization in the direction of $\vec{B}$ averaged over different azimuthal angles to account for the random azimuthal orientations of the Dy ions. Since the XMCD gives the magnetization only up to a proportionality factor, the axes are normalized to the saturation values that are obtained from the respective fit. While the easy-axis curve ($D < 0$) clearly matches the experimental data, the hard-axis curve ($D > 0$) fails to capture the steep increase of magnetization at small magnetic fields and saturates to a constant value rather than to follow the slow increase after 2 T. The hard axis fit fails to converge giving a high positive D value.

Using the information on the ligand field, the XA spectra can be simulated as is visible by the green lines in the figures 5.5 and 5.6. The spectra have been simulated and fitted to the experimental data using multiplet theory [61, 63]. The spectra are simulated using Cowan's code [63] as implemented in [124]. The details of the calculations are described in the Appendix of [114]. To calculate the field-dependent integrated XMCD, all allowed X-ray-induced transitions are summed over the thermally populated eigenstates of the Hamiltonian. Averaging over different azimuthal incidence directions and orientations of the magnetic field is carried out to account for the random azimuthal orientations of the Dy ions.

Combining the simulation of the XA spectra and the insight about the easy axis of anisotropy, the orientation of this axis can be determined from the linearly polarized XA data. Figure 5.8 shows the difference spectrum between spectra measured with 25° and 90° incidence angle already shown in Figure 5.5 and compares it to simulated spectra for three different orientations of the symmetry axis of the orbitals with respect to the surface. According to the simulations, the largest difference spectrum is produced by an orientation of the anisotropy axis of the metal ion in the surface plane. Since the experimental spectrum is very close to this situation and rather exceeds it, the easy axis

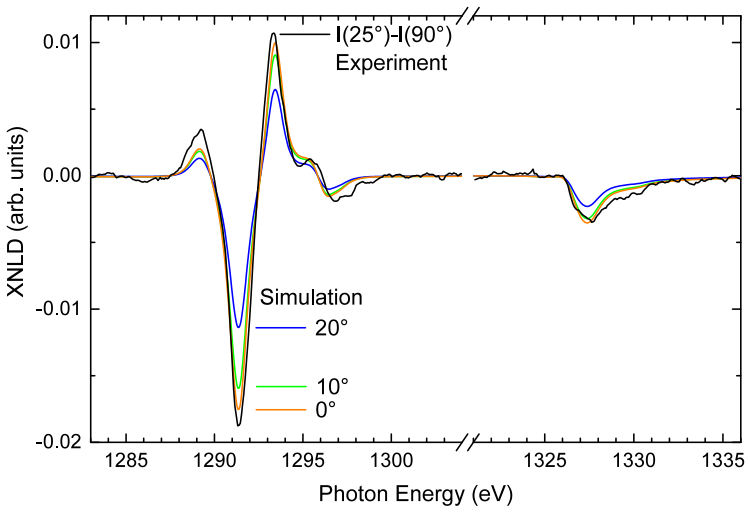

Figure 5.8: Dy $M_{4,5}$ XNLD difference spectrum between the first (25°) and the last (90°) spectrum from Figure 5.5. This spectrum is compared to simulated difference spectra for three tilting angles of the anisotropy axis with respect to the surface.

of anisotropy lies certainly parallel to the surface.

From the combined fit of the magnetization and all of the simulated XA spectra with D as the fitting parameter a value of $D = -0.68(15)\,\mathrm{mV}$ is obtained.

5.3.2 The ground state as confirmation of the uniaxial model

Strictly speaking, the Hamiltonian 5.1 of the system might also contain the parameter E as the energetic difference between the x and y directions of the total orbital angular momentum as well as some higher order field parameters. Indeed, some small value of E cannot be excluded and has to be assumed due to the low symmetry of the ligand field. Its main effect is the mixing of states with different projection of the total angular momentum onto the z-axis. However, due to the azimuthal averaging of magnetization it is difficult to determine the size of the parameter or the orientation of the corresponding x axis. When included in the fit routine, the main effect of a non-zero E on the fit curve is a better match at higher magnetic fields at the cost of a worse match at very small fields. The mean squared deviation does not decrease significantly. Hence, it can be assumed to be small compared to D.

However, small additional ligand field parameters are, non-diagonal contributions to the Hamiltonian like the E parameter would lead to new eigenstates which are mixtures of different M states. Determining the degree of mixture would give a further estimate of the validity of the model 5.1.

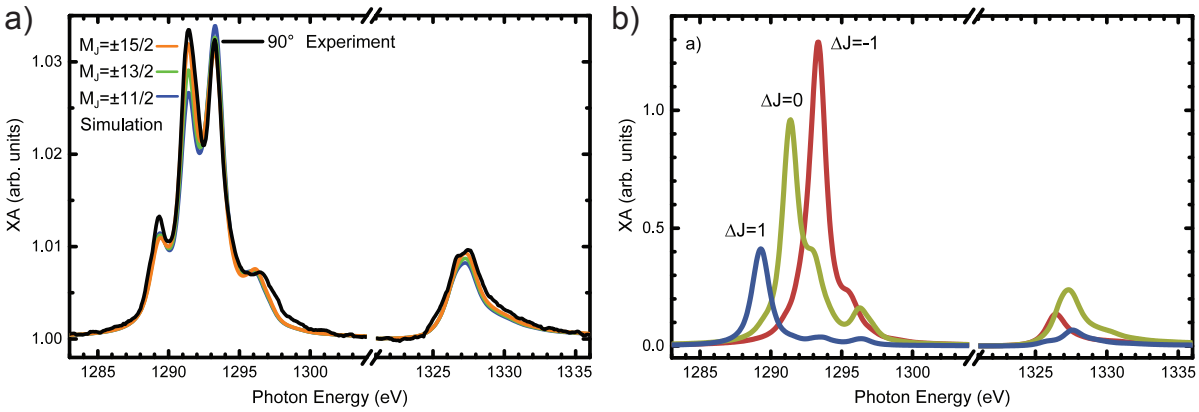

Figure 5.9: a) Calculated Dy $M_{4,5}$ XA spectra for three initial-state doublets and experimental spectrum measured with linearly polarized X-rays and the E vector parallel to the surface; b) calculated Dy-$M_{4,5}$ XA spectra in the absence of a ligand field for the three dipole-allowed transitions $\Delta J = 0, \pm 1$.

In order to exactly identify the ground state, the experimental spectra can be compared to calculated spectra for different M. Already in Figure 5.5 a) the agreement of the simulated curves assuming an $M = \frac{15}{2}$ ground state to the experimental data is clearly visible. In Figure 5.9 a) calculated spectra for three initial state doublets with maximum angular momentum projection are compared to an experimental Dy $M_{4,5}$ XA spectrum. The XA spectrum was measured with linearly polarized X-rays and the E vector parallel to the surface and is the one marked 90° in a). The simulations have been performed by first calculating the Dy $M_{4,5}$ XA spectra of a Dy^{3+} ion separately for each of the $J = 0, \pm 1$ dipole transitions that are presented in Figure 5.9 b). The final spectrum is calculated as the sum of these three contributions using weighting factors that depend on the initial state, the helicity, and the orientation of the light, as described in the Appendix of [114]. These weighting factors are shown for the individual Kramers doublets and a situation in which the symmetry axis of the f orbitals is parallel and the incidence of the X-rays is perpendicular to the surface.

Qualitatively, Figure 5.9 a) shows that initial states with higher M lead to a higher intensity at the $\Delta J = 0$ peak at the M_5 edge with the $M = \pm 15/2$ having the highest intensity. The $\Delta J = 0$ peak in the experimental data has at least of the intensity of the simulated $M = \pm 15/2$ curve and is distinctively higher than the $M = \pm 13/2$ case. Hence, the initial state in the experiment can be unambiguously identified as the $M = \pm 15/2$ state, thereby validating the assumed model.

Anisotropy parameters with higher powers of the projection operators of the total orbital angular momentum play a crucial role in systems with crystallographic point group symmetry as has been discussed in chapter 2. The symmetry of ligand field created by three ligands whose coordination is rather determined by the adsorption on the surface than the coordination chemistry of the central ion does not likely fall into the crystallographic point group. The higher powers of the angular momentum operators correspond to higher order terms of a multipole expansion of the electric field of the ligands. The isolated nature of the 4f-shell provides a distance between the ligand charge and the 4f shell that makes the effect of higher multipole terms significantly smaller than that of lower terms. Therefore, higher powers of the angular momentum operator can be neglected in the Hamiltonian.

5.4 Inelastic tunneling spectra and the first excited state energy

It would be desirable if the magnetic state of an individual molecule could be read out. With the STM tip one can directly address the spin states of individual atoms or molecules and detect their magnetic excitations by inelastically tunneling electrons [125, 126, 127]. With the central ion in the $Dy(tta)_3$ lying in a well defined ground state and having a good estimate of the energy separation between the ground state and the first excited state, magnetic excitations by tunneling electrons of a particular known energy can be expected.

With the above derived magnetic ground state of $J = 15/2$ and $M = \pm 15/2$ as well as a pronounced easy axis of anisotropy, with $D = -0.68(15)$ meV, we expect possible inelastic transitions from the $M = \pm 15/2$ to the $M = \pm 13/2$ state with $E = D[(15/2)^2 - (13/2)^2] = -9.5(2.1)$ meV. The involved levels are visualized as the two lowest levels in the diagram of the anisotropy barrier in Figure 5.10 a). Differential conductance spectra on single molecules indeed exhibit symmetric steps at $\pm 7.7(3)$ meV around the Fermi level with a change of conductance of 10% as is depicted in Figure 5.10 b). This transition could therefore correspond to the inelastic excitation from the $M = \pm 15/2$ ground state to the $M = \pm 13/2$ first excited state. Although this is in agreement with the XA data, a different origin, like the excitation of molecular vibrations, must be ruled out. To account for alternative explanations of the inelastic excitations, the most natural test is to perform the IETS on isostructural molecules with a Gd^{3+} center. $Gd(tta)_3$ exhibits the

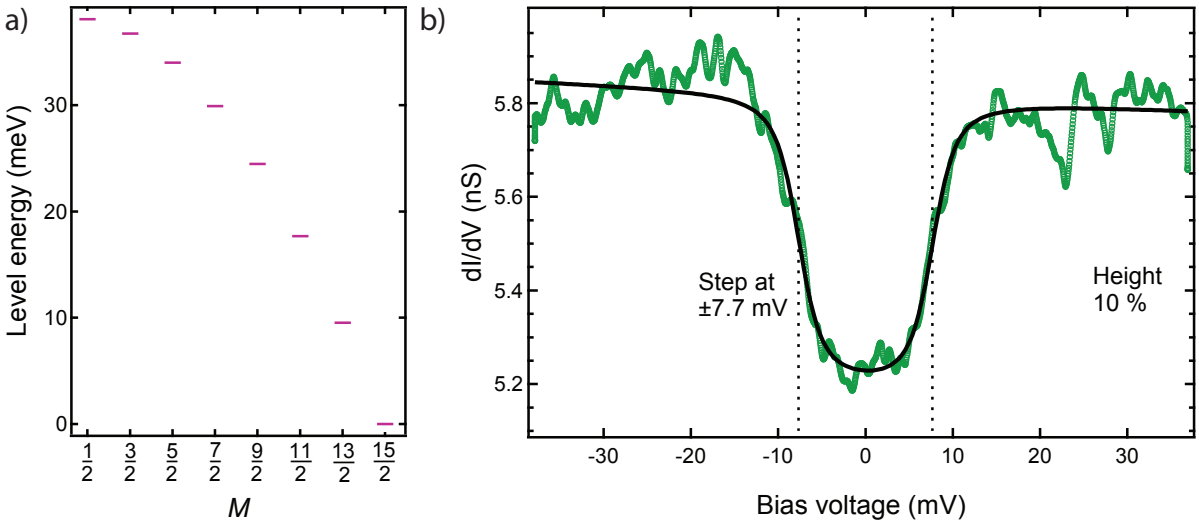

Figure 5.10: a) Estimated energy levels according to anisotropy parameters from XMCD; b) STS spectra show inelastic excitations on $Dy(tta)_3$, black lines are fits using an arctan-step function to determine the step positions ($\pm 7.7(3)$ mV) and height (10% of the dI/dV amplitude).

same structural and electronic properties as $Dy(tta)_3$. Gd^{3+}, however, has a half-filled 4f shell. Hence, the total angular momentum is zero and we do not expect a sizable magnetic anisotropy, due to the absence of spin-orbit coupling in the Hund's rules ground state.

5.5 Adsorption structure of $Gd(tta)_3$ on Au(111)

The $Gd(tta)_3$ complexes have been evaporated at 470 K and deposited at room temperature onto the clean Au(111) surface and postannealed to 385 K, similar to the preparation with $Dy(tta)_3$. In both cases, close-packed islands are observed, which align with the herringbone reconstruction (compare Figures 5.11a), c) and 5.2).

Importantly, the STM images of $Gd(tta)_3$ also reveal a similar appearance of the individual molecules. They consist of a bright oval shape, which are attributed to an upright standing tta ligand, and a lower protrusion associated with two almost flat-lying tta ligands. The comparison of the differential conductance spectra reveals the similarity of the frontier molecular orbitals of the Gd- and Dy-complex and thus reflect the equivalent orientation of the molecules on the surface (Figures 5.11b) and 5.4).

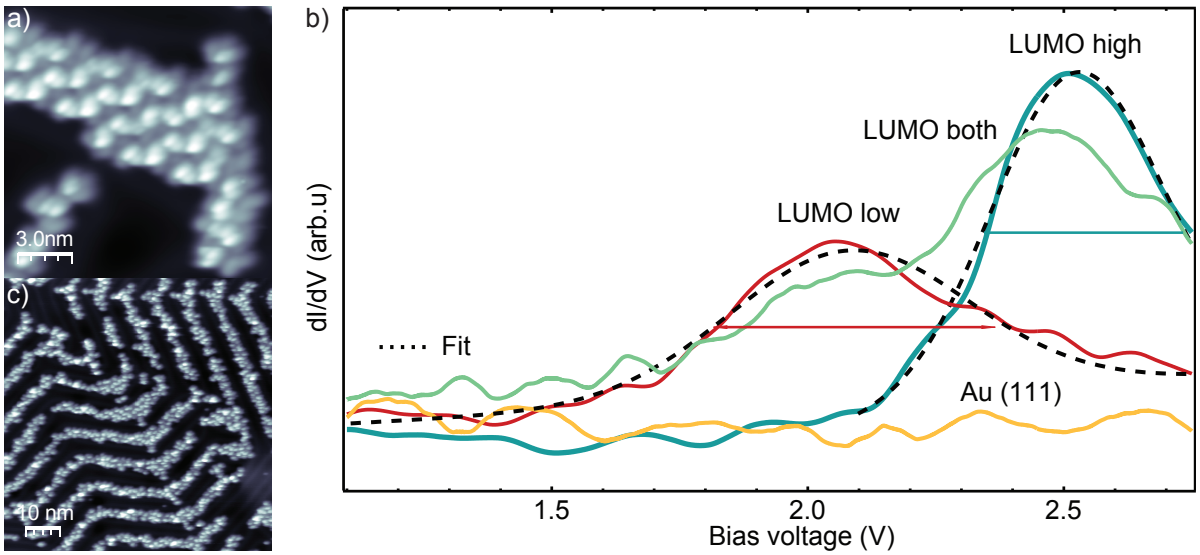

Figure 5.11: a) and c): STM images of $Gd(tta)_3$ on Au(111) ($V = 0.65\,V$, $I = 70\,pA$). They reveal the close resemblance to the molecular arrangement and orientation of $Dy(tta)_3$ on Au(111); b) dI/dV spectra on $Gd(tta)_3$ on Au(111): a peak at 2080 mV with FWHM of 549 mV is found on the lower protrusion (red) and a peak at 2523 mV, FWHM of 389 mV is found on the higher protrusion (blue); both peaks appear simultaneously when tunneling through both ligand types in the center of the molecule (green). The peak positions vary by ≈ 100 mV depending on the arrangement of the neighbouring molecules.

5.5.1 XA spectroscopy on $Gd(tta)_3$ on Au(111)

As in the case of $Dy(tta)_3$, XA spectroscopy is performed on the control molecule $Gd(tta)_3$ to confirm the identical ionization and the expected absence of zero-field splitting.

Angle-dependent Gd $M_{4,5}$ XA spectra for linear polarization are shown in Figure 5.12 a). The shape of the spectrum recorded at the magic angle (55°) is typical for Gd in its 3+ oxidation state [61]. The 4f shell is half-filled with a spin of $S = 7/2$ and a vanishing angular momentum. No significant angle-dependent variation of the spectra is observed, as can be seen from the vanishing XNLD spectrum in the lower part of Figure 5.12 a), given by the difference between the spectra recorded at 90° and 25° X-ray incidence. Gd $M_{4,5}$ XA and XMCD spectra recorded at $B = 6\,T$ and $T = 4.5\,K$ with circular polarization are shown in the Figure 5.12 b) for 90° and 20° X-ray incidence. Again, no significant variation of the spectra with the incidence angle is observed, as is expected in an atomic shell with vanishing angular momentum. As in the case of the Dy XA spectra presented above, all spectra shown in Figure 5.12 are fitted simultaneously with spectra

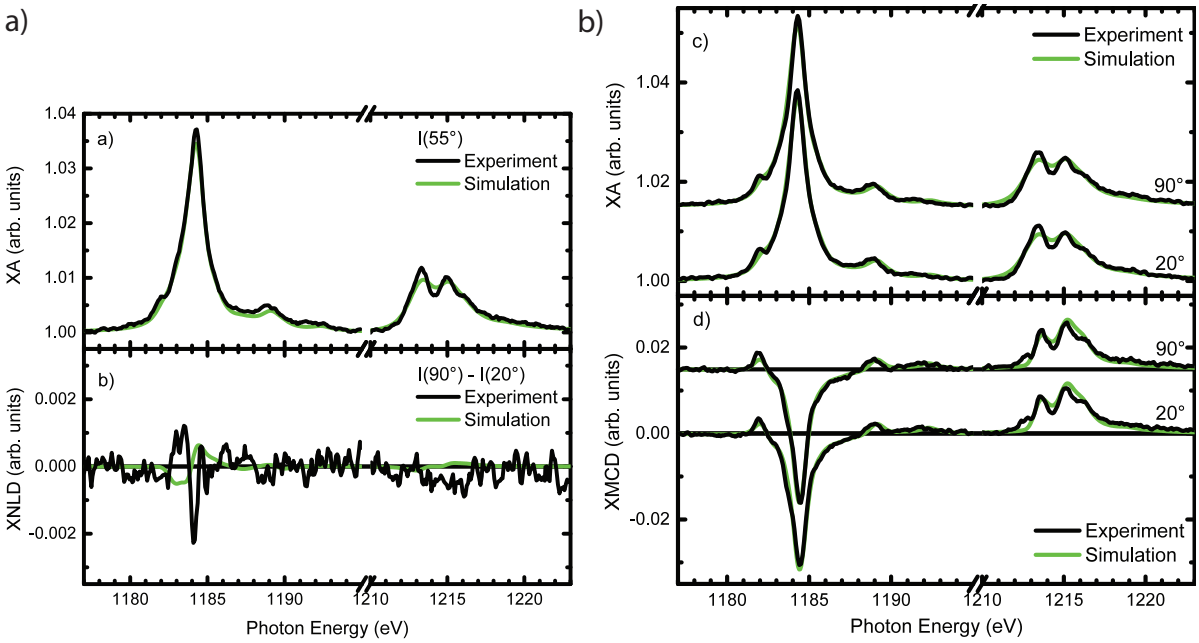

Figure 5.12: Angle-dependent Gd $M_{4,5}$ XA a) and XNLD as well as XA and XMCD b) of 0.2 ML $Gd(tta)_3$ on Au(111) recorded at T = 4.5K. The spectra shown in panel a) are measured in a small magnetic field of 20 mT with angles of 20° , 55°, and 90° between the E vector of the linearly polarized X-rays and the surface normal. The spectra shown in panel b) are measured in a magnetic field of 6 T applied parallel to the k vector of the circularly polarized X-rays. Simulated spectra fitted to the experimental ones are shown in green.

(green lines) obtained from multiplet calculations as explained in the appendix of [114].

In Figure 5.13, the integrated Gd M_5 XMCD signal is plotted as a function of magnetic field along the k vector of the X-rays for 20° and 90° incidence angles. The XMCD signal at 90° incidence is only slightly smaller than the one at 20°, indicating a small magnetic anisotropy. Due to the vanishing angular momentum, such an anisotropy cannot be explained by electrons occupying pure 4f states. Presumably, it is a consequence of a slight hybridization between the 4f and 5d states. This leads to a small magnetic anisotropy that can be described by Equation 5.1. The difference in magnetization for 20° and 90° incidence can be matched by many combinations of anisotropy parameters and orientations of the anisotropy axes.

The theoretical integrated XMCD curves shown in Figure 5.13 are a fit to the experimental data assuming anisotropy axes parallel to the surface. The best fit is obtained for $D = 0.02\,\text{meV}$. In this situation, the first excited state is only 0.3 meV higher in energy

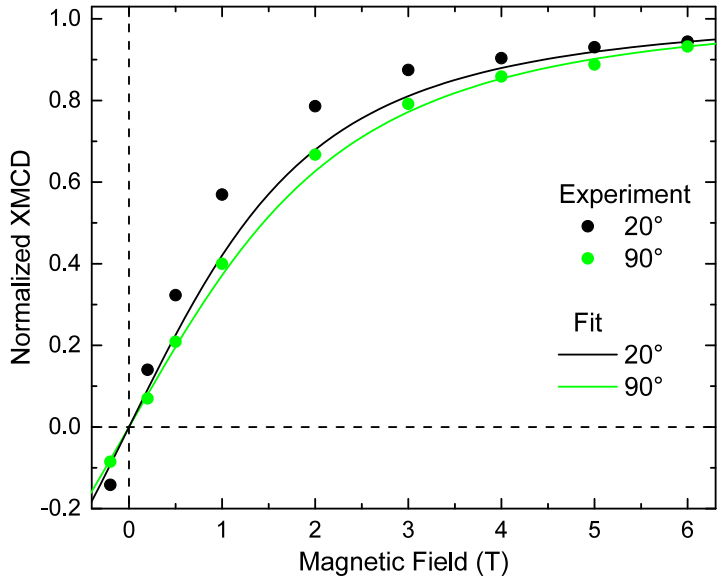

Figure 5.13: Integrated Gd M_5 XMCD signals recorded at 20° (black symbols) and 90° (green symbols) incidence angles as a function of external magnetic field at a temperature of 4.5 K. Lines are a fit to the experimental data of the model described in the main text. The XMCD signal has been normalized to its saturated value.

than the ground state.

5.5.2 Non-magnetic origin of inelastic excitations in $Gd(tta)_3$

Inelastic excitations of vibrations in the tunneling spectroscopy of organic molecules are similarly common as inelastic excitations in magnetic metal centers. Magnetic excitations, however, require a lifting of degeneracy in a quantum number by either a magnetic field or, in absence of a magnetic field, a sizable magnetic anisotropy.

Due to the absence of a sizable magnetic anisotropy in the XMCD data, no inelastic excitations of magnetic origin should occur in the differential conductance spectra recorded on the Gd complexes. However, inelastic tunneling spectra on the $Gd(tta)_3$ complex show a very similar inelastic step for the Dy-complex as seen in figure 5.14. Hence, these excitations can safely be assumed to originate from molecular vibrations. The prominent exposure and its decoupling from the substrate render the upper ligand very sensitive to vibrational excitations by the tunneling electrons. The absence of inelastic spin excitations could be due to several reasons. First, tunneling into particular f states could be suppressed by symmetry [128]. However, in the present case, the 4f states remain largely unperturbed and close to spherical symmetry. The tunneling coupling should therefore not underlie symmetry selection rules due to their shape. Second, the 4f electrons are hardly accessible with the tunneling electrons. The tunneling path is

probably dominated by the molecular states of the ligand, which are coupled to the 5d and 6s electrons of the rare-earth ion by coordination bonding. The hybridization of the 4f electrons with the Fermi level of the electrodes is likely to be small, such that the magnetic information cannot be accessed directly by electronic transport measurements [129].

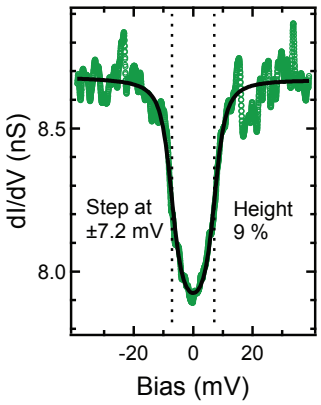

Figure 5.14: STS showing inelastic excitations of $Gd(tta)_3$; black lines show arctan-step function fit to determine the step position ($\pm 7.2(4)$ mV) and height (10% of the dI/dV amplitude).

5.6 Summary

In the research of single magnetic centers as computing devices the adsorption of metal organic complexes on metal surfaces serves two purposes. First, the metal surface itself is a metallic lead for a possible electronic readout. Second, the adsorption changes the coordination geometry, thereby affecting the anisotropy barrier in the magnetic center.

Due to their high magnetic moment and anisotropy, $Dy(tta)_3$ molecules are ideal candidates for magnetic data storage when adsorbed on a surface. The adsorption configuration on Au(111) forces two of the three tta ligands into the surface plane. The ligand field imposes a distinguished orientation of the symmetry axis of the f orbitals and direction of magnetization parallel to the surface. Such an easy-axis anisotropy is an ideal situation for creating large anisotropy barriers. The ground state of the Dy^{3+} ion has the maximum projected magnetic moment of $M = \pm 15/2$, in contrast to Dy-bis(phthalocyaninato) complexes, where an $M = \pm 13/2$ ground state has been observed [108].

$Gd(tta)_3$ molecules adsorb in exactly the same configuration. However, due to the half-filled 4f shell, their anisotropy is vanishingly small, as expected. Features seen in inelastic tunneling spectra appear identically in both systems and are thus attributed to vibrational excitations. No spin excitations are distinguished in the tunneling spectra, which is due to the rather shielded nature of the 4f electrons.

To couple the 4f electrons more effectively to the electric leads, the 4f levels have to lie energetically closer to the frontier orbitals of the ligand and to the Fermi level of the leads. A different choice of organic ligand such as in a metallocene is known to show a higher mixing of molecular orbitals and the 4f shell of lanthanides [130].

Changing the ligand certainly also affects the anisotropy barrier of the metal center. Some dysprosocenes have shown hysteresis at temperatures as high as 60 mK [131]. Whether this properties would be enhanced upon adsorption onto a metal surface or whether they would vanish cannot be estimated in advance. However, the search for conveniently readable single atom magnetic memory might reach its goal in single-ion metal organic complexes adsorbed on metal surfaces.

6 Summary

In this thesis two molecular systems that show an energy barrier between two distinct states were investigated by STM at liquid helium temperatures. In both systems the question of addressing by the electric current was evaluated.

The TCNE in the TTF/TCNE on Au(111) charge transfer complex shows two distinct conformational states, one significantly bent towards the surface and another that is rather flat. The bending is likely facilitated by a rehybridization from sp^2 towards sp^3 at the two central C atoms that stems from the π-accepting bond with d-orbitals of the substrate. The bond and the bending affect the energy landscape and the barrier between the two states. The states differ in conductance, which makes a readout possible.

The presence of the Kondo effect in the flat conformational, high conducting state and the absence in the bent state hint at different charge states. However, roughly the same charge of the two conformational states could be established by measurements of LCPD and comparison to simulated electric potential curves. The assessment of charge is possible because the state that exhibits the Kondo effect certainly accepts exactly one electron from the surface into the LUMO. The difference in LCPD between the Kondo-TCNE and the TTF that donates one electron to the surface, is a gauge for the charge visible by LCPD.

The absence of the visible Kondo effect in the bent state can be explained by a change in the Kondo temperature due to different parameters of the Anderson impurity model in the bent state. The hybridization with the d-states of the substrate rather than with the conduction band, goes along with a lower hybridization Δ and a higher distance of the singly occupied LUMO state from the Fermi-level ϵ_S.

The switching dynamics of the TCNE was investigated by measuring switching rates from the random telegraph noise in two different ordered phases of the TTF/TCNE. By applying the ladder climbing model the number of inelastic excitations needed to switch from the thermally stable bent state into the high conducting state can be counted.

An energy barrier height in the order of magnitude of 200 mV is estimated. From the evaluation of the switching rates into the thermally stable state it is concluded that an additional thermal process is involved. This difference in switching dynamics allows a controlled switching into the desired state. A high current increases the probability that the random telegraph noise terminates in the high conducting state, while a low current increases the probability to end in the thermally stable state.

In the case of a magnetic moment of the central ion in the metal-organic complex $Dy(tta)_3$ the energy barrier between the states of opposite magnetic moment is the uniaxial magnetic anisotropy. Dysprosium is chosen as metal center for its high magnetic moment and the potentially large anisotropy barrier that results from the large moment.

The uniaxial magnetic anisotropy is detected by XMCD and XNLD. The estimated size of the anisotropy barrier between the two wells of about 40 mV exceeds the thermal energy at room temperature. Although the potential has the right double-well shape, it is too shallow to result in a magnetic hysteresis. The shape of the potential is induced by two of the negatively charged tta ligands that coordinate from opposite sides of the Dy atom. The surface acts as a neutral ligand. The coordination is deduced from STM, dI/dV as well as from NEXAFS measurements.

The question of addressing by tunneling electrons is more difficult in the case of $Dy(tta)_3$. Inelastic excitations with the correct energy to be excitations from the $M = \pm 15/2$ ground state to the first excited state $M = \pm 13/2$ are detected in dI/dV. A test molecule $Gd(tta)_3$ is investigated and shows as expected no relevant magnetic anisotropy. It shows, however, the same inelastic excitations. This means that the excitations in $Dy(tta)_3$ are non-magnetic but likely vibrational.

What is common to both systems, the TTF/TCNE and the $Dy(tta)_3$, is not only that an energetic barrier is formed. In both cases it is only through the adsorption of the molecule on the surface that the energetic barrier arises in the observed form. In the TCNE, the molecule can bond to the surface in two different geometries, creating two potential wells. In the adsorption of $Dy(tta)_3$, the surface orients the molecule and thereby the orientation of its magnetic anisotropy as well as acts as a neutral ligand needed for the creation of the anisotropy. This is in contrast to adsorption of molecules on the surface which already posses the desired properties in solution or in a crystal such as chemical switches [132] or organic molecules with a metal center such as the double-decker molecules $TbPc_2$

or $DyPc_2$ [133]. As the examples in the present thesis demonstrate, not only does the contact to the metal surface allow to electrically probe the molecules and observe the phenomena in them, but also creates properties and phenomena that otherwise would not be present.

Bibliography

[1] M. Julliere, "Tunneling between ferromagnetic films," *Physics Letters A*, vol. 54, pp. 225–226, Sept. 1975.

[2] C. Chappert, A. Fert, and F. N. Van Dau, "The emergence of spin electronics in data storage," *Nature Materials*, vol. 6, pp. 813–823, Nov. 2007.

[3] G. Binasch, P. Grünberg, F. Saurenbach, and W. Zinn, "Enhanced magnetoresistance in layered magnetic structures with antiferromagnetic interlayer exchange," *Physical Review B*, vol. 39, pp. 4828–4830, Mar. 1989.

[4] J. Bardeen, "Semiconductor research leading to the point contact transistor," *Nobel Lecture*, Dec. 1956.

[5] W. H. Brattain, "Transistor technology evokes new physics," *Nobel Lecture*, Dec. 1956.

[6] W. Shockley, "Transistor technology evokes new physics," *Nobel Lecture*, Dec. 1956.

[7] G. E. Moore, "Cramming more components onto integrated circuits, reprinted from electronics, volume 38, number 8, april 19, 1965, pp.114 ff.," *IEEE Solid-State Circuits Society Newsletter*, vol. 11, no. 3, pp. 33–35, 2006.

[8] G. Binnig, H. Rohrer, C. Gerber, and E. Weibel, "Surface studies by scanning tunneling microscopy," *Physical Review Letters*, vol. 49, pp. 57–61, July 1982.

[9] G. Binnig, C. F. Quate, and C. Gerber, "Atomic force microscope," *Phys. Rev. Lett.*, vol. 56, pp. 930–933, March 1986.

[10] F. J. Giessibl, "Atomic resolution on Si(111)-(7x7) by noncontact atomic force microscopy with a force sensor based on a quartz tuning fork," *Applied Physics Letters*, vol. 76, no. 11, pp. 1470–1472, 2000.

[11] L. Gross, F. Mohn, N. Moll, P. Liljeroth, and G. Meyer, "The Chemical Structure of a Molecule Resolved by Atomic Force Microscopy," *Science*, vol. 325, pp. 1110–1114, August 2009.

[12] F. Mohn, L. Gross, N. Moll, and G. Meyer, "Imaging the charge distribution within a single molecule," *Nature Nanotechnology*, vol. 7, pp. 227–31, 02 2012.

[13] A. S. Dawydow, *Quantenmechanik. 5., bearbeitete Auflage.* VEB: Kluwer Academic Press, 1987.

[14] J. Bardeen, "Tunnelling from a Many-Particle Point of View," *Physical Review Letters*, vol. 6, pp. 57–59, January 1961.

[15] J. Tersoff and D. R. Hamann, "Theory and application for the scanning tunneling microscope," *Phys. Rev. Lett.*, vol. 50, pp. 1998–2001, Jun 1983.

[16] N. D. Lang, "Spectroscopy of single atoms in the scanning tunneling microscope," *Phys. Rev. B*, vol. 34, pp. 5947–5950, October 1986.

[17] A. Selloni, P. Carnevali, E. Tosatti, and C. D. Chen, "Voltage-dependent scanning-tunneling microscopy of a crystal surface: Graphite," *Phys. Rev. B*, vol. 31, pp. 2602–2605, February 1985.

[18] J. Lambe and R. C. Jaklevic, "Molecular vibration spectra by inelastic electron tunneling," *Phys. Rev.*, vol. 165, pp. 821–832, January 1968.

[19] M. B. Weissman, "$\frac{1}{f}$ noise and other slow, nonexponential kinetics in condensed matter," *Rev. Mod. Phys.*, vol. 60, pp. 537–571, April 1988.

[20] P. Dutta and P. M. Horn, "Low-frequency fluctuations in solids: 1f noise," *Reviews of Modern Physics*, vol. 53, no. 3, pp. 497–516, 1981.

[21] F. J. Giessibl, "Advances in atomic force microscopy," *Rev. Mod. Phys.*, vol. 75, pp. 949–983, July 2003.

[22] C. Lotze, *Fundamental Processes in Single Molecule Junctions.* PhD thesis, Freie Universität Berlin, 2014.

[23] H. Hamaker, "The london-van der waals attraction between spherical particles," *Physica*, vol. 4, pp. 1058–1072, 01 1937.

[24] L. Kelvin, "V. contact electricity of metals," *The London, Edinburgh, and Dublin Philosophical Magazine and Journal of Science*, vol. 46, no. 278, pp. 82–120, 1898.

[25] R. Smoluchowski, "Anisotropy of the electronic work function of metals," *Phys. Rev.*, vol. 60, pp. 661–674, Nov 1941.

[26] R. Temirov, S. Soubatch, O. Neucheva, A. C. Lassise, and F. S. Tautz, "A novel method achieving ultra-high geometrical resolution in scanning tunnelling microscopy," *New Journal of Physics*, vol. 10, p. 053012, May 2008.

[27] K. Besocke, "An easily operable scanning tunneling microscope," *Surface Science*, vol. 181, pp. 145–153, Mar. 1987.

[28] WaveMetrics, Inc., "Igor pro," 1988–2014.

[29] I. Horcas, R. Fernández, J. M. Gómez-Rodríguez, J. Colchero, J. Gómez-Herrero, and A. M. Baro, "WSXM: A software for scanning probe microscopy and a tool for nanotechnology," *Review of Scientific Instruments*, vol. 78, p. 013705, Jan. 2007.

[30] R. Hoffmann, "A chemical and theoretical way to look at bonding on surfaces," *Reviews of Modern Physics*, vol. 60, pp. 601–628, jul 1988.

[31] J. Fraxedas, *Molecular Organic Materials*. Cambridge: Cambridge University Press, 2006.

[32] G. L. Miessler, P. J. Fischer, and D. A. Tarr, *Inorganic Chemistry*. Pearson advanced chemistry series, Pearson, 2014.

[33] L. Bartels, G. Meyer, K.-H. Rieder, D. Velic, E. Knoesel, A. Hotzel, M. Wolf, and G. Ertl, "Dynamics of electron-induced manipulation of individual co molecules on cu(111)," *Phys. Rev. Lett.*, vol. 80, pp. 2004–2007, Mar 1998.

[34] J. Desesquelles, M. Dufay, and M. Poulizac, "Lifetime measurement of molecular states with an accelerated ion beam," *Physics Letters A*, vol. 27, no. 2, pp. 96 – 97, 1968.

[35] R. Hesper, L. H. Tjeng, and G. A. Sawatzky, "Strongly reduced band gap in a correlated insulator in close proximity to a metal," *Europhysics Letters*, vol. 40, no. 2, pp. 177–182, 1997.

[36] D. M. Duffy and A. M. Stoneham, "Conductivity and 'negative U' for ionic grain boundaries," *Journal of Physics C: Solid State Physics*, vol. 16, no. 21, pp. 4087–4092, 1983.

[37] I. F. Torrente, K. J. Franke, and J. I. Pascual, "Spectroscopy of C 60 single molecules: the role of screening on energy level alignment," *Journal of Physics: Condensed Matter*, vol. 20, no. 18, p. 184001, 2008.

[38] M. Ternes, A. J. Heinrich, and W.-D. Schneider, "Spectroscopic manifestations of the Kondo effect on single adatoms.," *Journal of physics. Condensed matter : an Institute of Physics journal*, vol. 21, p. 53001, feb 2009.

[39] L. Kouwenhoven and L. Glazman, "Revival of the Kondo effect," *Physics World*, vol. 14, pp. 33–38, jan 2001.

[40] W. de Haas, J. de Boer, and G. van dÃ«n Berg, "The electrical resistance of gold, copper and lead at low temperatures," *Physica*, vol. 1, no. 7, pp. 1115 – 1124, 1934.

[41] W. Meissner and B. Voigt, "Messungen mit hilfe von flüssigem helium xi widerstand der reinen metalle in tiefen temperaturen," *Annalen der Physik*, vol. 399, no. 7, pp. 761–797, 1930.

[42] J. Kondo, "Resistance Minimum in Dilute Magnetic Alloys," *Progress of Theoretical Physics*, vol. 32, pp. 37–49, jul 1964.

[43] P. W. Anderson, "A poor man's derivation of scaling laws for the Kondo problem," *Journal of Physics C: Solid State Physics*, vol. 3, pp. 2436–2441, dec 1970.

[44] K. G. Wilson, "The renormalization group: Critical phenomena and the Kondo problem," *Rev. Mod. Phys.*, vol. 47, pp. 773–840, Oct 1975.

[45] J. R. Schrieffer and P. A. Wolff, "Relation between the Anderson and Kondo Hamiltonians," *Physical Review*, vol. 149, pp. 491–492, sep 1966.

[46] P. W. Anderson, "Localized Magnetic States in Metals," *Physical Review*, vol. 124, pp. 41–53, oct 1961.

[47] F. D. M. Haldane, "Theory of the atomic limit of the anderson model. i. perturbation expansions re-examined," *Journal of Physics C: Solid State Physics*, vol. 11, pp. 5015–5034, dec 1978.

[48] J. Jensen and A. Mackintosh, *Rare earth magnetism: structures and excitations*. International series of monographs on physics, Clarendon Press, 1991.

[49] J. M. D. Coey, *Magnetism and Magnetic Materials*. Cambridge University Press, 2010.

[50] A. Abragam and B. Bleaney, *Electron Paramagnetic Resonance of Transition Ions*. The international series of monographs on physics, Oxford University Press, 1970.

[51] Stöhr, J, *Magnetism From Fundamentals to Nanoscale Dynamics*. Springer Series in Solid-State Sciences, Springer-Verlag Berlin Heidelberg, 2006.

[52] H. Lueken, *Magnetochemie: Eine Einführung in Theorie und Anwendung*. Teubner Studienbücher Chemie, Vieweg+Teubner Verlag, 2013.

[53] J. Van Vleck, *The Theory of Electric and Magnetic Susceptibilities*. International series of monographs on physics, Clarendon Press, 1932.

[54] K. W. H. Stevens, "Matrix Elements and Operator Equivalents Connected with the Magnetic Properties of Rare Earth Ions," *Proceedings of the Physical Society. Section A*, vol. 65, pp. 209–215, mar 1952.

[55] J. Rinehart and J. Long, "Exploiting single-ion anisotropy in the design of f-element single-molecule magnets," *Chem. Sci.*, vol. 2, no. 11, p. 2078, 2011.

[56] J. Sievers, "Asphericity of 4f-shells in their Hund's rule ground states," *Zeitschrift für Physik B Condensed Matter*, vol. 45, no. 4, pp. 289–296, 1982.

[57] N. F. Chilton, D. Collison, E. J. L. McInnes, R. E. P. Winpenny, and A. Soncini, "An electrostatic model for the determination of magnetic anisotropy in dysprosium complexes," *Nature Communications*, vol. 4, p. 2551, oct 2013.

[58] J. Stöhr and R. Gomer, *NEXAFS Spectroscopy*. Springer Series in Surface Sciences, Springer, 1992.

[59] M. Bernien, *X-Ray absorption spectroscopy of Fe complexes on surfaces*. PhD thesis, Freie Universität Berlin, 2010.

[60] B. T. Thole, G. Van Der Laan, J. C. Fuggle, G. A. Sawatzky, R. C. Karnatak, and J. M. Esteva, "3D X-Ray-Absorption Lines and the 3D94Fn+1 Multiplets of the Lanthanides," *Physical Review B*, vol. 32, pp. 5107–5118, oct 1985.

[61] J. B. Goedkoop, B. T. Thole, G. Van Der Laan, G. a. Sawatzky, F. M. F. De Groot, and J. C. Fuggle, "Calculations of magnetic x-ray dichroism in the 3d absorption spectra of rare-earth compounds," *Physical Review B*, vol. 37, pp. 2086–2093, feb 1988.

[62] R. D. Cowan, "Theoretical calculation of atomic spectra using digital computers∗," *J. Opt. Soc. Am.*, vol. 58, pp. 808–818, Jun 1968.

[63] R. D. Cowan, *The theory of atomic structure and spectra*. University of California Press: Berkeley, 1981.

[64] M. Sacchi, O. Sakho, and G. Rossi, "Strong dichroism in the dy 3d→4f x-ray absorption at dy/si(111) interfaces," *Phys. Rev. B*, vol. 43, pp. 1276–1278, Jan 1991.

[65] J. Goedkoop, *X-Ray dichroism of rare earth materials.* PhD thesis, Katholieke Universiteit te Nijmegen, 1989.

[66] I. Fernandez-Torrente, S. Monturet, K. Franke, J. Fraxedas, N. Lorente, and J. Pascual, "Long-Range Repulsive Interaction between Molecules on a Metal Surface Induced by Charge Transfer," *Physical Review Letters*, vol. 99, p. 176103, oct 2007.

[67] D. Wegner, R. Yamachika, Y. Wang, V. W. Brar, B. M. Bartlett, J. R. Long, and M. F. Crommie, "Single-molecule charge transfer and bonding at an organic/inorganic interface: tetracyanoethylene on noble metals.," *Nano letters*, vol. 8, pp. 131–135, jan 2008.

[68] T. Choi, S. Bedwani, A. Rochefort, C.-Y. Chen, A. J. Epstein, and J. Gupta, "A single molecule Kondo switch: multistability of tetracyanoethylene on Cu(111).," *Nano Letters*, vol. 10, pp. 4175–4180, oct 2010.

[69] J. Kortright, D. Lincoln, R. Edelstein, and a. Epstein, "Bonding, Backbonding, and Spin-Polarized Molecular Orbitals: Basis for Magnetism and Semiconducting Transport in V[TCNE]x~2," *Physical Review Letters*, vol. 100, pp. 2–5, jun 2008.

[70] P. Stoll, C. Lotze, J. N. Ladenthin, T. R. Umbach, I. Fernández-Torrente, and K. J. Franke, "Correlation of Kondo effect and molecular conformation of the acceptor molecule in the TTF-TCNE charge transfer complex," *Journal of Physics: Condensed Matter*, vol. 30, p. 454002, Oct. 2018.

[71] I. F. Torrente, K. J. Franke, and J. I. Pascual, "Electron Transfer Phenomena at the Molecular Scale," vol. 2, pp. 51–75, 2011.

[72] T. R. Umbach, M. Fernandez-Torrente, I.and Ruby, F. Schulz, C. Lotze, R. Rurali, M. Persson, and K. J. Pascual, J. I.and Franke, "Atypical charge redistribution over a charge-transfer monolayer on a metal," *New Journal of Physics*, vol. 15, pp. 083048–, August 2013.

[73] D. A. Clemente and A. Marzotto, "Structure of two polymorphs of the TTF-TCNE

charge-transfer complex and the degree of ionicity," *Journal of Materials Chemistry*, vol. 6, no. 6, pp. 941–946, 1996.

[74] M. Meneghetti and C. Pecile, "TTF–TCNE a charge transfer π–molecular crystal with partial ionic ground state: Optical properties and electron-molecular vibrations interaction," *The Journal of Chemical Physics*, vol. 105, no. 2, p. 397, 1996.

[75] I. Fernández-Torrente, K. Franke, and J. Pascual, "Vibrational Kondo Effect in Pure Organic Charge-Transfer Assemblies," *Physical Review Letters*, vol. 101, p. 217203, nov 2008.

[76] N. Moll, L. Gross, F. Mohn, A. Curioni, and G. Meyer, "The mechanisms underlying the enhanced resolution of atomic force microscopy with functionalized tips," *New Journal of Physics*, vol. 12, p. 125020, dec 2010.

[77] P. Hapala, R. Temirov, F. S. Tautz, and P. Jelínek, "Origin of High-Resolution IETS-STM Images of Organic Molecules with Functionalized Tips," *Physical Review Letters*, vol. 113, p. 226101, nov 2014.

[78] P. Hapala, G. Kichin, C. Wagner, F. S. Tautz, R. Temirov, and P. Jelínek, "Mechanism of high-resolution STM/AFM imaging with functionalized tips," *Physical Review B*, vol. 90, p. 085421, aug 2014.

[79] L. Gross, F. Mohn, N. Moll, B. Schuler, A. Criado, E. Guitian, D. Pena, A. Gourdon, and G. Meyer, "Bond-Order Discrimination by Atomic Force Microscopy," *Science*, vol. 337, pp. 1326–1329, sep 2012.

[80] J. Zhang, P. Chen, B. Yuan, W. Ji, Z. Cheng, and X. Qiu, "Real-Space Identification of Intermolecular Bonding with Atomic Force Microscopy," *Science*, vol. 342, pp. 611–614, nov 2013.

[81] N. D. Lang and W. Kohn, "Theory of metal surfaces: Induced surface charge and image potential," *Phys. Rev. B*, vol. 7, pp. 3541–3550, Apr 1973.

[82] N. V. Smith, C. T. Chen, and M. Weinert, "Distance of the image plane from metal surfaces," *Phys. Rev. B*, vol. 40, pp. 7565–7573, Oct 1989.

[83] T. Miyamachi, T. Schuh, T. Märkl, C. Bresch, T. Balashov, A. Stöhr, C. Karlewski, S. André, M. Marthaler, M. Hoffmann, M. Geilhufe, S. Ostanin, W. Hergert, I. Mertig, G. Schön, A. Ernst, and W. Wulfhekel, "Stabilizing the magnetic

moment of single holmium atoms by symmetry," *Nature*, vol. 503, pp. 242–6, Nov. 2013.

[84] S. Chelkowski, A. D. Bandrauk, and P. B. Corkum, "Efficient molecular dissociation by a chirped ultrashort infrared laser pulse," *Physical Review Letters*, vol. 65, no. 19, pp. 2355–2358, 1990.

[85] D. M. Eigler, C. P. Lutz, and W. E. Rudge, "An atomic switch realized with the scanning tunnelling microscope," *Nature*, vol. 352, pp. 600–603, aug 1991.

[86] B. Stipe, M. Rezaei, W. Ho, S. Gao, M. Persson, and B. Lundqvist, "Single-Molecule Dissociation by Tunneling Electrons," *Physical Review Letters*, vol. 78, no. 23, pp. 4410–4413, 1997.

[87] B. C. Stipe, M. a. Rezaei, and W. Ho, "Coupling of Vibrational Excitation to the Rotational Motion of a Single Adsorbed Molecule," *Physical Review Letters*, vol. 81, pp. 1263–1266, aug 1998.

[88] R. E. Walkup, D. M. Newns, and P. Avouris, "Role of multiple inelastic transitions in atom transfer with the scanning tunneling microscope," *Physical Review B*, vol. 48, pp. 1858–1861, jul 1993.

[89] S. Gao, M. Persson, and B. I. Lundqvist, "Theory of atom transfer with a scanning tunneling microscope," *Physical Review B*, vol. 55, pp. 4825–4836, feb 1997.

[90] S. Tikhodeev and H. Ueba, "How Vibrationally Assisted Tunneling with STM Affects the Motions and Reactions of Single Adsorbates," *Physical Review Letters*, vol. 102, pp. 1–4, jun 2009.

[91] G. P. Salam, M. Persson, and R. E. Palmer, "Possibility of coherent multiple excitation in atom transfer with a scanning tunneling microscope," *Physical Review B*, vol. 49, pp. 10655–10662, Apr. 1994.

[92] T. Komeda, "Lateral hopping of molecules induced by excitation of internal vibration mode," *Science*, vol. 295, no. 5562, pp. 2055–2058, 2002.

[93] N. Gonzalez-Lakunza, I. Fernández-Torrente, K. J. Franke, N. Lorente, A. Arnau, and J. I. Pascual, "Formation of dispersive hybrid bands at an organic-metal interface.," *Physical Review Letters*, vol. 100, p. 156805, Apr. 2008.

[94] M. Ohara, Y. Kim, S. Yanagisawa, Y. Morikawa, and M. Kawai, "Role of molecular orbitals near the fermi level in the excitation of vibrational modes of a single

molecule at a scanning tunneling microscope junction," *Physical Review Letters*, vol. 100, no. 13, pp. 1–4, 2008.

[95] J. Wirth, N. Hatter, R. Drost, T. R. Umbach, S. Barja, M. Zastrow, K. Rück-Braun, J. I. Pascual, P. Saalfrank, and K. J. Franke, "Diarylethene molecules on a Ag(111) surface: Stability and electron-induced switching," *The Journal of Physical Chemistry C*, vol. 119, pp. 4874–4883, Feb. 2015.

[96] M. Alemani, M. V. Peters, S. Hecht, K.-H. Rieder, F. Moresco, and L. Grill, "Electric field-induced isomerization of azobenzene by STM.," *Journal of the American Chemical Society*, vol. 128, pp. 14446–7, November 2006.

[97] G. Schulze, K. J. Franke, A. Gagliardi, G. Romano, C. S. Lin, A. L. Rosa, T. A. Niehaus, T. Frauenheim, A. D. Carlo, A. Pecchia, and J. I. Pascual, "Resonant electron heating and molecular phonon cooling in Single C60 junctions," *Physical Review Letters*, vol. 100, Apr. 2008.

[98] L. Bogani and W. Wernsdorfer, "Molecular spintronics using single-molecule magnets.," *Nature materials*, vol. 7, pp. 179–186, March 2008.

[99] D. Gatteschi and R. Sessoli, "Quantum tunneling of magnetization and related phenomena in molecular materials," *Angewandte Chemie - International Edition*, vol. 42, no. 3, pp. 268–297, 2003.

[100] M. N. Leuenberger and D. Loss, "Quantum computing in molecular magnets.," *Nature*, vol. 410, pp. 789–793, April 2001.

[101] G. Christou, D. Gatteschi, D. N. Hendrickson, and R. Sessoli, "Single-Molecule Magnets," *MRS bulletin*, vol. 25, no. 11, pp. 66–71, 2000.

[102] A. Caneschi, D. Gatteschi, R. Sessoli, A.-L. Barra, L.-C. C. Brunel, and M. Guillot, "Alternating current susceptibility, high field magnetization, and millimeter band EPR evidence for a ground S = 10 state in [Mn12O12(Ch3COO)16(H2O)4].2CH3COOH.4H2O," *Journal of the American Chemical Society*, vol. 113, no. 15, pp. 5873–5874, 1991.

[103] R. Sessoli, D. Gatteschi, A. Caneschi, and M. a. Novak, "Magnetic bistability in a metal-ion cluster," *Nature*, vol. 365, pp. 141–143, September 1993.

[104] D. Gatteschi, R. Sessoli, and A. Cornia, "Single-molecule magnets based on iron(iii) oxo clusters," *Chemical Communications*, no. 9, pp. 725–732, 2000.

[105] C. J. Milios, A. Vinslava, W. Wernsdorfer, S. Moggach, S. Parsons, S. P. Perlepes, G. Christou, and E. K. Brechin, "A record anisotropy barrier for a single-molecule magnet," *Journal of the American Chemical Society*, vol. 129, no. 10, pp. 2754–2755, 2007.

[106] M. Mannini, F. Pineider, P. Sainctavit, C. Danieli, E. Otero, C. Sciancalepore, A. M. Talarico, M.-A. Arrio, A. Cornia, D. Gatteschi, and R. Sessoli, "Magnetic memory of a single-molecule quantum magnet wired to a gold surface," *Nature Materials*, vol. 8, pp. 194–197, March 2009.

[107] P. Santini, S. Carretta, F. Troiani, and G. Amoretti, "Molecular nanomagnets as quantum simulators," *Physical Review Letters*, vol. 107, p. 230502, November 2011.

[108] N. Ishikawa, M. Sugita, T. Ishikawa, S. Y. Koshihara, and Y. Kaizu, "Lanthanide double-decker complexes functioning as magnets at the single-molecular level," *Journal of the American Chemical Society*, vol. 125, no. 29, pp. 8694–8695, 2003.

[109] A. Dei and D. Gatteschi, "Molecular (Nano) magnets as test grounds of quantum mechanics," *Angewandte Chemie - International Edition*, vol. 50, no. 50, pp. 11852–11858, 2011.

[110] G. Cucinotta, M. Perfetti, J. Luzon, M. Etienne, P. E. Car, A. Caneschi, G. Calvez, K. Bernot, and R. Sessoli, "Magnetic anisotropy in a dysprosium/DOTA single-molecule magnet: Beyond simple magneto-structural correlations," *Angewandte Chemie - International Edition*, vol. 51, no. 7, pp. 1606–1610, 2012.

[111] J. Dreiser, C. Wäckerlin, M. E. Ali, C. Piamonteze, F. Donati, A. Singha, K. S. Pedersen, S. Rusponi, J. Bendix, P. M. Oppeneer, T. A. Jung, and H. Brune, "Exchange interaction of strongly anisotropic tripodal erbium single-ion magnets with metallic surfaces," *ACS Nano*, vol. 8, no. 5, pp. 4662–4671, 2014.

[112] N. Ishikawa, M. Sugita, and W. Wernsdorfer, "Quantum tunneling of magnetization in lanthanide single-molecule magnets: Bis(phthalocyaninato)terbium and bis(phthalocyaninato)dysprosium anions," *Angewandte Chemie - International Edition*, vol. 44, no. 19, pp. 2931–2935, 2005.

[113] R. Vincent, S. Klyatskaya, M. Ruben, W. Wernsdorfer, and F. Balestro, "Electronic read-out of a single nuclear spin using a molecular spin transistor.," *Nature*, vol. 488, pp. 357–360, August 2012.

[114] P. Stoll, M. Bernien, D. Rolf, F. Nickel, Q. Xu, C. Hartmann, T. R. Umbach, J. Kopprasch, J. N. Ladenthin, E. Schierle, E. Weschke, C. Czekelius, W. Kuch, and K. J. Franke, "Magnetic anisotropy in surface-supported single-ion lanthanide complexes," *Phys. Rev. B*, vol. 94, p. 224426, December 2016.

[115] M. J. Frisch, G. W. Trucks, H. B. Schlegel, G. E. Scuseria, M. A. Robb, J. R. Cheeseman, G. Scalmani, V. Barone, B. Mennucci, G. A. Petersson, H. Nakatsuji, M. Caricato, X. Li, H. P. Hratchian, A. F. Izmaylov, J. Bloino, G. Zheng, J. L. Sonnenberg, M. Hada, M. Ehara, K. Toyota, R. Fukuda, J. Hasegawa, M. Ishida, T. Nakajima, Y. Honda, O. Kitao, H. Nakai, T. Vreven, J. A. Montgomery Jr., J. E. Peralta, F. Ogliaro, M. Bearpark, J. J. Heyd, E. Brothers, K. N. Kudin, V. N. Staroverov, R. Kobayashi, J. Normand, K. Raghavachari, A. Rendell, J. C. Burant, S. S. Iyengar, J. Tomasi, M. Cossi, N. Rega, J. M. Millam, M. Klene, J. E. Knox, J. B. Cross, V. Bakken, C. Adamo, J. Jaramillo, R. Gomperts, R. E. Stratmann, O. Yazyev, A. J. Austin, R. Cammi, C. Pomelli, J. W. Ochterski, R. L. Martin, K. Morokuma, V. G. Zakrzewski, G. A. Voth, P. Salvador, J. J. Dannenberg, S. Dapprich, A. D. Daniels, Ö. Farkas, J. B. Foresman, J. V. Ortiz, J. Cioslowski, and D. J. Fox, "Gaussian09 Revision E.01."

[116] R. P. Yang and W., *Density-Functional Theory of Atoms and Molecules*. International Series of Monographs on Chemistry, Oxford University Press, 1989.

[117] J. A. Hehre, W. J.; Ditchfield, R.; Pople, "Self Consistent Molecular Orbital Methods. XII. Further Extensions of Gaussian Type Basis Sets for Use in Molecular Orbital Studies of Organic Molecules," *J. Chem. Phys.*, vol. 56, no. 05, pp. 2257–2261, 1972.

[118] M. M. Francl, B. M. College, W. J. Pietro, W. J. Hehre, and M. S. Gordon, "Self-consistent molecular orbital methods . XXIII . A polarization-type basis set for second-row elements," *The Journal of Chemical Physics*, vol. 77, no. 3654, pp. 3654–3665, 1982.

[119] L. R. Melby, N. J. Rose, E. Abramson, and J. C. Caris, "Synthesis and Fluorescence of Some Trivalent Lanthanide Complexes," *J. Am. Chem. Soc.*, vol. 86, no. 23, pp. 5117–5125, 1964.

[120] D. Purushotham, V. Ramachanda Rao, and B. Raghava Rao, "Studies on rare earth 1,3-diketonates," *Analytica Chimica Acta*, vol. 33, no. C, pp. 182–197, 1965.

[121] B. T. Thole, P. Carra, F. Sette, and G. van der Laan, "X-ray circular dichroism as a probe of orbital magnetization," vol. 68, pp. 1943–1946, March 1992.

[122] T. Komeda, H. Isshiki, J. Liu, Y.-F. Zhang, N. Lorente, K. Katoh, B. K. Breedlove, and M. Yamashita *Nature Communications*, p. 217, mar.

[123] W. Nolting and A. Ramakanth, *Quantum theory of magnetism*. Springer-Verlag Berlin Heidelberg, 2009.

[124] E. Stavitski de Groot, F, "The CTM4XAS program for EELS and XES spectral shape analysis of transition metal L-edges," *Micron*, vol. 41, no. 7, pp. 687–694, 2010.

[125] A. J. Heinrich, J. A. Gupta, C. P. Lutz, and D. M. Eigler, "Single-atom spin-flip spectroscopy," *Science*, vol. 306, no. 5695, pp. 466–469, 2004.

[126] C. F. Hirjibehedin, C.-Y. Lin, A. F. Otte, M. Ternes, C. P. Lutz, B. a. Jones, and A. J. Heinrich, "Large Magnetic Anisotropy of a Single Atomic Spin Embedded in a Surface Molecular Network," *Science*, vol. 317, no. 5842, pp. 1199–1203, 2007.

[127] J.-p. P. Gauyacq, N. N. Lorente, and F. D. Novaes, "Excitation of local magnetic moments by tunneling electrons," *Progress in Surface Science*, vol. 87, no. 5-8, pp. 63–107, 2012.

[128] B. Bryant, R. Toskovic, A. Ferran, J. L. Lado, A. Spinelli, J. Fernandez-Rossier, and A. F. Otte, "Controlled complete suppression of single-atom inelastic spin and orbital cotunneling," *Nano Letters*, vol. 15, no. 10, pp. 6542–6546, 2015. PMID: 26366713.

[129] M. Steinbrecher, A. Sonntag, M. dos Santos Dias, M. Bouhassoune, S. Lounis, J. Wiebe, R. Wiesendanger, and A. A. Khajetoorians, "Absence of a spin-signature from a single ho adatom as probed by spin-sensitive tunneling," *Nature Communications*, vol. 7, Feb. 2016.

[130] D. E. Smiles, E. R. Batista, C. H. Booth, D. L. Clark, J. M. Keith, S. A. Kozimor, R. L. Martin, S. G. Minasian, D. K. Shuh, S. C. E. Stieber, and T. Tyliszczak, "The duality of electron localization and covalency in lanthanide and actinide metallocenes," *Chem. Sci.*, vol. 11, pp. 2796–2809, 2020.

[131] C. A. P. Goodwin, F. Ortu, D. Reta, N. F. Chilton, and D. P. Mills, "Molecular

magnetic hysteresis at 60 kelvin in dysprosocenium," *Nature*, vol. 548, pp. 439–442, Aug. 2017.

[132] M. Piantek, G. Schulze, M. Koch, K. J. Franke, F. Leyssner, A. Krüger, C. Navío, J. Miguel, M. Bernien, M. Wolf, W. Kuch, P. Tegeder, and J. I. Pascual, "Reversing the thermal stability of a molecular switch on a gold surface: ring-opening reaction of nitrospiropyran.," *Journal of the American Chemical Society*, vol. 131, pp. 12729–35, September 2009.

[133] D. Klar, A. Candini, L. Joly, S. Klyatskaya, B. Krumme, P. Ohresser, J.-P. Kappler, M. Ruben, and H. Wende, "Hysteretic behaviour in a vacuum deposited submonolayer of single ion magnets," *Dalton Trans.*, vol. 43, no. 28, pp. 10686–10689, 2014.

Der Lebenslauf ist in der Online-Version aus Gründen des Datenschutzes nicht enthalten.

Publikationsliste

Publikationen im Zusammenhang mit der Doktorarbeit

Paul Stoll, Matthias Bernien, Daniela Rolf, Fabian Nickel, Qingyu Xu, Claudia Hartmann, Tobias R. Umbach, Jens Kopprasch, Janina N. Ladenthin, Enrico Schierle, Eugen Weschke, Constantin Czekelius, Wolfgang Kuch, and Katharina J. Franke. Magnetic anisotropy in surface-supported single-ion lanthanide complexes. *Phys. Rev. B*, 94:224426, 2016.

Paul Stoll, Christian Lotze, Janina N Ladenthin, Tobias R Umbach, Isabel Fernández-Torrente, and Katharina J Franke. Correlation of Kondo effect and molecular conformation of the acceptor molecule in the TTF-TCNE charge transfer complex. *Journal of Physics: Condensed Matter*, 30(45):454002, 2018.

Sonstige Publikationen

T. R. Umbach, M. Bernien, C. F. Hermanns, A. Krüger, V. Sessi, I. Fernandez- Torrente, P. Stoll, J. I. Pascual, K. J. Franke, and W. Kuch. Ferromagnetic coupling of mononuclear Fe centers in a self-assembled metal-organic network on Au(111). *Physical Review Letters*, 109(26), 2012.

M. Stampe, P. Stoll, T. Homberg, K. Lenz, and W. Kuch. Influence of ferromagnetic- antiferromagnetic coupling on the antiferromagnetic ordering temperature in Ni/Fe_xbilayers. *Phys. Rev. B*, 81:104420, 2010.

Danksagung

Als allererstes möchte ich natürlich Katharina danken für die Möglichkeit in ihrer Gruppe zu arbeiten. Durch die spannende Forschungsrichtung, die Freiheit zu messen, was auch immer ich wollte, war das Sammeln von Daten wirklich ein riesiger Spaß. Es gab immer viele Gelegenheiten für Vorträge in der Gruppe oder auch auf Konferenzen, durch die sich die Ergebnisse immer interessant und relevant angefühlt haben. Sie war immer für mich da, wenn es Schwierigkeiten gab z.B. mit der Elternzeit, während der Drittmittelstellen überraschenderweise auslaufen und hat letztendlich immer alle Probleme gelöst.

Wolfgang möchte ich dafür danken, dass er sich bereit erklärt hat mein Zweitgutachter zu sein obwohl er Zweitgutachter von gefühlt hundert anderen Doktoranden war. Auch für die gemeinsame Zeit als Tutor in seinen Vorlesungen, mit den sehr netten Besprechungen und interessanten Diskussionen möchte ich mich bedanken.

Als nächstes möchte ich den Postdocs, die mich betreut haben danken. Matthias dafür, dass er das Dysprosium-Projekt organisiert hat und für die vielen Diskussionen, die mir in vieler Hinsicht sehr geholfen haben. Chris möchte ich auch für sehr viele Gespräche danken, aber natürlich auch dafür dass ich sein AFM benutzen durfte und die SSDs, die irgendwann in jedem Rechner der Umgebung steckten. Tobi möchte ich an dieser Stelle danken, obwohl er genau genommen nicht mein Postdoc war, weil er de facto doch eine ähnliche Rolle gespielt hat. Sein Vorbild erfolgreich wissenschaftliche Projekte durchzuführen hat etwas auf mich abgefärbt und das hat viel zu dem Erfolg meiner Projekte beigetragen.

Den vielen Leuten in der Gruppe möchte ich für die Gesellschaft bei den Mittagessen und den Kaffeerunden danken. Die gegenseitige Hilfe im Labor, für die wirklich jeder wirklich immer gern zur Verfügnung gestanden, macht mich dankbar aber vor allem stolz in dieser Gruppe gewesen zu sein. Ganz besonderer Dank gilt Janina, die immer die hübschesten Bilder und Spektren aufgenommen hat und Daniela, die keine Angst vor dem Dysprosiummonster hatte. Finn möchte ich danken dafür, dass er mich am Anfang in die Maschine eingearbeitet und Nils für seinen Igor Code zum Laden von

Createc Dateien. Wibke danke ich für die Kaffeepausen, die wir auch noch hatten als sie nicht mehr meine Bürokollegin war und Rory für seine Gesellschaft im Büro als Wibke weg war. Natürlich kann ich Gelavizh nicht unerwähnt lassen, auch wenn wir gar keine gemeinsamen Forschungsprojekte hatten (zumindest keine erfolgreichen), allein schon weil sie immer die Molekülverdampfer repariert hat, die uns anderen kaputt gegangen sind. Ich kann natürlich nicht alle Leute aufzählen, es waren zu viele und ich würde garantiert jemanden vergessen.

Zuallerletzt danke ich meiner Familie, die mich immer untertützt hat. Ohne die Hilfe und die Liebe meiner Eltern hätte ich vieles und auch diese Arbeit nicht beenden können. Julia, auch du warst immer für mich da mit Rat und Tat und vielem mehr. Unserem Sohn Bero möchte ich natürlich danken, weil er unser Leben und uns so verändert hat.

Selbstständigkeitserklärung

Name: Stoll
Vorname: Paul

Ich erkläre gegenüber der Freien Universität Berlin, dass ich die vorliegende Dissertation selbstständig und ohne Benutzung anderer als der angegebenen Quellen und Hilfsmittel angefertigt habe. Die vorliegende Arbeit ist frei von Plagiaten. Alle Ausführungen, die wörtlich oder inhaltlich aus anderen Schriften entnommen sind, habe ich als solche kenntlich gemacht. Diese Dissertation wurde in gleicher oder ähnlicher Form noch in keinem früheren Promotionsverfahren eingereicht. Mit einer Prüfung meiner Arbeit durch ein Plagiatsprüfungsprogramm erkläre ich mich einverstanden.

Datum:_____Unterschrift:_____